Effect of Polymeric Interlayers in Sulfide-Based Solid-State Batteries

Jelle Hoite Prins

Delft University of Technology

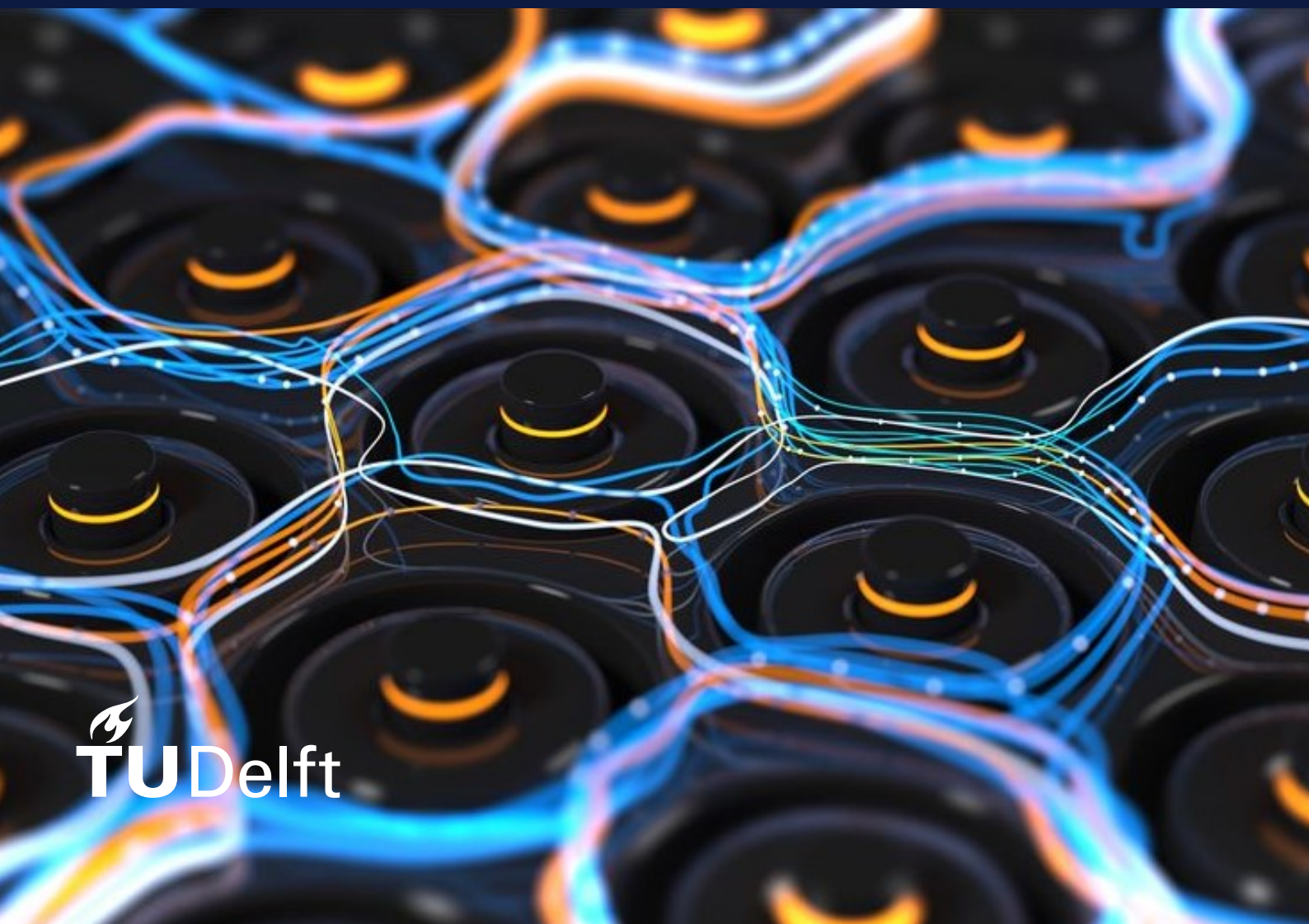

Effect of Polymeric Interlayers in Sulfide-Based Solid-State Batteries

by

Jelle Hoite Prins

to obtain the degree of Master of Science
in Sustainable Energy Technology
at Delft University of Technology,
to be defended publicly on the 22^{nd} of April at 15:00.

Student number:	4677811	
Project duration:	September 2023 - April 2024	
Thesis Committee:	Prof. dr. F.M. Mulder,	TU Delft, supervisor
	Prof. dr. ir. M. Wagemaker,	TU Delft
	Dr. Swapna Ganapathy	TU Delft
	Ir. P. Karanth,	TU Delft, daily supervisor

An electronic version of this thesis is available at the TU Delft Repository.

Acknowledgements

I am proud to present this MSc thesis, which marks the end of my journey at TU Delft. As I reflect on the past eight months as a research student at TU Delft, I am grateful for everything I have experienced and for everyone I have met along the way. I consider myself lucky to be surrounded by an incredible group of people who provided opportunities for learning, room for failure, and ample room for personal growth.

I am thankful to Pranav, my daily supervisor. You've guided me from the start of this master's end project and encouraged and supported me through the challenging stages of this study. It felt like we worked as a team, and I will miss that. I would also like to thank Fokko for supervising my thesis, providing me with the knowledge I needed, and making sure the project was moving in the right direction. Your lectures on the Necessity of Storage Technology have opened my eyes to a real challenge in the energy transition.

I am thankful to my defense committee members, Marnix and Swapna, who have generously provided expertise during the HSE meetings. Thanks should also go to Mark, Jeff, Zhu, Ajay, and all other MECS and SEE group members for their feedback and words of encouragement. I will miss the numerous times we celebrated your accomplishments, with home-made pies, cakes, and other sweets. A special thanks to my fellow master students for their moral support, and all the enjoyable coffee breaks. Additionally, I want to express my gratitude to my colleagues back in Amsterdam for their support and interest in this study.

On a more personal note, I owe my gratitude to my friends and my family. My friends from Westland and my friends from the Paardenmarkt 1B, for all the laughs we had and the holidays and weekends we spent together; you all made this journey ever so much more enjoyable! My girlfriend, Taryn, my parents, my brothers, my sister-in-law, and the little one for their unconditional love and support; without you, this would not have been possible.

Jelle Prins
Delft, April 2024

Abstract

Sulfide-based solid-state batteries (SSBs) are emerging as a top contender for next-generation rechargeable batteries with improved safety and outstanding energy densities. SSBs incorporate non-flammable solid-electrolytes (SEs), eliminating safety hazards for batteries in electric vehicles and electronic devices. In addition, the development of SSBs with SEs allows the conventional graphite anode to be replaced by a lithium metal anode, theoretically surpassing the energy densities of lithium-ion batteries (LIBs). However, SSBs with high nickel cathode materials such as $LiNi_{0.8}Mn_{0.1}Co_{0.1}O_2$ (NMC), exhibit several cathode interface-related issues preventing the large-scale adoption of this technology. Specifically, the problems include challenges such as mechanical and chemical instability, which results in particle cracking, contact loss, and decomposition of the solid-electrolyte.

To overcome these challenges, this study used polymeric interlayers at the surface of the NMC to buffer volume changes and passivate chemical side reactions. Herein, the Ni-rich layered oxides polycrystalline NMC811 (PC-NMC) and single-crystal NMC Ni82 (SC-NMC) were coated with PDDA-TFSI, poly(diallyldimethy-lammonium) bis(trifluoro-methanesulfonyl)imide, using a microencapsulation method. Additionally, this study aimed to maximize the utilization of cathode active material with the use of the conductive additive carbon nanofibers (CNFs) and the addition of lithium salt (LiTFSI) in the polymeric coating. Full lab-scale SSBs consisted of a coated NMC-based cathode, a Li-In alloy anode, and Li_6PS_5Cl solid-electrolyte.

The conductive carbon additive severely increased SSB degradation, which was associated with the formation of decomposition elements sulfates/sulfites (SO_x), polysulfides (P_2S_x), phosphates (PO_x), and lithium phosphate phases (P/Li_xP). The polymeric coating on PC-NMC slightly improved cycle stability. Here, improvements were associated with the significant reduction of contact loss between NMC and Li_6PS_5Cl particles. The cathode with SC-NMC with a PDDA-(Li)TFSI polymeric coating demonstrated exceptional performance improvements in SSBs, mitigating chemical and mechanical degradation. It showcased improved cycle stability with a capacity retention of 95% observed after 100 cycles at 0.2C, compared to a capacity retention of 84% for SSBs without a cathode interface coating. Furthermore, a significantly improved initial capacity of 155 mAh g^{-1} at 0.2C was established, compared to an initial capacity of 144 mAh g^{-1} for uncoated SSBs. Overall, the results highlight the performance-enhancing effect of a polymeric coating with added lithium salts in Li_6PS_5Cl-based SSBs.

Contents

List of Figures

List of Acronyms and Abbreviations

SSB Solid-State Battery

LIB Lithium-ion Battery

SE Solid Electrolyte

LE Liquid Electrolyte

LPSC Li_6PS_5Cl, or agryrodite

CAM Cathode Active Material

CEI Cathode Electrolyte Interphase

SEI Solid Electroltye Interphase

LCO Lithium Cobalt Oxide

NMC Lithium Nickel Manganese Cobalt Oxide

NCA Lithium Nickel Cobalt Aluminium Oxide

LNMO Lithium Nickel Manganese Oxide

CBD Carbon-Binder Domain

SEM Scanning Electron Microscope

CB Carbon Black

VGCF Vapor-Grown Carbon Fiber

CNF Carbon Nanofibers

EIS Electrochemical Impedance Spectroscopy

XRD X-Ray Diffraction

XPS X-Ray Photon Spectroscopy

TEM Transmission Electron Microscopy

PC-NMC Polycrystalline Lithium Nickel Manganese Cobalt Oxide

SC-NMC Single-crystal Lithium Nickel Manganese Cobalt Oxide

PDDA-TFSI poly(diallyldimethylammonium)-bis(trifluoro- methanesulfonyl)imide

1 Introduction

The demand for efficient and sustainable energy storage systems has never been more critical than in today's rapidly evolving energy infrastructure. To transition towards a cleaner and greener future, developing advanced energy storage technologies is a crucial solution to tackle the challenges of renewable energy integration, electric vehicle propulsion, and portable electronic devices. Solid-state batteries have emerged as a promising solution, offering significant advancements in safety, energy density, and lifespan compared to lithium-ion batteries' liquid electrolyte counterparts. However, considerable challenges remain for full-scale commercialization, cell performance, and lifespan of solid-state batteries. One of the main challenges this study will cover in detail is optimizing the cathode-electrolyte interface, which remains a critical challenge in achieving optimal solid-state battery performance and lifetime.

1.1. Solid-State Batteries: Challenges and Possible Solutions

In the last decade, Solid-State Batteries (SSBs) have emerged as a potential future electrochemical energy storage technology that can surpass the performance characteristics and safety standards of state-of-the-art Lithium-ion Batteries (LIBs). Currently, LIBs hold an uncontested position as the preferred technology for electrochemical energy storage, primarily due to their notable attributes, such as volumetric and gravimetric energy densities, power densities, exceptional cyclability, and reliability. However, for more widespread adoption of LIBs, mitigation of fundamental challenges, such as safety hazards from battery ignition, and fires, is required while meeting demands for even higher energy and power densities and attaining acceptable performance in various temperature ranges. Here, SSBs come into play.

Researchers are studying SSB technology with higher energy and power densities and improved safety standards. Furthermore, the use of solid electrolyte (SE) in SSBs can avert electrode cross-talk, as well as adverting the unwanted electrochemical reactions leading to lithium dendrite formation at the electrodes, causing long-term deterioration in conventional LIBs, eliminating concerning safety hazards for electric vehicles and electronic devices. In addition, research has led to the development of SEs with higher ionic conductivity, which could lead to higher power densities. In the future, SSBs have the potential for faster charging times, higher power densities, and higher safety standards.

Despite the promising performance improvements and higher device safety, SSBs face challenges that must be overcome before they can compete with conventional LIBs. The most pressing challenges for SSBs are the following. The first challenge is developing and preparing solid-state composite cathodes that demand minimal stack pressure for long-term operational stability. The second major challenge is designing and fabricating high-capacity anodes suited for stable long-term operation. Another challenge is the development of SEs with exceptionally high ionic conductivities, which are cost-effective and offer adequate stability. Research should also focus on the challenge of long-term stability across anode-, cathode-separator, and cathode-electrolyte interfaces. Finally, a critical challenge with the increasing usage of rechargeable batteries in our everyday lives is the adoption of sustainable battery recycling, which

emerged as a crucial challenge. This study will focus on the known cathode-electrolyte interface-related issues and test the possible solution of polymeric interlayers at the cathode electrolyte interface.

1.2. Polymeric Interlayers at the Cathode-Electrolyte Inferface

Solid-state batteries work on the premise of solid electrolytes with similar or even greater ionic conductivities than their liquid electrolyte predecessor. However, not all solid electrolytes have an ionic conductivity superior to that of LE, and the implementation of SE comes with an entire set of complex macro-, micro-, and nanoscale challenges on the cathode electrode side alone. These challenges arise at the designing phase of the cathode when selecting active material particle sizes and selecting the ratio of cathode active material (CAM) to SE. Another challenge arises during the electrochemical cycling of the SSB; due to the chemo-mechanical processes, the volume and morphology of the cathode change problematically.

The volume and morphology changes of the materials inside the SSB result in many interface-related issues. This study will focus specifically on the interface-related issues at the cathode side of SSBs. The problems at the cathode-electrolyte interface are contact loss of CAM to the SE, and cathode electrolyte interphase (CEI) formation. A promising solution for these issues is the application of polymer interlayers. The polymer interlayers work as a buffer for volumetric changes, reducing contact losses between the CAM and the SE. Furthermore, the polymeric interlayers can avoid direct contact between the CAM and the electrochemically unstable SE, promising to reduce the formation of a highly resistive CEI. In addition, conductive additives must be considered an essential component in the cathode of solid-state batteries. Conductive additives, such as carbon black or carbon nanofibers, provide electronic pathways within the cathode. However, they form a point of deterioration, which also needs to be investigated for optimal cathode performance.

1.3. Techniques to Study the Cycling Performance and the Cathode Electrolyte Interfaces

As recently pointed out by Janek et al. [7], the cathode-electrolyte interface remains a significant challenge in speeding up the development of solid-state batteries. Over the past years, research has focused on tackling the stability and performance of the solid-state battery by examining the composition of anode material, cathode active material, and solid electrolyte. In comparison, limited research has been conducted to understand the effect of protective coatings in countering the volume and morphology changes of the cathode in solid-state batteries. Some research has been conducted on the effect of conductive additives on cycling performance and the long-term stability of conductive additives. Still, additional research could be done into the interface-related issues between the composite cathode material and the conductive additive.

The characterization techniques used in this study are Electrochemical Impedance Spectroscopy (EIS), X-ray Photon Spectroscopy (XPS), X-ray Diffraction (XRD), and Scanning Electron Microscopy (SEM). These techniques are excellent for analyzing electrochemical side reactions and monitoring deformations visually. This study uses EIS, XPS, XRD, and SEM data to study the cathode-electrolyte interfaces, assess the cycling performance, and investigate the chemical stability during electrochemical cycling.

1.4. Scope of Work and Research Questions

This study aims to study the cathode/solid-electrolyte interface in solid-state batteries with the introduction of polymeric interlayers. Additionally, the effect of conductive additives is studied to determine optimal cathode electrode kinetics. The main research question that is investigated in this work is:

"How do polymeric interlayers affect the cycling performance and the stability of the cathode/solid-electrolyte interface in sulfide-based solid-state batteries?"

Sub-research questions have been formulated to help answer the main research question. These research questions are subdivided into questions related to cathodes with conductive additives, and polymeric interlayers on different cathode active materials. The division is as follows:

*1. What are the effects of **carbon nanofibers** - as a conducive additive - on the cycling performance and cathode/solid-electrolyte interface stability, in sulfide-based SSBs?*

*2. How does the application of a **polymerized ionic liquid** - as a protective coating - influence the cycling performance and stability of the cathode/solid-electrolyte interface in sulfide-based solid-state batteries?*

a) on polycrystalline and single-crystal cathode active material structures,

b) with varying coating thicknesses,

c) with and without lithium salt.

After introducing the subject of this study, the problem situation, the solution proposition, and the main research questions, this work will continue with the literature review in Chapter 2. This chapter will provide the background and the working principles of solid-state batteries, elaborating on the (chemo-)mechanics and kinetics in SSBs. After this, the function of conductive additives and the concept of polymeric interlayers are discussed. The materials used in this study and the methods to prepare the SSB cells are presented in Chapter 3. Following is Chapter 4, which describes and interprets the results of the various experiments carried out on the SSBs with conductive additives and polymeric coatings on polycrystalline NMC and single-crystal NMC. Chapter 5 will briefly discuss and compare some of the outcomes with other studies; limitations of this work are included in this section. The formulated research questions will be answered in the concluding chapter in Chapter 6. This chapter will also provide recommendations for future research.

2

Literature Review

This chapter aims to provide a comprehensive overview of solid-state batteries, the research challenges involved at the solid electrolyte and cathode interface, the function of conductive carbon additives, and the role of polymer interlayers in the development of solid-state batteries. The working mechanism and the various components of solid-state batteries are discussed. In addition, the fundamentals of solid electrolytes are discussed in further detail. The general theories of (chemo-)mechanics and kinetics at the solid electrolyte cathode interface are examined and further discussed. Particular attention is devoted to the optimization of the ratio of cathode active material to solid electrolyte and the optimization of the particle sizes. Furthermore, the function of conductive additives and the different types of conductive additives are considered. Finally, the concept of polymeric interlayers is introduced, expanding on the working mechanism of polymeric binder and protective coatings, while a variety of suitable polymers and their characteristics are explored.

2.1. Solid-State Batteries: Working Mechanisms and Components

This section will briefly introduce the case for solid-state batteries (SSBs) and their basic working mechanism. The components comprising a solid-state battery and the challenges and suitable characteristics of a variety of materials are discussed. All materials used in SSBs have their own set of advantages and disadvantages; a strategic selection of the solid electrolyte, cathode active materials, and anode material is made. Lastly, the half-reactions of a solid-state battery with the selected materials are displayed and discussed in further detail.

2.1.1. Basic Working Mechanism

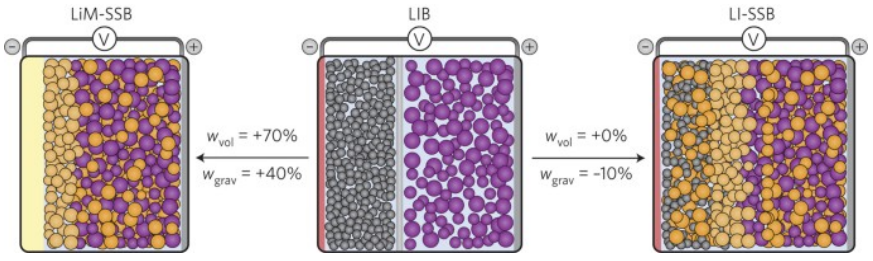

Figure 2.1: Schematic overview of the key differences between liquid and solid electrolyte batteries [1].

A Lithium-ion Battery (LIB) consists of an anode, usually made from a type of graphite, a thin separator, a cathode, and a liquid electrolyte contained in the pores of the cathode. If the liquid electrolyte (LE) were

replaced by a solid electrolyte (SE), no significant gains in terms of volumetric- and gravimetric density would be made, as a solid electrolyte will always have a higher density than a liquid electrolyte. However, by replacing the conventional graphite electrode with a reversible lithium metal anode, a significant jump in volumetric and gravimetric energy density could be made of up to 70% and 40%, respectively, as displayed in figure 2.1 [1].

During discharge, lithium metal is stripped from the anode to become a lithium-ion and an electron. This lithium-ion then moves to the cathode, and the electron goes around the external circuit to extract useful electrical work, for example, for our portable devices. When the battery is discharged the volume of the battery is smaller, during charging lithium-ions are plated back onto the lithium metal, and the battery expands again. This process is further described in subsection 2.1.7, Half Reactions, and Overall Cell Reaction. Repeating this cycle of charging and discharging can lead to degradation of the battery performance caused by chemo-mechanics and kinetics [26], which is further discussed in section 2.2.

2.1.2. Solid Electrolytes

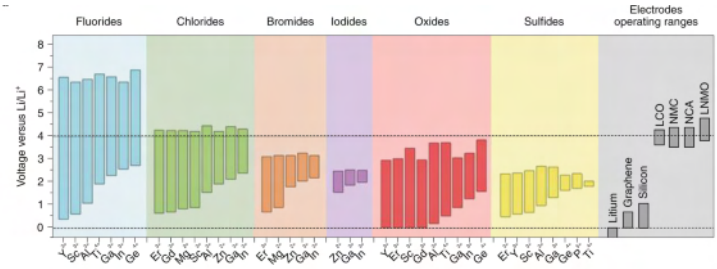

Figure 2.2: Electrochemical stability of various inorganic solid electrolytes. Illustration of solid electrolytes versus common electrodes' typical operating potential. Lithium Cobalt Oxide (LCO), Nickel Manganese Cobalt (NMC), Nickel Cobalt Aluminium (NCA), and Lithium Nickel Manganese Oxide (LNMO) [2].

Research has been conducted on several types of solid electrolytes. This group of materials can be divided into the inorganic halide-, oxide-, and sulfide-based SEs and the organic group of polymer electrolytes. Recent discoveries show SE materials with ionic conductivities comparable to or even greater than their LE counterparts. The most important characteristics of SEs are (oxidative) electrochemical stability, mechanical stability, and high ionic conductivity [6] [7].

The inorganic group of SEs, halides, oxides, and sulfides, has its own set of advantages and disadvantages. Figure 2.2 illustrates the oxidative electrochemical stability window of these material classes versus the typical operating potential of common electrodes [2]. From left to right, this figure displays the halides (fluorides, chlorides, and bromides), oxides, and sulfides set off against the operating potentials of common electrodes: Lithium Cobalt Oxide (LCO), Nickel Manganese Cobalt (NMC), Nickel Cobalt Aluminium (NCA), and Lithium Nickel Manganese Oxide (LNMO).

From this figure, it is evident that halide-based SEs have high oxidative electrochemical stability, which allows for stable operation together with the Cathode Active Material (CAM) without the risk of chemical decomposition. Halide-based SEs have moderate ionic conductivity of 1 (mS cm^{-1}) at low operating temperatures, which gives it a poor performance for fast charging and discharging capabilities. Oxide-based SE is the second class of materials that offer high oxidative electrochemical stability. However, their maximum ionic conductivity is around 1 mS cm^{-1} as well. Apart from that, the brittle nature and lack of mechanical rigidity make this material challenging to work with when required to maintain contact with the CAM after multiple charging and discharging cycles [27].

The group of materials with exceptionally high ionic conductivities are the sulfides (e.g., argyrodite), with an ionic conductivity of up to 25 mS cm^{-1} at room temperature. Mechanical properties of this substance, such as great malleability and a low Young's modules, make this one the most researched SE of present-day [27]. However, the relatively short window for oxidative electrochemical stability (figure 2.2) forms its most prominent challenge and gives rise to the need for coatings or protective layers to prevent direct contact with the CAM and chemical decomposition.

Polymer-based SEs are very versatile materials, showing advantageous mechanical characteristics, and can be fabricated from solutions or in molten states [6]. A systematic overview, as given for the inorganic SEs, is challenging to produce due to the multidisciplinary research fields interested in polymeric-based SEs [3]. However, their oxidative electrochemical stability is yet too low for stable operation, and limited ionic conductivity at room temperature presents significant challenges for this group of materials.

2.1.3. Working Mechanism of Solid Electrolytes

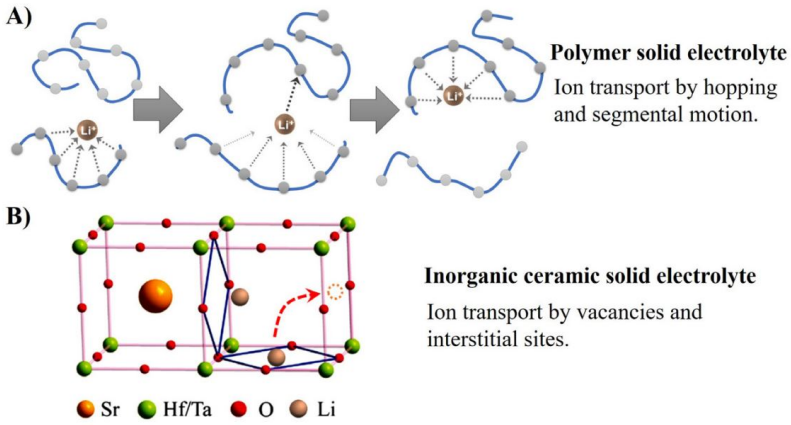

Figure 2.3: Schematic presentation of predominant Li^+ ion transport in A) Polymer-based solid electrolyte, and B) Inorganic ceramic solid electrolyte [3].

The specific mechanisms governing ion conduction vary across different solid electrolytes and are not universally comprehended. However, commonly reported mechanisms for polymer-based solid electrolytes and inorganic halide-, oxide-, and sulfide-based SEs are depicted in Figure 2.3. In polymer-based solid electrolytes, the conduction of ions is closely linked to the motion of main chain segments above and the hopping of Li^+ ions between inter- and intra-chain positions (Figure 2.3A). In contrast, for inorganic ceramic electrolytes, Li^+ ions migrate or hop among vacancies and interstitial sites (Figure 2.3B). These vacancies and interstitial sites are purposefully created in the material to enhance ionic conductivity; these sites are fixed in place. The advantages of polymer solid electrolytes are the suitable mechanical characteristics, such as flexibility, and the favorable characteristics for fabrication processes [3]. However, its ionic conductivity is relatively low at room temperature (~1 mS cm^{-1}) compared to its inorganic ceramic solid electrolyte counterparts. This needs to be taken into consideration when selecting a suitable solid electrolyte.

2.1.4. Choice of Electrolyte

The application of sulfide electrolytes has gained popularity among researchers for their high ionic conductivity and good machinability. However, their application is still limited due to the small electrochemical stability window [2]. Lithium argyrodite Li_6PS_5X (X = halogen) is seen as a key member in the sulfide SEs group, as it shows fast ionic conductivity, moderate mechanical properties, and a slightly broader electrochemical stability window compared to other sulfides [28].

Nevertheless, the interface between the electrodes and the argyrodite is problematic as a result of the electrochemical instability. The reaction at the interface of Li_6PS_5Cl, and cathode active material with oxides, such as Lithium Cobalt Oxide (LCO), Nickel Manganese Cobalt (NMC), and Lithium Nickel Manganese Oxide (LNMO), has been reported in Auvergniott et al. [29]. Upon cycling, the argyrodite (Li_6PS_5Cl) is oxidized into elemental sulfur (S) and polysulfides, P_2S_X ($X \geq 5$), while discharging these

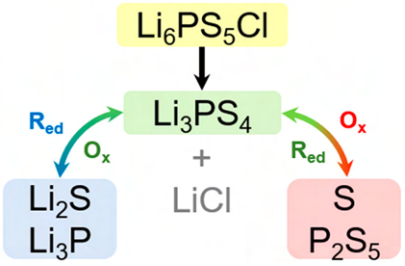

Figure 2.4: Representation of the redox reaction pathways of argyrodite (Li_6PS_5Cl) for the first charge and subsequent charge and discharge cycles [4].

products lead to reduced Li_3PS_4 and LiCl, thereafter forming lithium phosphide (Li_3P), and lithium sulfide (Li_2S) [4]. This process is described in figure 2.4. Due to the oxygen-rich nature of the active material of the cathode, the formation of sulfate/sulfide fragments (SO_x) is also possible [12]. The unstable interphase created between the argyrodite and the cathode active material will lead to an increased interface resistance, capacity deterioration, and potentially total failure of the corresponding SSB.

Despite the electrochemical instability leading to unstable cathode-electrolyte interface, lithium argyrodite with a chloride halogen group (Li_6PS_5Cl) is selected as the solid-electrolyte of choice for this study due to its high ionic conductivity, good processability, and its commercial availability. The argyrodite, Li_6PS_5Cl, selected is produced by the NEI Corporation; the specifications are listed in Appendix A. It is essential to improve the interaction between the SE and CAM; one possible solution is the use of polymeric interlayers with high ionic conductivity. The CAM can be coated with an organic polymeric protective coating to avoid direct contact with the argyrodite sulfide SE. Protection strategies of the cathode-electrolyte interface and the selection of suitable polymeric materials are discussed in further detail in sections 2.2 and 2.4, respectively.

2.1.5. Choice of Cathode Active Material

Within LIB and SSB research, a lot of time is devoted to cathode materials, as several challenges still exist regarding material costs, improving battery capacity, and interactions between the CAM and the SE of choice [6]. One of the first CAMs that were present in commercially viable LIBs was the layered oxide material $LiCoO_2$. The working principle behind layered oxides is the lithium intercalation between the layers of an oxide in a crystalline structure that enhances ionic conductivity for lithium ions during electrochemical cycling [30].

The problem with $LiCoO_2$ is the scarcity, geographical concentration, and accompanying costs of Cobalt. One approach to make the cathode material in batteries cheaper is to replace the relatively expensive Cobalt with other transition metals (TMs), such as nickel and manganese [31]. Using the materials nickel and manganese in cathode material gave rise to the isostructural materials, such as $LiNi_xMn_yCo_zO_2$. In scientific literature, this isostructural material is referred to as NMCXYZ, with X, Y, and Z indicating the molar ratios of Ni, Mn, and Co, respectively [32]. A large variety of Ni, Mn, and Co contents have been used in commercially available batteries; some examples are NMC532, NMC622, and NMC811. Despite these advancements, cathode materials with even higher Ni contents are wanted as they can provide higher volumetric and gravimetric energy densities. However, Ni-based cathodes tend to be chemically unstable; adding Mn mitigates this instability and is, therefore, part of the highly successful NMC cathode material group [30]. For those reasons, the material NMC811, $LiNi_{0.8}Mn_{0.1}Co_{0.1}O_2$, is gaining tremendous popularity in present-day cathode design research.

Two types of crystalline structures for NMC particles are commercially available: polycrystalline NMC and single-crystal NMC. Polycrystalline NMC is a more commonly used and cost-effective material. However, increased states of charge cause the polycrystalline cathode particles to crack, exposing fresh surfaces and increasing capacity degradation [33]. Single-crystal NMC batteries provide higher energy and power density with faster lithium-ion diffusion, and single-crystal layered-oxide cathodes have superior

cycle life due to reduced particle cracking [33]. Therefore, single crystal NMC can offer slightly better performance output but is limited available due to the more expensive synthesis of the crystals.

In this study, polycrystalline NMC811, NANOMYTE®BE-56E, produced by NEI Corporation, as well as single-crystal NMC, PRO Single Crystal High Nickel NMC Ni82, produced by MSE Supplies LLC, is used as cathode active materials; the specifications are listed in appendix A.

2.1.6. Choice of Anode Material

The small electrochemical stability window of the selected argyrodite SE leads to limited options for electrode selection. Several studies show that the interaction between thiophosphate or argyrodite as SE and lithium metal can lead to the formation of oxidized elements [34]. This is the reason many researchers frequently favor a lithium alloy instead of lithium metal as a choice for the anode material. Lithium inserted into metals (i.e., alloy formation) typically occurs at potentials below approximately 1V vs. Li^+/Li, which is still outside the stability window of argyrodite electrolyte. However, the electrochemical oxidation process is significantly lowered compared to that of lithium metal [5]. Metals that are considered for these alloys are Aluminum (Al), Gallium (Ga), Indium (In), Tin (Sn), and Antimony (Sb).

Among these varieties, the indium-lithium alloy is preferred due to its favorable capacity to accommodate local stress concentrations, also known as ductility. The relatively high costs of indium prevent it from any large-scale applications, yet due to its high ductility, it is the preferred material for assembling SSBs for research purposes. The indium-lithium alloy can produce a constant redox potential of approximately 0.6 V vs. Li^+/Li. Besides, inserting a reference electrode into SSBs is difficult, which underlines the need for a counter electrode with a stable potential. Hence the Indium-Lithium [5].

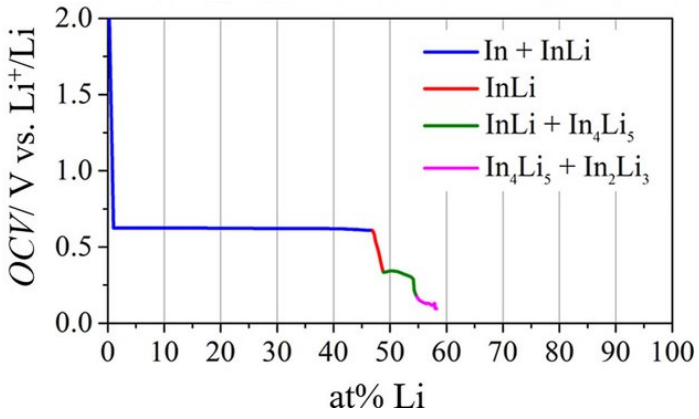

Figure 2.5: Results from a coulometric titration experiment at room temperature. The graph shows the electrochemically determined open circuit voltage (OCV) over the lithiation of In until the phase Ln_2Li_3 [5].

However, the redox potential of the In-Li is dependent on the lithium insertion percentage as shown by Santhosha et al. [5] by coulometric titration at room temperature (Figure 2.5). Research showed the importance of the right In/Li ratio of the electrode; the right ratio will enable stable lithiation and delithiation. In addition, too much lithiation leads to a build-up of interface resistance and a drop in redox potential. Therefore, in this study, an Li/In atom ratio of 1/2 will be applied to create a Lithium Indium alloy of $Li_{0.5}In$, which ensures stable operation during electrochemical cycling.

2.1.7. Half Reactions

SSBs produce electrical energy through the conversion of chemical energy stored in the electrodes through redox reactions. The following half-reactions illustrate the electrochemical reactions occurring within a complete SSB cell. In these redox reactions, $Li_{0.5}In$ is considered as the anode, and $LiNi_{0.8}Mn_{0.1}Co_{0.1}O_2$ as the cathode. During discharge, the cathode undergoes a reduction process in which NMC811 combines

with lithium ions and an electron to form lithium nickel manganese cobalt oxide. Note that NMC811 is never fully delithiated during charging, as this is kinetically challenging and can harm the structural integrity of the CAM [35]. The corresponding half-reaction is as follows:

$$Li_x^+ + Li_{1-x}Ni_{0.8}Mn_{0.1}Co_{0.1}O_2 + e_x^- \underset{\text{charge}}{\overset{\text{discharge}}{\rightleftharpoons}} LiNi_{0.8}Mn_{0.1}Co_{0.1}O_2$$

At the lithium indium anode, lithium is oxidized to Li^+ ions during discharge. In theory, the electrode under full utilization will be lithiated to $Li_{0.5}In$. However, it should be pointed out that, in practice, the alloy might never reach its full utilization capacity. The corresponding half-reaction is the following:

$$2\,Li_{0.5}In \underset{\text{charge}}{\overset{\text{discharge}}{\rightleftharpoons}} 2\,In + Li^+ + e^-$$

The fundamental process of a SSB predominantly revolves around the processes of intercalation and deintercalation of lithium ions. These processes take place between the cathode and anode, with a solid electrolyte acting as a separator. Intercalation specifically involves the introduction of lithium ions into the host matrix, all while leaving the crystal structure of the matrix intact [36].

During discharging, oxidation occurs at the anode, the lithium ions deintercalate from the anode and naturally move to the cathode, and electrons flow through the external circuit of the cell [37]. Oxidation occurs at the cathode during charging, lithium ions deintercalate from the cathode and intercalate at the lithium indium anode to store electrochemical energy.

Major performance issues with SSBs are related to the cycling of the cell and can cause capacity deterioration, as well as a decrease in its fast charging capacities. The complicated electrochemical processes lead during battery cycling as lithium extraction and incorporation lead to volume changes, and thus local stresses [38]. The effects of electrochemical cycling of SSBs and the kinetics of ionic en electronic percolation are discussed in section 2.2, General Theory of (Chemo-)Mechanics and Kinetics in Batteries.

* * *

2.2. General Theory of (Chemo-)Mechanics and Kinetics in Batteries

This section will introduce the principles of chemo-mechanics and kinetics within the field of SSB research. The main challenges correlated with the chemo-mechanics and kinetics within SSBs are discussed, and possible solutions in the form of protective strategies to these challenges are explained in further detail. Furthermore, a literature review on the optimization of the particle size of the CAM and the SE is conducted, and a suitable particle size for both the CAM and the SE is decided upon. In addition, the gravimetric ratio between the CAM and the SE is determined. Finally, the challenges and possibilities of conductive additives are discussed.

2.2.1. Chemo-Mechanics and Kinetics during Electrochemical Cycling

To understand the significance of chemo-mechanics and kinetics in the CAM during electrochemical cycling, it is important to grasp the processes occurring inside SSB cathodes. These processes are categorized in macro-, micro-, and nanostructure scales, reported by Minnmann et al. [6], displayed in figure 2.6. The cathodes in SSBs consist of CAM and SE. In addition, polymeric interlayers and conductive additives can be added to enhance mechanical and electrical properties, this is further discussed in section 2.2.2, protective strategies. Replacing the conventional LE with SE results in processes on the cathode level, particle level, and interface level.

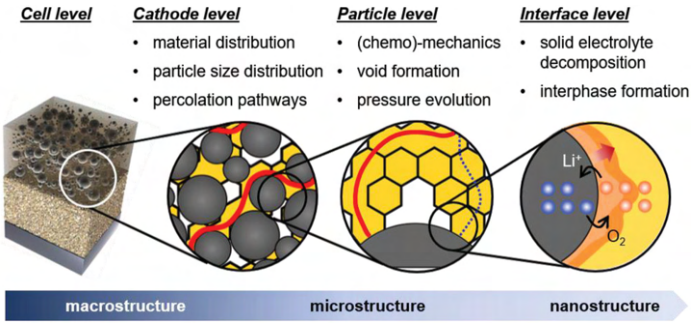

Figure 2.6: Schematic overview of the important processes occurring on different scales in SSB cathodes, caused by various challenges to the development of scalable fabrication processes and tailored material properties [6].

Firstly, at the cathode level, some important characteristics are material distribution, particle size distribution, and percolation pathways. Given that multiple solids are at play, it is during the design and fabrication phase to consider the particle distribution and particle sizes of both the CAM and the SE, as this will influence the percolation pathways of ions. Recent work has shown that the loading of active material, or the ratio between CAM and SE, significantly influences the tortuosity of the cathode, which in turn alters the ionic conductivity of the cathode [9]. The theory and effects of tortuosity and the optimization of the ratio and the particle sizes of the CAM and the SE are further explained in the section 2.2.3 and 2.2.4, respectively.

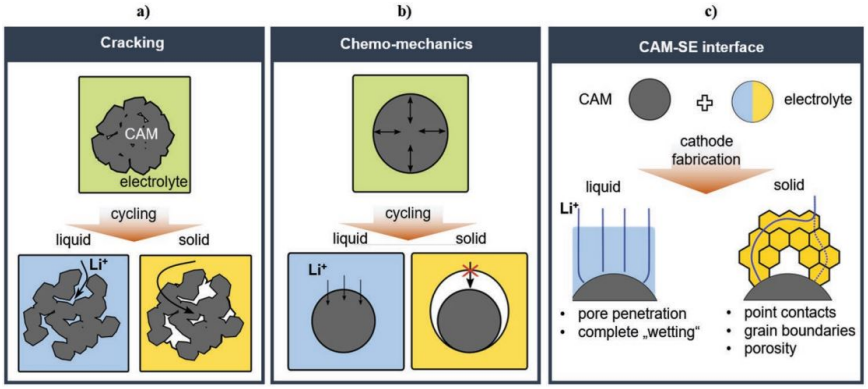

Figure 2.7: Schematic illustration of effects that come into play if changing the liquid electrolyte to solid electrolyte. a) Cracking of CAMs induced by (chemo-)mechanical stress. b) Large volume changes resulting in contact loss between CAM and SE. c) CAM-SE interface difference for liquid- and solid electrolytes [6].

Secondly, at the particle level, chemo-mechanics, void formation, and pressure evolution are characteristics that need to be taken into consideration for the design of the cathode. Chemo-mechanics is a term describing the effect of electrochemically induced volume or morphology changes in materials. During lithiation and delithiation of CAM in SSBs, the chemo-mechanical processes can lead to several forms of capacity deterioration as shown in the study by Minnmann et al.[6]. Figure 2.7 illustrates the most common chemo-mechanical effects related to the volume and morphology changes of the CAM. As reported by Koerver et al.[38], the replacement of LE with SE leads to the detrimental effects of these volumetric and morphology changes that negatively affect the capacity of the battery.

Interparticle cracking, in combination with the use of SE, as shown in Figure 2.7a, creates voids at the interface of the CAM and the SE, increasing ionic resistance across the interface. The issue of pore formation is non-existent in conventional LIB, as the LE will wet the free surface after cracking of CAM particles. A second issue is void formation due to volumetric changes of the CAM, as shown in figure 2.7b. This is another form of the occurring chemo-mechanics, resulting in a loss of surface contact between the SE and the CAM [38]. Figure 2.7c summarizes the differences for cathode fabrication with both LE and SE. In the case of cathode fabrication for LIB, the LE will penetrate all voids completely wetting the surface of the CAM particles. In the case of SSBs, direct issues arise at the cathode electrolyte interface, where the SE creates point contacts with the CAM instead of complete surface wetting, poor ionic conducting grain boundaries exist within the SE and voids are present in a porous material like SEs.

Finally, at the interface level, oxidative SE decomposition and the formation of a Cathode Electrolyte Interphase (CEI) need to be avoided. One solution is to select an electrochemically stable SE, such as the halide- or oxide-based SE [26]. However, since the SE of choice for this study is a lithium argyrodite, with a relatively small electrochemical stability window, protective measures have to be considered. The formation of CEI upon charging leads to irreversible capacity loss [39]. Protective strategies for all mentioned CAM and SE interface-related issues are elaborated on in section 2.2.2, protective strategies.

2.2.2. Protective Strategies

The electrochemical instability at the interfaces of the lithium argyrodite, the cathode active material, and the anode, remains one of the major issues in SSB development [7]. The main focus of this section is on the cathode-solid electrolyte interface, and the issues arising from unstable mechanical and electrochemical properties of the selected materials as discussed. In addition, potential solutions to the interface-related issues are proposed. Interface issues related to the anode interface, as well as the separator-cathode interface are also briefly introduced.

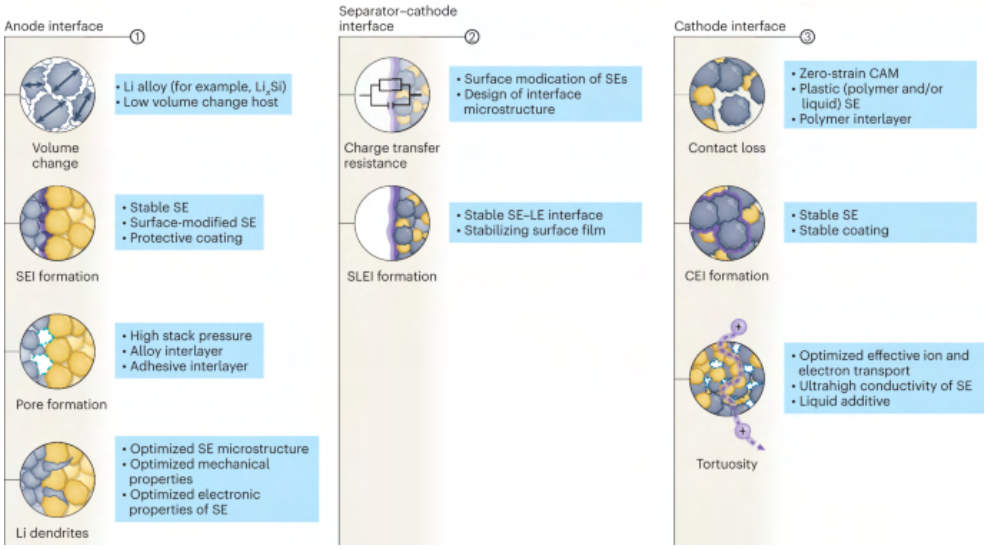

Figure 2.8: Potential solutions to interface-related issues in SSBs. From left to right: Anode interface, Separator-cathode interface, and Cathode interface-related issues and potential protective strategies [7].

Figure 2.8, from the work of Janek et al. [7], summarizes the interface-related issues and potential solutions for SSBs. At the anode interface, research is mainly focused on issues revolving around volume changes [38], formation of a solid-electrolyte interphase (SEI) [40], pore formation [41], and Li dendrite formation [42]. Possible solutions span the appropriate selection of anode and SE material, protective coatings, high stack pressure, adhesive interlayers, and optimized properties of the SE (e.g. SE particle size). At the interface of the separator and the cathode, charge transfer resistance, and SEI formation, are the governing issues. Optimized properties of the SE are among the possible solutions again. Other possible solutions are an optimized interface microstructure design and the introduction of a stabilizing surface film. This analogy emphasizes the importance of the optimization, design, and selection of the SE for stable operation at the anode, and separator-cathode interface.

The cathode is the decisive component in SSBs for battery capacity and energy density, as shown by the analysis of Kerman et al. [43] and Pasta et al. [44]. As discussed in section 2.2.1, the CAM is subject to chemo-mechanical volume changes, which leads to cracking and pore formation resulting in the first cathode interface-related issue, the contact loss between CAM and SE [38]. The second cathode interface issue is cathode electrolyte interphase (CEI) formation [26]. A final interface-related issue is tortuosity increase caused by, the porosity of the material, and grain boundaries within the SE. One solution that is already widely applied in SSB research is applying high external stack pressure, however, this is considered impractical and does not resolve the issue in its totality [16]. A suggested, and researched, solution is the use of polymer interlayers that can buffer volume changes combined with the characteristics of good ionic conductivity, electrochemical stability, and the suitable mechanical property of being elastomeric. Elastomeric refers to the ability of the polymeric binder, or interlayer, to regain its original shape after being subject to volume changes inflicted by swelling of the CAM. As suggested by Gregory et al. [16], multiple polymers should be investigated with different cell components for future SSB development. The working mechanism of polymeric interlayers, the different kinds available, and the selection of polymers for this study are further discussed in section 2.4, Polymer Interlayers as Protective Coating on Cathode Active Material.

2.2.3. Tortuosity and the Optimization of the Ratio of Cathode Active Material to Solid Electrolyte

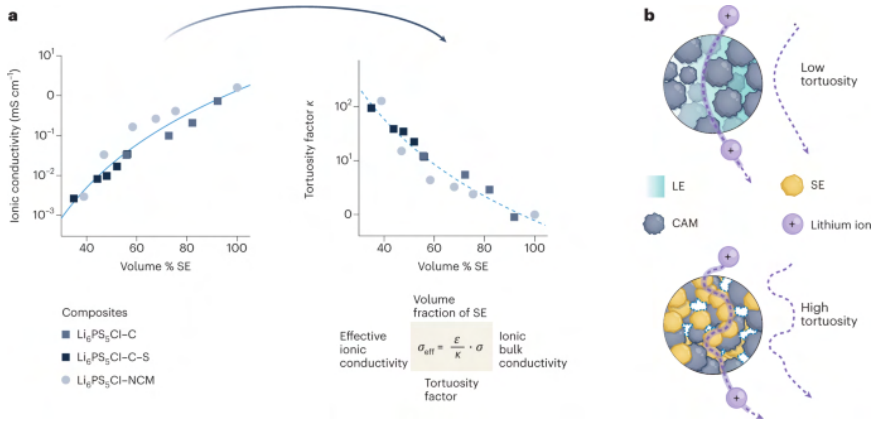

Figure 2.9: Tortuosity effects in solid-state cathode composites. a) Measured partial lithium-ion conductivity and evaluated tortuosity factor as a function of the weight percentage of SE. Values of the conductivity and tortuosity factors are taken from Ohno et al. [8] Minnmann et al. [9], respectively. b) Schematic explanation of the tortuosity in SSB cathodes, as opposed to that in LIB cathodes [7].

The selected SE, argyrodite, has a good reputation for its high ionic conductivity. However, this is necessary to compensate for the effect of tortuosity created by the use of a SE in the cathode of SSBs. Tortuosity is a critical parameter used to predict the transport properties of porous media.[45] A widely used term in earth-science-related literature is nonetheless just as relevant for the design and development of high-performance cathode electrodes. Tortuosity is a parameter related to the straightness of the path ions can travel in a composite cathode. Illustrated in figure 2.9b. low tortuosity is displayed in the cathode electrode fully immersed in LE, compared to a high tortuosity displayed in the cathode of an SSB. As a higher tortuosity relates to a longer pathway for ions, the effective ionic conductivity is reduced and needs to be compensated for to be comparable to the ionic conductivity of LIB with a LE [7].

A second parameter that needs to be considered is the ratio of SE to CAM. As shown in figure 2.9a, a higher volume percentage of SE leads to higher ionic conductivities; conversely, a lower volume percentage of SE leads to higher tortuosity and a lower ionic conductivity. Values of the conductivity and tortuosity factors are taken from Ohno et al. [8] and Minnmann et al. [9]. This is captured in the following equation:

$$\sigma_{eff} = \frac{\epsilon}{\kappa} \cdot \sigma_{bulk}$$

where σ_{eff} is the effective ionic conductivity, ϵ the volume fraction of SE, κ the tortuosity factor and σ_{bulk} the ionic bulk conductivity.[7]

A trade-off between a higher cell capacity and higher ionic conductivity has to be made, where a higher weight percentage of CAM will lead to a higher cell capacity and a higher weight percentage of SE will lead to a higher ionic conductivity. The study by Shi et al. [10] shows that the CAM is still fully utilized at a cathode loading of 70wt%. Cathode loading above 75wt% displays a drastically decreasing cathode utilization, which can be seen in figure 2.10a (note: this for a relative particle size of 1.67). In figure 2.10, θ_{CAM} is the CAM utilization, f_{CAM} is the CAM loading in weight percentage (wt%), and λ is the relative particle size $\frac{D_{CAM}}{D_{SE}}$. This is confirmed by the work of Nam et al. [46] and Zhang et al. [47], which revealed a significant decrease in cycling performance and cell capacity at a CAM loading of 80wt%. A preliminary decision of a gravimetric ratio of approximately 70wt% to 30wt% of CAM versus SE is made, this is subject to the influence of the size-, and distribution of the particles, as well as the volume percentage of conductive additives.

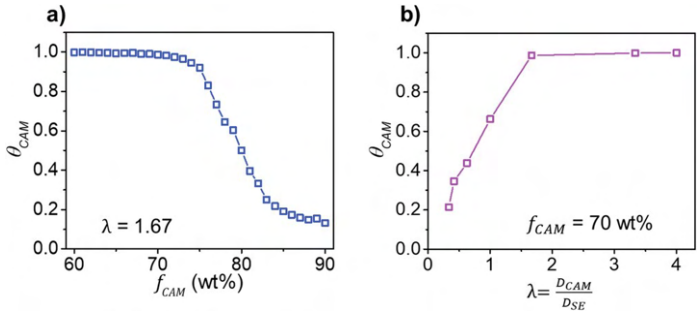

Figure 2.10: Modeling results of the study by Shi et al. [10] of the effect of a) CAM loading and b) relative particle size on CAM utilization.

2.2.4. Optimization of the Particle Sizes of Cathode Active Material to Solid Electrolyte

Despite the influence of the CAM wt% on the capacity of a battery, the work of Shi et al. [10] demonstrates that the utilization of CAM in SSBs is also highly dependent on the particle sizes of the CAM and the SE. The performance factors to be considered for the design of the particle sizes of the CAM and the SE are; interfacial degradation, electronic conductivity, ionic conductivity, diffusion pathways, and grain boundary effects [48]. Multiple options can be selected for the CAM and the SE particle sizes. In a more general sense, the CAM can either be large or small and the SE particles can either be large or small. This results in four possible sets of particle sizes, namely: large CAM and large SE, large CAM and small SE, small CAM and large SE, and small CAM and small SE, each with its own set of advantages and disadvantages. Minnmann et al. [6] concluded that a tailor-made particle size distribution needs to be considered to optimize the listed performance factors. This is summarized in figure 2.11.

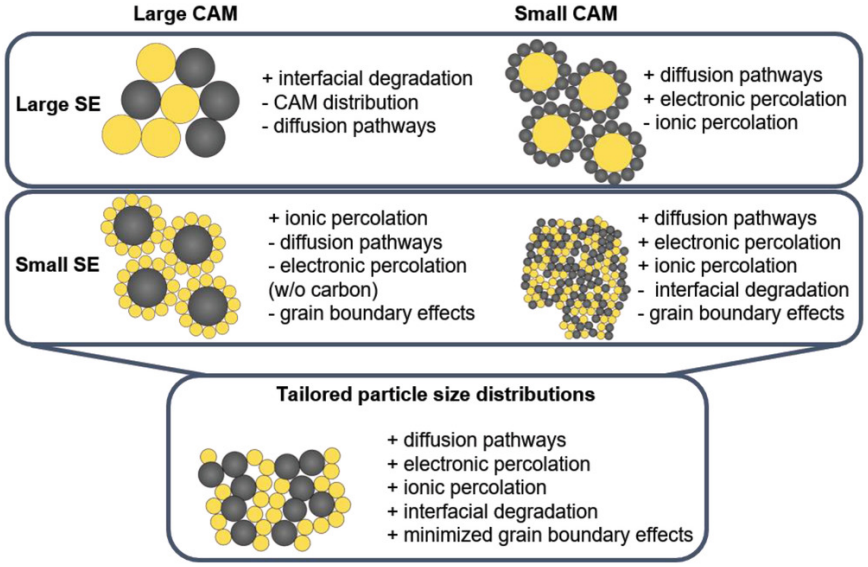

Figure 2.11: The factors to be considered for the design of the particle sizes of the CAM and the SE are interfacial degradation, electronic conductivity, ionic conductivity, diffusion pathways, and grain boundary effects [6].

Large CAM particles combined with large SE particles have the advantage of decreased interfacial degradation, conversely, this results in poor electronic and ionic diffusion pathways. Decreasing the SE particle sizes will lead to an increase in ionic conductivity, but also to a decrease in electronic percolation and grain boundary issues within the SE. Small CAM particles combined with large SE will increase the diffusion pathways within the CAM, as well as increase the electronic conductivity. However, the large

SE particles still hold the characteristic of poor ionic conductivity when compared to a smaller SE particle size. Having both a small CAM and a small SE particle size results in enhanced diffusion pathways, and electronic- and ionic percolation [48]. However, the interfacial degradation with smaller particles is significantly increased as a result of the increased surface area of the particles and thus a greater opportunity for surface degradation to occur. For those reasons, Minnmann et al. [6] makes the case for a tailored particle size distribution, which will result in optimal performance in all mentioned factors.

The work of Shi et al. [10] studied the optimization of the relative particle size (λ) on CAM utilization, and observed that a relative particle size of 1.67 would be required to achieve full cathode utilization at a CAM weight percentage of 70wt%. Similar CAM utilization values were obtained using CAM of 5μm and 12μm. Therefore, it is validated that CAM utilization is indeed related to the change in λ. As stated in section 2.1.5 Choice of Cathode Active Material, the particle size of the commercially available NMC811 is 10-13μm, the optimized SE particle size would therefore be approximately 6-7μm.

* * *

2.3. Conductive Carbon Additives

The cathode of SSBs is composed of cathode active material and solid-electrolyte, optionally a polymeric binder or interlayer and carbon conductive additives can be introduced to the electrode. Conductive carbon additives play an important role in boosting the cycling performance of SSBs. Important to note is that the conductive carbon additives do not participate in the electrochemical process of the SSB cell. Still, they can decrease internal resistance and therefore improve power density and specific power of the cell [49]. However, major issues were reported by Zhang et al. [50], showing long-term capacity fading of thiophosphate-based SSBs when using conductive carbons. In this subsection, the reasoning for and against the use of conductive carbon additives is discussed. Furthermore, the types of conductive carbon additives and the choice of preference are elaborated on. Finally, the gravimetric weight percentage of conductive additives for optimal performance is determined.

2.3.1. Working Mechanism of Conductive Carbon Additives

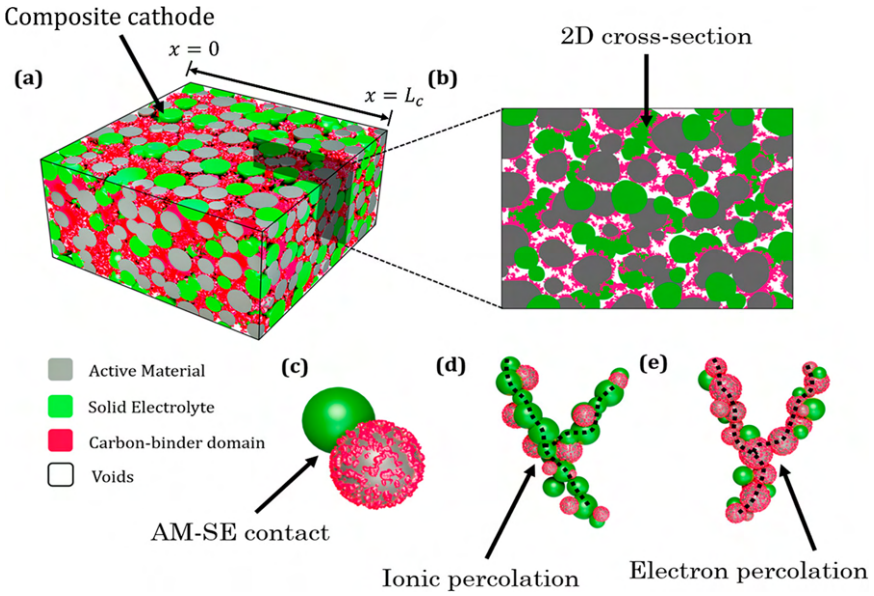

Figure 2.12: a) Schematic representation of a composite cathode consisting of CAM, SE, Carbon-Binder Domain (CBD), and voids b) cross-sectional view of the cathode microstructure. Microstructural composition of key elements, such as c) active contact area, d) ionic percolation, and e) electronic percolation pathways [11].

Conductive (carbon) additives can enhance the electron percolation pathways of the electrode [49], however, at the interface with the argyrodite (SE) the conductive additives can potentially lead to degradation with the creation of secondary phases [51]. A schematic representation of a composite cathode for SSBs is displayed in figure 2.12, where the microstructure of the cathode is split up into grey particles representing the CAM, green particles representing the SE, pink particles representing the carbon-binder domain (CBD), and the voids are displayed in white [11]. The CBD is a mixed phase formed by carbon and binder material, enhancing mechanical stability and electronic connections [52]. Figure 2.12c, gives a representation of the particle-particle contact of CAM and SE, unlike cathodes with LE the cathode in SSBs is not fully wetted. Figure 2.12d, displays the ionic percolation pathways within the SE. Figure 2.12e represents the electron percolation pathways, which can enhance the effective electronic conductivity of the electrode.

Despite the improved electronic conductivity offered by the conductive carbon additives, the formation of secondary phases upon electrochemical cycling forms major issues. The secondary phases can

impede the ion and electron pathways, increasing the tortuosity of the electrode. Additionally, such interphases can obstruct the solid-solid contact of the CAM and the SE, leading to increased resistance [53]. It can be concluded that the effect of conductive carbon additives may have a positive or a negative effect. Therefore, cells with and without electronically conductive additives will be constructed and tested in this study.

2.3.2. Types of Conductive Carbon Additives

The effect of commercial carbon additives within a SSB has been previously described in a study by Zhang et al. [50], some notable results and differences in the variations of conductive carbon additives will be discussed briefly to argue the selection of conductive additive for this study. As mentioned in section 2.1.4 *Choice of Electrolyte*, the decomposition of SE is a major issue [29]. All the while, changing the composition of argyrodite and making it more electrochemically stable, is difficult. Therefore, it is vital to control the kinetics within SSBs by selecting the appropriate morphology and weight percentage of conductive carbon additives [4].

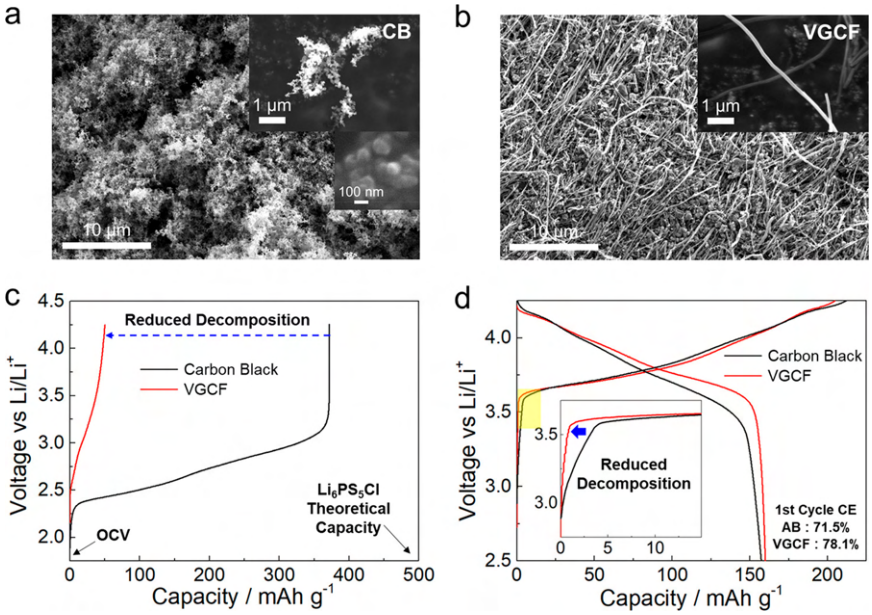

Figure 2.13: Scanning Electron Microscope (SEM) images displaying the morphology and size differences of a) carbon black (CB) and b) vapor-grown carbon fiber (VGCF) c) charge profile of LiIn | Argyrodite | NMC811 cells using 30 wt% CB vs VGCF d) Electrochemical cycling voltage profiles of LiIn | Argyrodite | NMC811 cells using 1 wt% of CB vs VGCF [4].

A large variation of commercially available carbon additives exist, such as Ketjenblack, Denkablack, C65, and vapor-growth carbon fiber (VGCF . Their specific surface area is 1454 m^2/g, 68 m^2/g, 62 m^2/g, and 24 m^2/g, respectively [54]. A distinct difference in morphology and particle size of the conductive carbon additives can be made, as displayed in figure 2.13 [4]. Carbon Black (CB) has a higher specific surface area, due to its nanosized particles (fig. 2.13a), whereas vapor-growth carbon fiber has a significantly lower specific surface area (fig. 2.13b). Such differences promote decomposition kinetic . Research by Tan et al. [4] showed that the use of low specific surface area conductive additives reduces the decomposition of the SE, as the results shown in figure 2.13c. Here, the effect of using 30 wt% of the different conductive additives showed increased decomposition kinetics and a higher total capacity decay for CB vs VGC . Another effect of using low specific surface area conductive additives can be seen in figure 2.13. Displayed is the first charge and discharge cycle of a $Li_{0.5}In$ | Li_6PS_5Cl | NMC811 cell using 1 wt% of each conductive carbon additive. The SSB cell with VGCF showed a higher coulombic efficiency, the charge efficiency of electron percolation, and a reduced electrolyte decomposition profile.

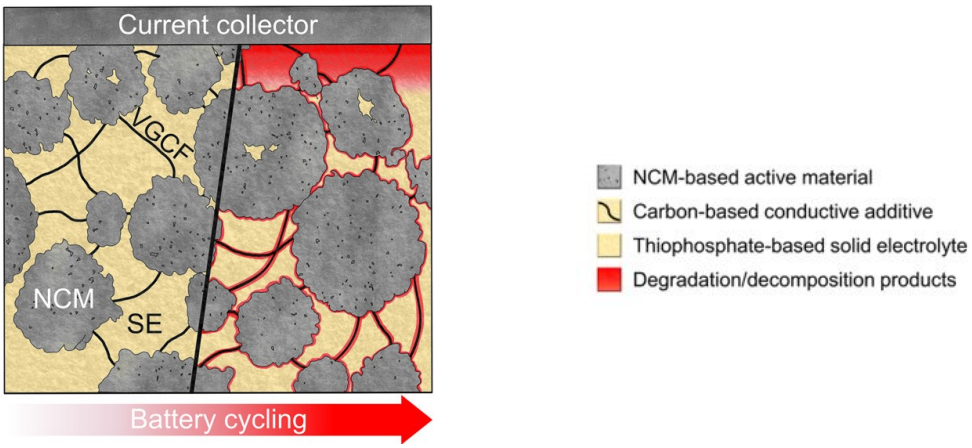

Figure 2.14: Schematic overview showing the degradation effects within the cathode electrode based on NMC, thiophosphate SE (Argyrodite), and VGCF due to electrochemical cycling of the SSB. Image includes decomposition reactions at the interface of the SE to the current collector, the CAM, and the conductive additive. Image adapted from Walther et al. [12].

The conductive carbon additive, carbon nanofibers (CNF) from Signma-Aldrich, is selected for this study, due to its low specific surface area reducing the effect of SE decomposition, while maintaining a high level of coulombic efficiency. The specifications for the CNF are listed in Appendix A. Higher initial capacity is expected with the use of CNF as a conductive additive, however, cycling degradation is expected to increase making the usage of CNF detrimental to the life cycle performance of SSBs. Displayed in figure 2.14, cycling the battery will not only result in degradation at the interface of the SE to the current collector and the CAM, but also to the CNF [12]. For this study, SSBs with and without conductive carbon additives will be constructed and tested. In addition, the decomposition reaction at the interface of the Li_6PS_5Cl to the CNF will be analyzed using electrochemical impedance spectroscopy (EIS) and X-ray Photoelectron Spectroscopy (XPS).

2.3.3. Gravimetric percentage of Conductive Carbon Additives

Besides selecting the most suitable type of conductive carbon additive, it is crucial to decide upon the correct weight percent to ensure improved cycling performance and limit degradation over time. Research has shown that a balance between ionic and electronic conductivity is vital for battery performance. Han et al. [55] discovered that using conductive additives with a 25wt% and thiophosphate solid-electrolyte, the SE severely decomposed upon electrochemical cycling of the cells. Another study on the effects of conductive additives by Zhang et al. [50], showed that even as little as 1.9wt% of C65 conductive additive increases the overall cell resistance over time and only keeps increasing with higher mass fractions.

The results in the study of Zhang et al. [50] were obtained using the conductive additive C65, which has a specific surface area of 62 m^2/g. The CNF selected for this study has a specific surface area of 24 m^2/g, ensuring a better coulombic efficiency and slower capacity decay compared to the C65 [4]. The work of Strauss et al. [56] displayed an improved cell capacity by adding 1wt% of C65 to pelletized SSB cell of a coated-NMC622 cathode, a $Li_4Ti_5O_{12}$ anode and an argyrodite Li_6PS_5Cl solid-electrolyte/seperator. With the electronically conductive additive with a lower specific surface area, it is expected that a slightly higher mass fraction can be added to the composite cathode mixture. In this study, 3wt% of CNF will be added to the cathode composite mixture, and the effect on the initial capacity, capacity decay, cell impendence, and the interfaces throughout the composite cathode will be analyzed for pelletized $Li_{0.5}In$ | Li_6PS_5Cl | NMC811 SSB cells.

* * *

2.4. Polymeric Interlayers as Protective Coating on Cathode Active Material

This chapter introduces the concept of polymeric interlayers in solid-state batteries, explaining their working mechanism, and elaborating on the different types of polymeric binders or coatings that could be used to improve the interface between the CAM, the Li_6PS_5Cl, and the carbon nanofibers. SSBs experience capacity deterioration caused by cracking of the CAM and contact loss between the CAM and the SE [6]. Another reason for rapid capacity fading is the formation of oxidized secondary elements [4]. The application of a thin polymer coating on the NMC811 particles can help stabilize the cathode-electrolyte interface, improving cycling performance by suppressing the formation of oxygenated species, reducing particle cracking, and limiting contact loss [20]. Firstly, the working mechanism and the definition of a polymeric binder and a polymeric coating are explained. Secondly, this chapter will elaborate on a multitude of polymers as candidates for this study. Then, this chapter introduces application strategies for polymeric protective coating. Finally, a selection of the most suitable polymers to form a protective coating is made for this study.

2.4.1. Working Mechanism of Polymeric Binders and Protective Coatings

The ionic transport mechanism of polymer electrolytes was briefly introduced in section 2.1.3. The most important thing to note is that the transport mechanism of polymer electrolytes is quite different from that of inorganic solid electrolytes. As shown in figure 2.3, the ion percolation is a result of chain segment motions and rearrangements of the polymer chain. For inorganic solid electrolytes, the cations are transported through the crystal defects in the crystalline structure of SE.

Contrary to inorganic solid electrolytes, polymers do not conduct ions by default. Ionic conduction can be induced in polymers by introducing ion conducting groups, such as ionic liquids or lithium salts [57]. The polymers function as a structural backbone with favorable mechanical and electrochemical stability, to which ionic liquids can bond. These properties are the reason for its application in SSBs.

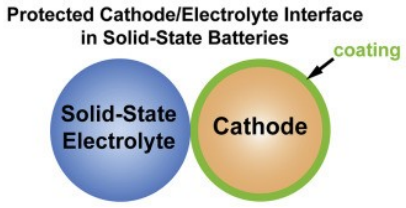

Figure 2.15: Schematic representation of a cathode surface coating as a solution to high interfacial resistance between cathode and solid-state electrolyte [13].

To mitigate the interfacial issues between the CAM, argyrodite, and carbon nanofibers, the NMC particles or the SE could be coated with a polymeric buffer layer [13]. In practice, the buffer layer, or polymeric coating, is usually applied to the cathode as it would significantly decrease the ionic conduction if applied to the S . This polymeric protective coating on the CAM can slow down the decomposition reaction and reduce interfacial resistance between CAM and SE [51]. Some coatings might negatively influence ionic and electronic conduction. Therefore, this study only considers polymers with at least moderate ionic conductivity and for some even electronic conductivity. Most polymers are resistant and do not conduct electrons, for these polymers the addition of conductive additives (carbon nanofibers) is necessary [7].

2.4.2. PEDOT:PSS as a Mixed Ionic Electronic Conducting Protective Coating

Most polymers are intrinsic insulators, limiting the electronic conductivity within the cathode composite [15]. The addition of conductive additives can mitigate this problem. However, adding more non-active material to the cathode composite decreases the overall cell capacity. In addition, conductive additives in

combination with sulfide-based Li_6PS_5Cl face enormous challenges, as the enhanced electronic percolation increases the oxidation of sulfide-based SE during cycling [58]. A mixed ionic electronic conductor (MIEC) can be used to improve the electronic conductivity, the ionic percolation, as well as the (electro-)mechanical stability of the cathode.

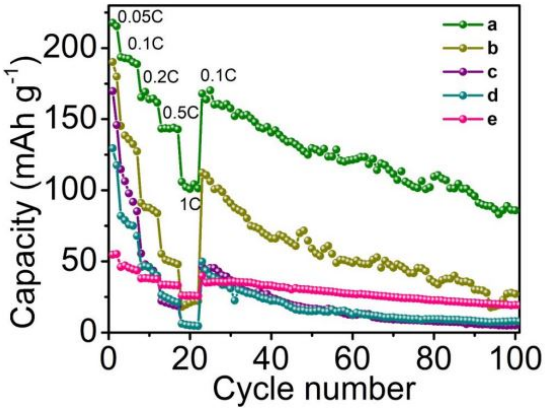

Figure 2.16: Capacity retention vs cycle number of multiple coating strategies in sulfide-based SSBs: a) PEDOT on NMC811 and CNFs, b) $LiNbO_x$ on MNC811 and PEDOT on CNTs, c) bare NMC811 and PEDOT on CNTs, d) PEDOT on NMC811 and bare CNTs, and e) PEDOT coating on NMC811 without CNTs [14].

Poly(3,4-ethylenedioxythiophene) (PEDOT) is an MIEC that displays moderate electronic conduction and outstanding mechanical properties. Consequently, PEDOT has found widespread application in various storage devices. For example, PEDOT was shown to be performance enhancing in lithium-ion batteries as a cathode binder [59], and in silicone batteries as an anode binder [60]. PEDOT has also been used as a protective coating for Ni-rich polycrystalline $LiNi_{0.85}Co_{0.1}Mn_{0.05}$ LIB cathodes, showcasing a capacity retention of 91% compared to 54% capacity retention of the uncoated cathode at 1C over 100 cycles [61]. Besides the various applications in LIBs, PEDOT has also been used in sulfide-based SSBs in a study by Deng et al. [14]. In this study, PEDOT was used as a protective coating on NMC811 particles and carbon nanotubes (CNTs) in $Li_{10}GeP_2S_{12}$ (LGPS) based SSBs, realizing significant improvements to the cycling performance of the cell with PEDOT coatings, as shown in figure 2.16.

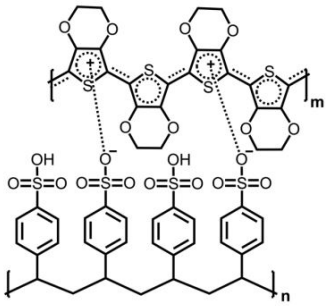

Figure 2.17: Chemical structure of poly(3,4-ethylendioxythiophene)/poly(styrene sulfonate) (PEDOT:PSS) [15].

Alternatively, poly(3,4-ethylendioxythiophene)/poly(styrene sulfonate) (PEDOT:PSS) is a commercially available polymer, similar to PEDOT, but doped by PSS further increasing the electronic conductivity of the polymer. The chemical structure of PEDOT:PSS is displayed in figure 2.17. The $-SO_3H$ groups in PSS are hydrophilic, making the PEDOT:PSS easily dispersible in water [15]. Spray-drying is considered a wet coating method and can form evenly distributed layers on NMC particles [51]. The hydrophilic characteristic of the additional PSS group can help with the coating formation on the NMC particle when using spray-drying as an application method. PEDOT:PSS has already been used as a binder for the cathode

composite in halide-based SSB in a study by Nazmutdinova et al. [15]. This resulted in increased electronic percolation and increased discharge capacity in the halide-based SSB. However, PEDOT:PSS has not seen any scientific publications as a protective coating in sulfide-based SSBs.

2.4.3. Polycarbonate-PEO as an Ionic Conducting Polymeric Protective Coating

Block polymers are designed to combine ionic conductivity with electrochemical stability and elastomeric mechanical properties [16]. Polycarbonate-poly(ethylene oxide), is an example of a triblock polymer with an ABA-block structure. Herein, "A" stands for a "hard" polycarbonate block, and "B" for the "soft" PEO block. The "A" block provides oxidative stability and enhanced mechanical rigidity. The soft "B" (PEO) block is known to be the golden standard matrix for solid polymer electrolyte [62]. However, the limitations of PEO are a relatively low lithium transference number and low ionic conductivity. PEO as a triblock polymer, with an ABA-block structure (PC-PEO-PC), ensures improved ionic conductivity, and mechanical and electrochemical stability.

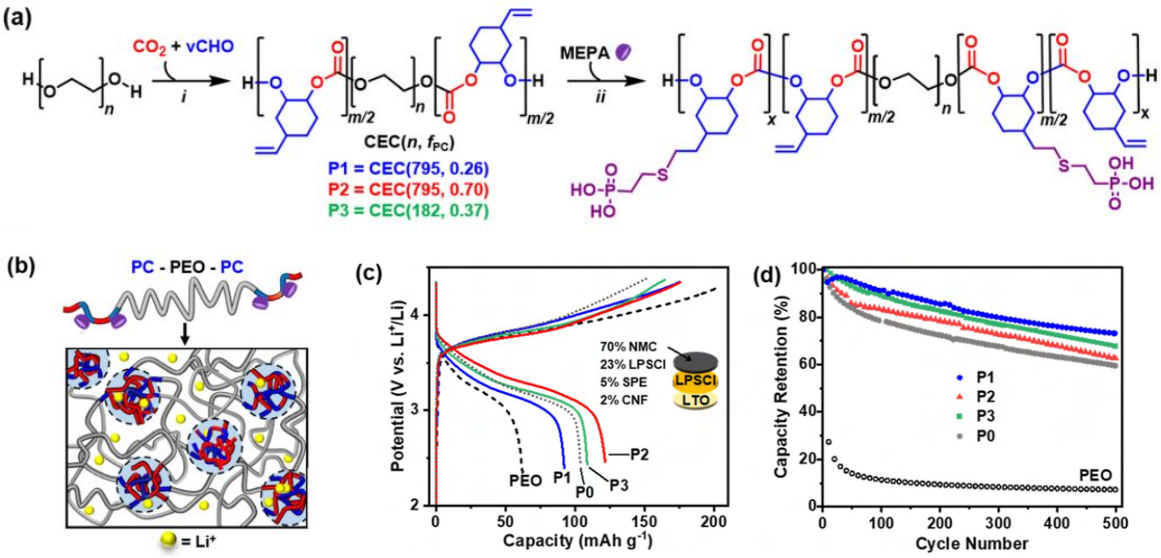

Figure 2.18: a) Reaction scheme: i) ring-opening copolymerization (ROCOP) of CO_2 with 4-vinyl cyclohexane oxide (vCHO) ii) UV-mediated reaction with phosphonic acid (MEPA . b) Schematic of the PC-PEO-PC, ABA-block structure. c) Charge-discharge voltage profiles with varying repeat units and volume fraction. d) Capacity retention vs cycle number. Image adapted from Gregory et al. [16].

Figure 2.18 a) displays the reaction scheme and the chemical structure of PC-PEO created in the study by Gregory et al. [16]. A schematic representation of PC-PEO-PC is shown in figure 2.18 b), here PEO is represented as the "soft" block sandwiched between the "hard" PC block. The mechanical and kinetic properties of the PC-PEO are dependent on the mid-segment length of PEO, namely the repeat units of ethylene ozides (n), and the volume fraction of PC (f_{PC}. Short PEO mid-segments result in triblock polymers with unfavorable mechanical properties, excessively long PEO segments give rise to difficult processing characteristic. The optimized triblock polymer in the study of Gregory et al. [16] has a repeat unit between the values of $n = 182$ and $n = 795$, and a minimal volume fraction of PC of 0.25 ($f_{PC} > 0.25$) to ensure oxidative stability and sufficient mechanical stability.

Ring-opening copolymerization (ROCOP) chemistry was selected as the most suitable way to form the outer PC blocks of triblock polymer. This technique allows for excellent control over the chain end groups, molar mass, and overall composition of the polycarbonate blocks [63]. UV-mediated thiol-ene reactions are the method of choice to create stable polymer groups [64]. Phosphonic acid can be attached to the PC blocks creating a customized adhesion compatibility with the cathode active material. LiTFSI can be added to the mixture to increase the polymer's ionic conductivity, as shown in figure 2.18b).

The cycling results of the SSB with PC-PEO are displayed in figure 2.18c) and figure 2.18d) [16]. Here, **P0** is a cell without any polymer, **P1** is a cell with PC-PEO characteristics $n = 795$ and $f_{PC} = 0.26$, **P2** is a cell $n = 795$ and $f_{PC} = 0.70$, and **P3** is a cell with $n = 182$ and $f_{PC} = 0.37$. Initial charge capacity was highest for *P2*, followed in descending order by **P3**, **P0**, and **P1** (figure 2.18c). However, **P1** beats all other samples in terms of cycling retention with 86% after 200 cycles. In summary, polycarbonate-PEO block polymers are promising candidates for improving the conductivity and cyclicability of solid-state batteries.

2.4.4. Vulcanized Butadiene Rubber Binders

Vulcanized Butadiene Rubber (BR) can form a mechanically stable alternative to other reinforcing binders for sulfide-based solid-state batteries, under low or no external stack pressure [17]. In the work by Kwon et al. [17] the vulcanization of BR during a wet-slurry process formed a resilient crosslink structure, suppressing the (chemo-)mechanical degradation of the composite cathode. The results suggest that the integrity of the particle structure of the cathode, during electrochemical cycling, is maintained better compared to pristine BR.

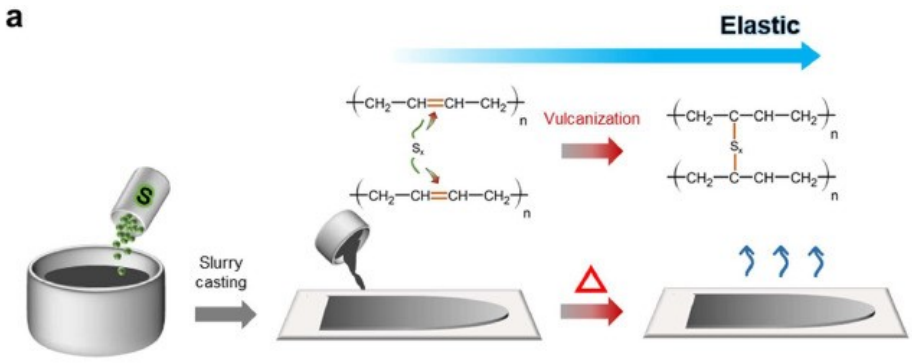

Figure 2.19: Schematic of the *in situ* formation of vulcanized BR binders during the slurry fabrication process for sheet-type electrodes [17].

The most commonly use method for the fabrication of sheet-type electrodes is wet-slurry casting, with solid-electrolyte infiltration and dry electrode technology [65]. Although this is a popular fabrication method, wet-slurry casting is a problematic process in combination with sulfide-based S . This is caused by the incompatibility and weak adhesion of sulfide-based SE with solvent and binders [66]. Kwon et al. [17] improved the adhesive characteristics of the mixture by crosslinking the BR binder, during slurry casting. The crosslinking process in which the BR chains are connected, forming a network of crosschained chemical compositions, is called vulcanization [67]. In the study by Kwon et al. [17], sulfur was added to the slurry crosslinking the butadiene rubber, thus vulcanizing the BR, schematically represented in figure 2.19.

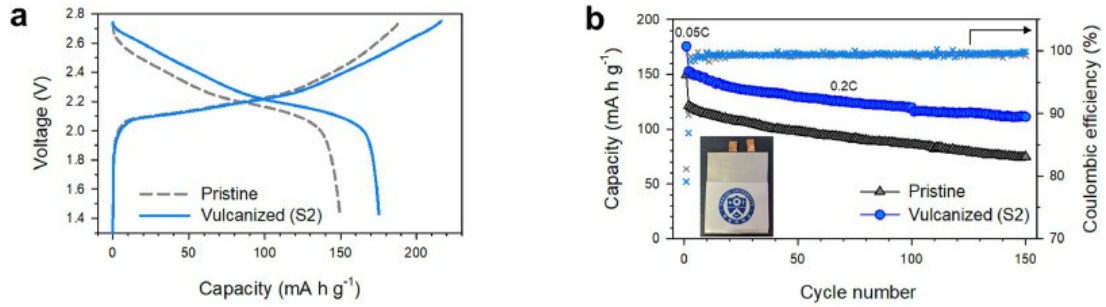

Figure 2.20: Electrochemical performance of pouch-type full cells employing pristine and vulcanized BR, operated under no external pressure. a) Charge–discharge voltage profiles of the pouch-type full cells at 0.05C, and b) cycling performances with a photograph of a pouch-type full cell [17].

Figure 2.20 displays the cycling performance of pristine and vulcanized B . Pristine BR refers to linear, or non-crosslinked, butadiene rubber. The initial capacity of the cycled pouch-type cells in the study of Kwon et al. [17] are shown in figure 2.20a), these results were obtained under no external stack pressure. Evidently, the initial capacity of the vulcanized BR is much higher than that of pristine BR (165 vs. 150 mA h g^{-1} at 0.05C, respectively. The capacity retention during cycling of the vulcanized BR also showed to be superior to that of the pristine BR, displayed in figure 2.20b. At the 150th cycle, the capacity retention of the cathode with vulcanized BR was 72.8% compared to the 2nd cycle, whereas the capacity retention for the cathode with pristine BR was a mere 61.8%. As has been demonstrated, the vulcanized butadiene rubber has the upper hand in terms of initial capacity, and capacity retention compared to pristine BR.

2.4.5. PDDA-TFSI as a Polymerized Ionic Liquid

Most polymeric binders in lithium batteries are inactive due to their inability to conduct lithium ions, resulting in lower power densities and cell capacities [19]. However, these inactive polymer binders are essential in lithium batteries to improve cycling lifetimes, by reducing degradation effect. One example of an inactive polymeric binder is the frequently used poly(vinylidene difluoride) (PVDF). Examples of active binders are poly(ionic) liquids or Polymerized Ionic Liquids (PILs). These are polymeric binders that can improve the electrochemical cycling performance of the cell, while also providing lithium ion conduction to enhance capacity values and power densities of the cell [68]. PILs have a large electrochemical stability window, are flexible, and conduct lithium ions due to the structure where a polymeric backbone is bonded with the ionic liquids, typically cationic or anionic groups [69].

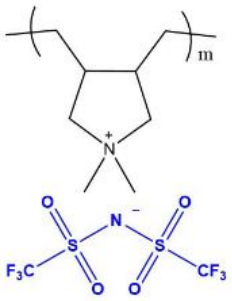

Figure 2.21: Chemical structure of poly(diallyldimethylammonium) bis(trifluoro- methanesulfonyl)imide (PDDA-TFSI), with the polymeric PDDA backbone in black, and the lithium salt LiTFSI in blue, adapted from Del Olmo et al. [18].

PILs can be used for a variety of scientific fields, such as CO_2 separation membranes [70], gel polymer

electrolytes [71], and binders for LIBs [19]. A frequently used PIL is the PDDA-based poly(diallyldimethylammonium) bis(trifluoro-methanesulfonyl)imide, PDDA-TFSI, or PDADMA-TFS. A schematic representation of the polymerized ionic liquid, PDDA-TFSI, is depicted in figure 2.21. In a study by Vauthier et al. [19], PDDA-TFSI was one of four PDDA-based PILS that were tested as a binder for LIBs. The PIL displayed to be thermally stable up to temperatures of 355°C, and improved cycling performance compared to polyvinylidene fluoride (PVDF), which is known for its high mechanical, thermal, and electrochemical stability [72]. However, the initial capacity of LIB with PDDA-TFSI seemed to be lower than the cell with conventional PVDF, as displayed in the charge-discharge voltage profiles and cycling performance graphs of figure 2.21 performance. Vauthier et al. [19] suggested that PDDA-based binders can play an important role in the development of solid-state batteries due to their intrinsic ionic conductivity, providing enhanced ionic percolation pathways. PDDA-TFSI has not seen any scientific publications as a protective coating in sulfide-based SSBs.

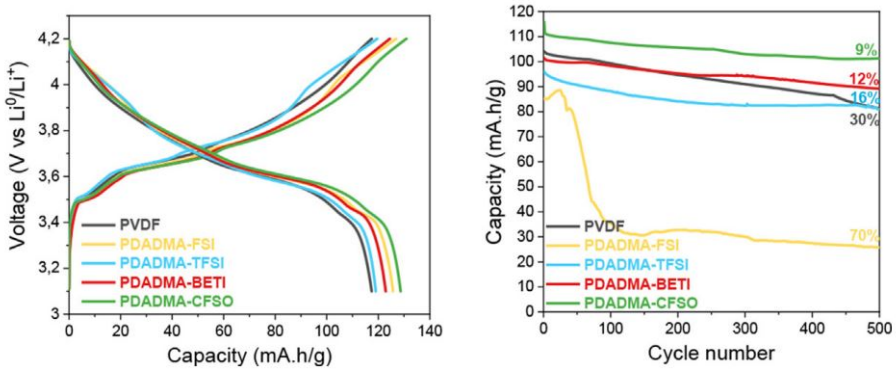

Figure 2.22: Electrochemical performance of pyrrolidinium-based poly(ionic liquid) binders in Li-ion batteries. a) Charge-discharge voltage profiles at 0.3C and 25°C, and b) capacity retention vs cycle number [19].

2.4.6. Protective Coating Application Strategies

The application of protective coatings on cathode active material can be done in many ways, two techniques are highlighted; spray-drying, and microencapsulation. Spray-drying is a technique that is used often in industry and is classified as a wet-coating method [73]. In the work of Shi et al. [20], spray-drying was used to obtain a uniform coating of poly((4-vinyl benzyl)trimethylammonium bis(trifluoromethanesulfonylimide)) (PVBTA-TFSI). Another often-used method for the application of surface coatings is microencapsulation. This method is based on using a solvent and an anti-solvent, making the soluble polymer collapse on the NMC particles [74].

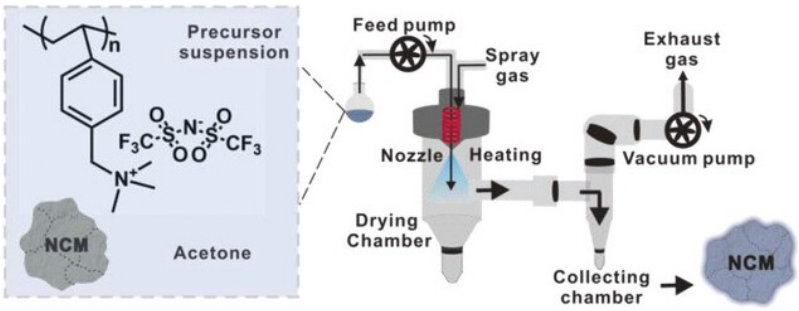

Figure 2.23: Schematic representation of the spray-drying surface coating process of NMC particles after collection the NMC is further dried in vacuum [20].

A schematic representation of the spray-drying method of NMC particles from the study of Shi et al. [20], is displayed in figure 2.23. For a coating to function properly, the adhesion of the coating material to

the NMC particles is crucial. Ionic groups in the discussed polymers have strong electrostatic interaction with the metal-oxide surfaces, such as that of the NMC particles [75]. During spray-drying, the size of the sprayed droplets compared to the particle size of the NMC determines if a uniform coating is formed on the NMC particles. Droplets with the polymer solution should have a greater diameter than the NMC particles to form a uniform protective coating, as shown in the study of Shi et al. [20]. Here, dry-spraying proved to be a successful technique to coat NMC particles, which in turn significantly improved the cycling performance, by decreasing the detrimental effects of volume changes and cracking of the NMC particles.

Microencapsulation is a technique used in a wide variety of commercial applications [76]. The process is usually carried out in two steps [74]. First, a solution of the soluble polymer is created, and the insoluble NMC particles are present in the solution. Then, an anti-solvent is added to the solution, ensuring the envisioned protective polymer collapses on the NMC particles, creating a homogeneous coating on the surface of the NMC particles. Microencapsulation has been used successfully to coat graphite anode material [77], and to coat cathode active material with flame retardants[78], both in LIBs. Regardless of the popularity of this coating technique in Li-ion batteries, the adaptation of this technique for solid-state batteries is limited.

2.4.7. Choice of Polymeric Protective Coating

The application of ion-conducting polymers as protective coatings on cathode active material has gained popularity among researchers as it has the potential to resolve many of the interface issues between cathode active material, solid electrolyte, and conductive additives[20]. Issues related to the cathode interface are mechanical and (electro-)chemical [16], as described previously in section 2.2.1 Chemo-Mechanics and Kinetics During Electrochemical Cycling. It is important to understand that the kinetics, electronic and ionic percolation, within SSBs must be improved to compete with conventional LIBs. Sulfide-based SE, such as argyrodite, shows ionic conductivity similar to that of liquid electrolyte counterparts. However, argyrodite has shown to be incompatible with conductive additives [58], which ensure electronic conductivity.

In summary, to increase the performance of argyrodite-based SSBs, polymeric protective coatings should i) buffer volumetric changes to avoid contact loss between the CAM and the SE, ii) be electrochemically stable to avoid electrochemical decomposition, and iii) enhance ionic, or electronic, conductivity to improve the electrochemical kinetics. Specifically for this study, the commercial availability of the polymer is a factor that is also considered. This literature review covered four candidates up for consideration for this study, namely; PEDOT:PSS, PC-PEO, butadiene rubber, and PDDA-based polymers. Following is the reasoning for the selection or discarding of the four studied polymer candidates:

- PEDOT:PSS is unique for its ability to conduct ions as well as electrons, caused by the additional PSS group [15]. A relatively similar structure, PEDOT, also displayed significant improvements to the capacity and cycling performance as a protective coating on the NMC particles and CNTs in LGPS-based SSBs [14]. PEDOT:PSS has been used as a binder in halide-based SSBs, displaying an increased electronic percolation and discharge capacity. The conducted research makes a strong case for using PEDOT:PSS as a polymeric protective coating for sulfide-based SSBs.

- PC-PEO has great mechanical and electrochemical stability properties, due to the 'hard-soft-hard' triblock polymeric structure. However, this polymer has already been used as a binder in LPSCl-based SSBs in a study by Gregory et al. [16]. In this study the PC-PEO triblock polymer was synthesized in-house, creating a multitude of chain lengths and polycarbonate volume fractions. PC-PEO is not commercially available, making this an unsuitable candidate for this specific study.

- Vulcanized Butadiene Rubber (BR) has great mechanical characteristics, and the initial capacity of an SSB with vulcanized BR is superior to that of one with non-vulcanized BR [17]. In the study by Kwon et al. [17], wet-slurry casting was the selected method to apply vulcanized BR as a binder in sulfide-based SSBs. However, due to the non-polar nature of BR, this polymer will not stick to the

NMC particles. Therefore, vulcanized BR is not a suitable candidate to form polymeric protective coatings in the cathode composites of this study.

- PDDA-based polymerized ionic liquids, have properties similar to that of conventional PVDF. However, whereas PVDF functions as an insulator, PDDA-based polymers with ionic liquids can conduct ions to a greater extend [69]. The best-performing PDDA-based PIL in LIBs in the study of Vauthier et al. [19] was PDDA-CFSO; however, PDDA-CFSO is not commercially available. The second-best commercially available PIL is PDDA-TFSI, and will therefore be part of this study to improve the performance and cycling lifetime of sulfide-based SSBs.

3

Materials and Methods

This chapter introduces the procedures for preparing solid-state batteries, the methods to assess their performance, and the techniques to analyze the degradation mechanics. First, the types of materials and the assembly procedures of the multiple components of the SSBs are introduced. Second, the application method of the polymeric interlayers on the cathode active materials is described. Subsequently, the electrochemical cycling for the SSB performance testing is explained. Finally, the characterization techniques used in this study, Electrical Impedance Spectroscopy (EIS), X-ray Photoelectron Spectroscopy (XPS), Scanning Electron Microscopy (SEM), and X-ray Diffraction (XRD), are briefly introduced.

3.1. Preparation of the Cathode Electrode Composites

The cathode composites of the solid-state batteries tested in this study were prepared using a mixture of argyrodite (Li_6PS_5Cl, D_{50} = 5 μm), with polycrystalline NMC811 particles ($LiNi_{0.8}Mn_{0.1}Co_{0.1}O_2$, D_{50} = 10 - 13μm, 200 mAh/g) from the NEI Corporation, or with single crystal NMC Ni82 ($LiNi_{0.82}Mn_{0.07}Co_{0.11}O_2$, D_{50} = 3 - 5μm, 200 mAh/g) from MSE Supplies LLC, material specifications are listed in appendix A. First, 70 milligrams of NMC was carefully weighed on an analytical balance. An analytical balance is an accurate laboratory balance with measurement accuracy up to 0.1mg. After this, 30 milligrams of argyrodite was weighed. Both powders were added to an agate pestle and mortar and hand-mixed for 15 minutes. An agate pestle and mortar was used, as it has a high hardness, and a very fine grain structure for easy cleaning, reducing the chances of cross-contamination with other sample materials.

Multiple compositions of cathode composites were created by mixing additional materials, such as conductive additives, or by using NMC particles with coatings of different thicknesses instead of the pristine NMC. The cathode composite for testing the effect of carbon nanofibers (CNFs), a conductive additive, was made with CNFs purchased from Sigma Aldrich. The material specifications are in appendix A. For this sample set, 70 mg of NMC811 particles were mixed with 3mg of CNF before mixing it with 27 mg of argyrodite. This composition ensures a similar cathode active mass loading.

The cathode composite for the samples with polymeric protective coatings was created by replacing the 70mg of pristine, uncoated NMC particles with particles coated with polymeric protective coatings. The protective coating on the NMC particles has a varying thickness, dependent on the weight percentage of polymer added to the solution during the coating application process. The formation of the solution and the application process of the polymeric protective coating is described in more detail in section 3.2 Polymer Coatings on the Cathode Active Material.

3.2. Polymer Coating Application

For this study, multiple application strategies have been looked at to create a uniform protective coating of even thickness on the surface of the NMC particles. The advantages and disadvantages of these strategies have been briefly touched upon in section 2.4.6 Protective Coating Application Strategies. Both application strategies have been used; the settings and process steps will be described following the decision-making for the polymer interlayer application for this study.

The spray-drying installation used in this study is the Buchi Mini Spray Dryer S-300. The laboratory spray dryer has maximal flexibility, allowing for a custom application approach [79]. Before spray-drying, a solution of 1 gram of NMC, 25mL of acetone, and 1wt% or 3wt% of the studied polymer was added to the solution. In this case, 10mg and 30mg of PDDA-TFSI was added to create the 1wt% and 3wt% PDDA-TFSI samples. This solution was stirred at 500 rpm for 45 minutes to create a fully suspended solution, after which it was fed into the Bunchi Mini Spray Dryer with the following settings. Drying Gas: 35 m^3/h, Inlet Temperature: 150 °Celsius, Spray Gas: 1800 L/h, Pump 1: 4 mL/min, Outlet Temperature: 200 °Celsius, Deblock: 20 bpm. After spray-drying, the coated NMC particles were collected in the collection chamber and further dried overnight in a vacuum oven at 80°Celsius. The coated NMC particles were used to prepare the cathode composite as described in the previous sub-section 3.1, Preparation of the Cathode Electrode Composites. Figure 2.23 presents a schematic overview of the application method.

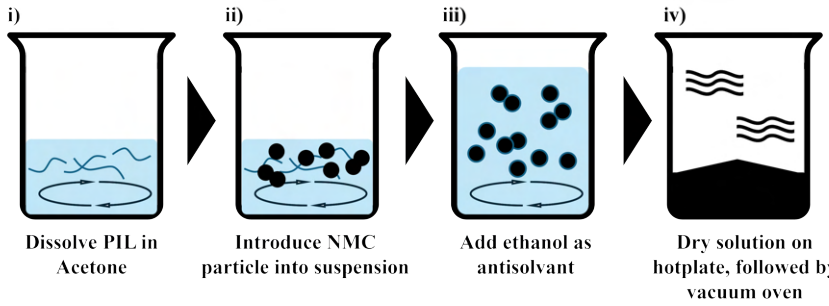

Figure 3.1: Schematic representation of the carried out microencapsulation coating process.

Microencapsulation is the second technique that has been used to coat the NMC particles with a polymer protective layer. First, for the PDDA-TFSI coating, 10mg and 30mg was weighed and dissolved, each into 25mL of acetone - here the acetone acts as a solvent for the polymer. Then, 1g of NMC particles, which are insoluble in acetone, were added, creating a suspension. The ratio of 1g NMC to 10mg or 30mg of PDDA-TFSI creates a 1wt% and a 3wt% coating of different thicknesses. The suspension was stirred at 500rpm for 30 minutes, after which 25mL of ethanol was added. Here, ethanol was used as an anti-solvent. The suspension with ethanol was stirred for 10 minutes at 500rpm, making the polymer precipitate on top of the NMC particles. The liquids were later evaporated by setting the suspension on a hotplate while stirring, leaving only the coated NMC particles behind, which were dried overnight in a vacuum oven at 80°Celsius. Figure 3.1 presents a schematic overview of the described process.

In the later stages of this study, PDDA-TFSI was mixed with LiTFSI to enhance the ionic conductivity of the polymeric protective coating. This specific coating was only used on single-crystal NMC, Ni82. A 1:1 mole ratio of PDDA-TFSI to LiTFSI was used to optimize the Li^+ transference number without creating a crystalline phase of the Li-salt. Wang et al. [80], showed that at mole ratios above 1:1.15, crystalline phases would form for PDADMA FSI:LiFSI. The formation of a crystalline phase leads to a decreased ionic diffusion coefficient and should, therefore, be avoided. The selected 1:1 ratio is deemed to be on the safer side, this could however be further optimized.

The molar weight of LiTFSI is around 287 grams per mole [81]. The repeating monomer unit of PDDA-TFSI is similar to that of Pyr13TFSI, and has a molar weight of around 408 grams per mole [81]. To create a 1:1 mole ratio, a 287:408 weight ratio was used. For the coating on 0.75g of single-crystal NMC, Ni82, 15mg

of PDDA-TFSI:LiTFSI was made by mixing 6.2mg of LiTFSI with 8.81mg of PDDA-TFSI. This results in a 2wt% coating of PDDA-TFSI:LiTFSI on the single-crystal NMC. Due to the tendency of LiTFSI to absorb moisture from the air, the microencapsulation process was performed in a glovebox. First, the 6.2mg of LiTFSI and the 8.81mg of PDDA-TFSI was added to 5mL of acetonitrile, which was mixed forming a homogeneous solution. Afterward, 0.75g of single-crystal NMC was added, forming a suspension that was mixed for 60 minutes. Stirring was performed using a magnetic stirrer with the suspension in a closed bottle, which did not allow the evaporation of the solvent. After 60 minutes, the bottle cap was removed, and the suspension was dried on a hotplate at 60°Celsius, with continued stirring. Finally, the remaining solution was placed in a vacuum antechamber to further dry overnight.

3.3. Solid-State Battery Cell Assembly

This study creates full solid-state batteries, meaning an anode, cathode, and separator are prepared for testing and pre- and post-cycling analysis. The prepared solid-state battery is made between two steel cell parts denoted with A and B in figure 3.2. In between the steel parts, surrounded by the PEEK sleeve, the argyrodite separator, the cathode, and the Lithium-Indium anode were prepared in that respective order. The diameter of the compressed cell is 10mm, giving the cell a surface area of ≈0.8cm^2 which is getting compressed.

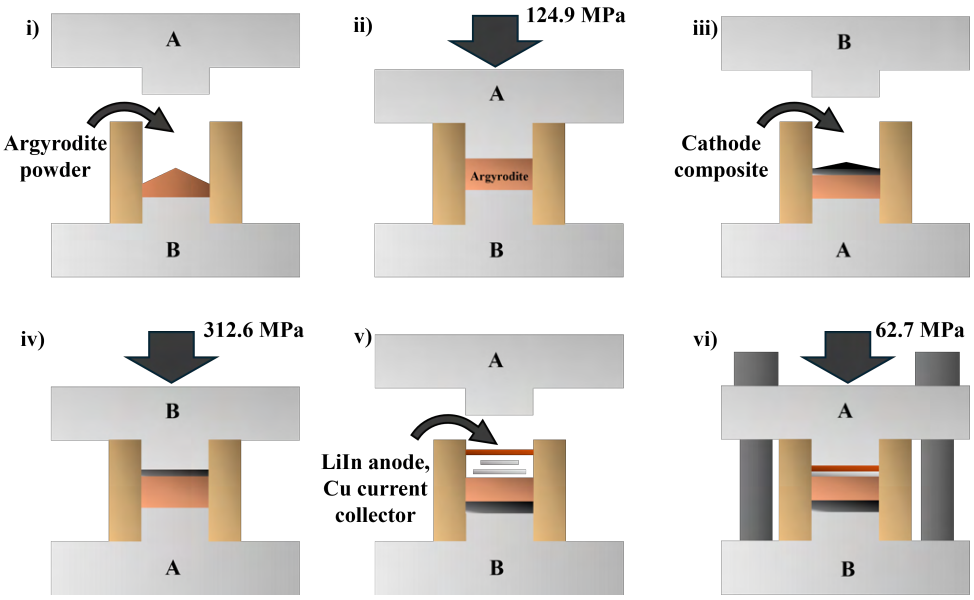

Figure 3.2: Schematic representation of the solid-state battery assembly procedure. In step iii) and iv) the cell is turned upside down for the preparation of the cathode.

First, the PEEK sleeve was placed on the steel cell part B. After this, 60 milligrams of argyrodite was carefully weighed and evenly spread inside the PEEK on top of the steel cell part. The second steel cell part, part A, was placed on top and together placed in the press, where the argyrodite separator was compressed at 124.9 Mpa of pressure for 1 minute. After retrieval from the press, the argyrodite pallet was checked for cracks, or other deformations, before proceeding with the following steps.

After opening the cell and examining the separator, 12mg of any of the created cathode composites is added to one side of the separator. All cathode composites consist of 70wt% of NMC active materials, by making cathodes of 12mg the cathode active loading is kept constant for all created solid-state cells. Cathode active loading was ≈10mg/cm^2, or 2mAh/cm^2, assuming a rated capacity of 200mAh/g for the NMC. The cathode composite is, again, carefully spread inside the PEEK on top of the argyrodite separator

before closing the cell with cell part B and placing it back in the press. The upper limit for the compressing on the cathode is set at 312.6 MPa of pressure for 5 minutes.

Finally, the Lithium-Indium anode of the solid-state battery is made by pressing a Lithium foil on the back side of an Indium foil, creating a metal alloy functioning as the anode of the SSB. An indium foil with a diameter of 8 millimeters is placed on the argyrodite separator, after that lithium foil with a diameter of 5 millimeters is placed on the indium foil. The weight ratio of Indium to Lithium was optimized per the work of Santhosha et al. [5]. Before closing the cell with cell part A, a 10-millimeter diameter copper foil is placed between the LiIn alloy and the steel cell part. The full cell is placed in the press and closed at 62.7 MPa. Three bolts are tightened, keeping the closing pressure of the cell at roughly 62.7 MPa. Figure 3.2 presents a schematic overview of the described procedure.

3.4. Electrical Measurements and Cell Cycling

The electrochemical cycling of the batteries was performed on the MACCOR workstation. The solid-state batteries were charged and discharged between 2.15V and 3.7V. The upper cutoff potential was 3.7V - corresponding to 4.3V vs Li^+/Li - as the capacity deterioration is significantly increased for higher cutoff potentials [82].

The first two cycles are run at a C-rate of C/20, 0.05C, meaning one-twentieth of the theoretical battery capacity is being charged per hour. These first two formation cycles ensure a stable solid electrolyte interphase on the anode, preventing irreversible consumption of lithium ions [83]. After the second cycle, the batteries are charged to a potential of 3.0V, and the first electrochemical impedance spectroscopy (EIS) measurements are taken. The following 100 cycles are run at a significantly higher C-rate of C/5, or 0.2C, which is a faster, more representative charging rate. After cycle 100, the battery is charged to 3.0V, and a post-cycling EIS measurement is taken. For all varieties of batteries, a minimum of two samples are created for cycling performance testing. This is done to normalize the generated results and reduce the chances of a one-off event of good or poor battery performance.

3.5. Electrochemical Impedance Spectroscopy

Electrochemical Impedance Spectroscopy (EIS) is a frequently used technique in semiconductor science and storage technology research [21]. This technique is non-destructive, which means it can be used to create an understanding of the manufactured sample without affecting the characteristics or the future performance. As it can relate the performance degradation with the impedance evolution, EIS has become an important pre-, and post-cycling analysis tool in battery research [84].

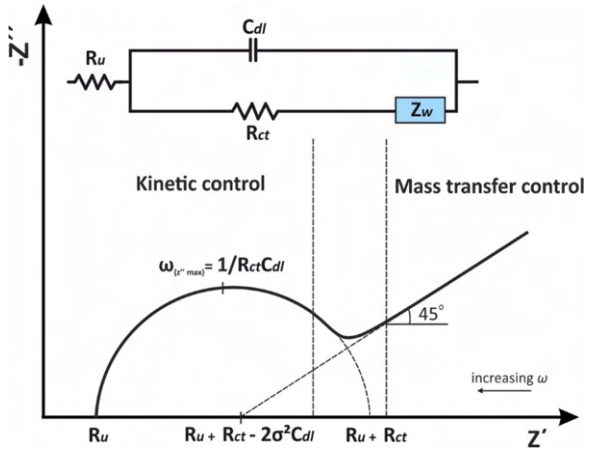

Figure 3.3: Randles equivalent circuit, and Nyquist plot for a wide range of frequencies [21].

EIS data is generally represented in a Nyquist plot, as the example presented in figure 3.3. The plot can be broken up into two domains, the high-frequency domain where kinetics control the ionic transport, and the low-frequency domain where mass transfer mechanics control ionic transport [21]. Figure 3.3 also displays Randles equivalent circuit, often used to model an electrochemical system's kinetic and mass transport. Here, R_u represents the electrolyte resistance, C_{dl} the double layer capacitance, R_{ct} the charge transfer resistance, and Z_w the Warburg impedance [21].

In this study, electrochemical impedance spectroscopy was used to study the interface resistance of the batteries pre-cycling as well as post-cycling. The first EIS measurement was taken after the batteries completed two formation cycles and were charged to a potential of 3.0V. The second EIS measurement is taken after 100 cycles. Measurements were taken between 10 MHz and 1Hz, to measure both the kinetic control domain, translating to the bulk SE resistance, and the charge transfer control domain, involved with solid-electrolyte separator/electrode resistance and the ionic resistance across NMC and SE interfaces [47]. In later measurements for single crystal NMC, lower frequencies up to 0.1Hz were applied.

A challenge in EIS measurements analysis lies in accurately fitting an electrical equivalent circuit to the system under investigation. Each element within the circuit must correspond to a distinct physical property, such as the bulk-, SE-electrode-, and charge transfer resistance. However, prior knowledge of the impedance linked with each element is needed to select the circuit components appropriately. Consequently, a Distribution of Relaxation Times (DRT) analysis is conducted, serving as a technique to aid in the fitting of an equivalent circuit to the impedance data [85].

3.5.1. Distribution of Relaxation Times

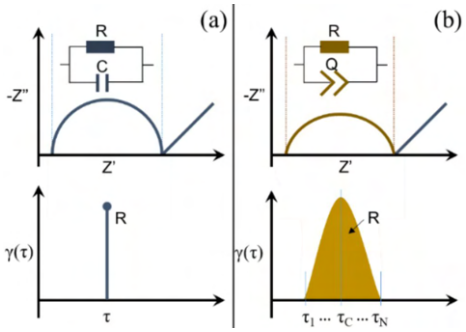

Figure 3.4: DRT plots for a) R/C parallel circuit elements, and b) R/Q parallel circuit elements [22].

The Distribution of Relaxation Times is a Fourier Transform of the electrical impedance data that can analyze the number of polarization processes causing internal voltage losses[86]. The ideal R/C parallel circuit represented in Randles equivalent circuit is a simplified representation of the physical system. The R/Q parallel circuit describes the real physical system, where Q is a Constance phase element modeling the behavior of a double layer [87]. The DRT of an ideal parallel circuit gives a Dirac, whereas the DRT of the R/Q parallel circuit element returns a parabola (see figure 3.4 [22]). The R/Q parallel circuit elements impedance can be described by [88]

$$Z_{RQ} = \frac{R}{\left(1 + j\omega RC\right)^{\varphi}} \tag{3.1}$$

Where R is the resistance, ω is the angular frequency, and C is the capacitance. For the ideal R/C parallel circuit, the time constant is given as

$$\tau = \frac{1}{2\pi \mathrm{f}} = RC \tag{3.2}$$

With the expression for the time constant (τ), the DRT curve (fig 3.4b)), can be split in n number of R/C circuit elements, which can be expressed as

$$Z_{DRT} = \sum_{x=1}^{n} \frac{R}{(1+j\omega\tau)} = \int_{\tau_1}^{\tau_n} \frac{\gamma(\tau)}{(1+j\omega\tau)} d\tau, x = 1...n \tag{3.3}$$

where the distribution of polarization at each time constant is described by $\gamma(\tau)$. Individual process resistances, both in the kinetic control domain and the charge transfer control domain, can be described by [22]

$$R = \int_{\tau_1}^{\tau_n} \gamma(\tau) d\tau \tag{3.4}$$

The benefit of performing a DRT analysis is that the impedance data can be interpreted more easily, without prior knowledge of an equivalent circuit. Using the RelaxIS 3 software, DRT analysis was performed to find an equivalent circuit for the interface resistances of the pre-, and post-cycled solid-state batteries. In this study, the impedance data was used in the DRT analysis, revealing an equivalent circuit, which was fitted to the original impedance data to quantify the interface resistances.

3.6. X-ray Photoelectron Spectroscopy

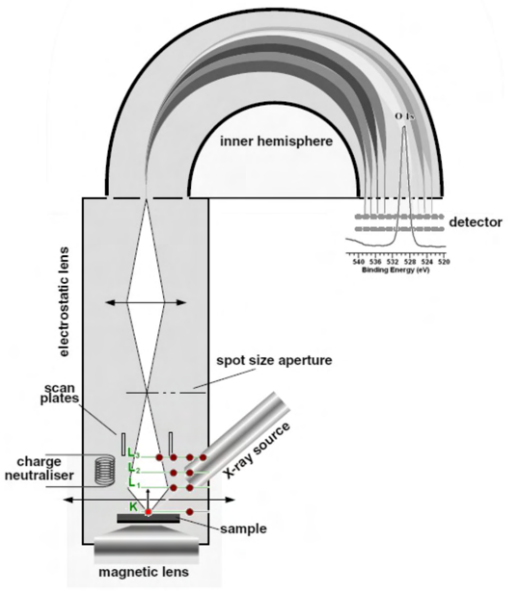

Figure 3.5: Schematic representation of X-ray Photoelectron Spectroscopy set-up [23].

X-ray Photoelectron Spectroscopy (XPS) is a technique used for material characterization in material sciences. In solid-state battery research, this can be the characterization of lithium metal anodes, solid electrolytes, and cathode composites. A schematic representation of an XPS set-up is given in figure 3.5 [23]; this system consists of the following elements. A vacuum chamber that allows the electrons emitted from the sample to move freely. Photons of known energy are emitted from an X-ray source, in order to excite electrons from molecular orbitals of the sample. An electrostatic lens gathers the electrons and focuses their trajectory into the energy analyzer. The energy analyzer only allows electrons with a specific kinetic energy to pass through - different chemical species can be distinguished as the kinetic energy is directly related to the binding energy [89]. The final component is an electron detector, recording the number of electrons of a given kinetic energy arriving from the energy analyzer. The data produced is the counts per

second as a function of binding energies - related to the kinetic energy - from atoms at the surface of the sample being characterized.

XPS is a technique sensitive to the photoemission from the top few nanometers of the sample. The emitted photoelectrons are displayed in an energy spectrum; this graphic representation usually displays primary photoelectron peaks and scattered signals. The primary photoelectron peaks represent the sum of the electrons arriving at the electron detector in counts per second; these peaks are located at the specific binding energies of the emitted photoelectron [23]. Signal fitting was performed using Shirley background, from the Case.xps library.

In this work, XPS measurements were taken of the cathode electrodes post-cycling. The samples are handled in the glove box and placed into a vacuum holder before being placed in the XPS apparatus. Measurements are fitted on the S2p, P2p peaks, meaning the focus is placed on Sulfur and Phosphorous compounds, which are the most common degradation products resulting from the electrochemical cycling of the LPSC-based batteries. Compounds suggested to show up in the XPS results are sulfates (SO_x), lithium polysulfides, P_2S_X ($X \geq 5$), lithium phosphide (Li_3P), and lithium sulfide (Li_2S) [4].

3.7. Scanning Electron Microscopy

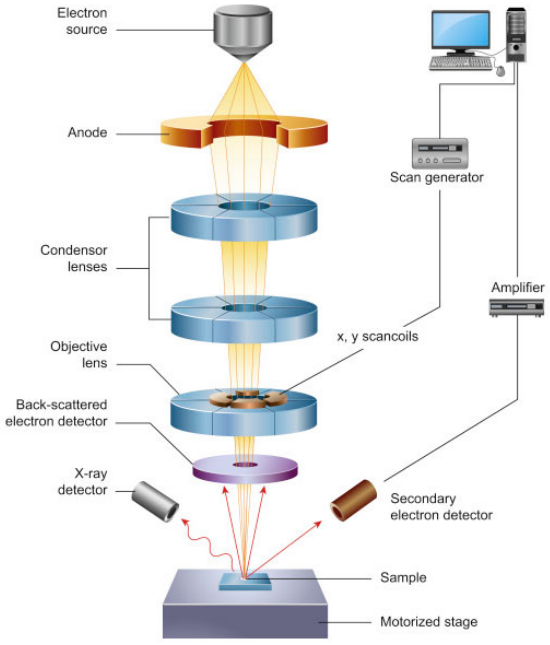

Figure 3.6: Schematic representation of a Scanning Electron Microscope [24].

Scanning Electron Microscopy (SEM) is a method for acquiring high-resolution images and intricate surface details of materials at a nanoscale. The electron microscope ejects a focused electron beam to scan the sample's surface, producing images at significantly higher resolutions than those achievable through optical microscopy [24]. A schematic representation of a scanning electron microscope is depicted in figure 3.6. In a scanning electron microscope, electrons are generated at the top of the column in the electron gun and accelerated through the column. Condenser lenses and apertures work to reduce the beam diameter, with the final objective lens focusing the beam on the sample surface, achieving a diameter ranging from less than 1 nanometer to 20 nanometers. The sample is mounted on a stage in a vacuum chamber, with the column and chamber maintained under vacuum. Signals, including secondary electrons, backscattered electrons, and characteristic X-rays, are generated when the beam strikes the sample and are detected by appropriate detectors.

Secondary electrons are detected with the Secondary Electron Detector (SED), and Backscattered electrons are detected with the Backscattered Electron Detector (BED). While secondary electrons emerge from 0-10nm depth, backscattered electrons emerge from 10-100nm depth, allowing the researcher to look at different surface depths of the sample. Also, the acceleration voltage influences the detection depth: lower voltages give more information from the surface, and higher acceleration voltages allow for electron detection from deeper within the sample. The scan generator, synchronized with an external computer, enables real-time, pixel-by-pixel grayscale image display [24]. The produced images can achieve resolutions ranging from 3 nm to several micrometers. In BED images, the NMC particles appear brighter compared to the LPSC due to the elemental makeup of the materials. NMC particles are made up of heavier elements, resulting in bigger nuclei, deflecting electrons more strongly than lighter elements.

In this study, the JEOL JSM-IT100 was used for samples in an airtight holder, and the JEOL JSM-IT700HR FE-SEM for NMC powder investigations. SEM images are made by extracting the battery components between the steel cell parts and placing them in an airtight sample holder. Single-pallet cathode electrodes were constructed and placed in the airtight holder to generate pre-cycling SEM images of the cathode surface morphology. Both Secondary Electron Detector (SED) and Backscattered Electron Detector (BED) images were taken to look at different surface depths of the sample.

3.8. X-ray Diffraction

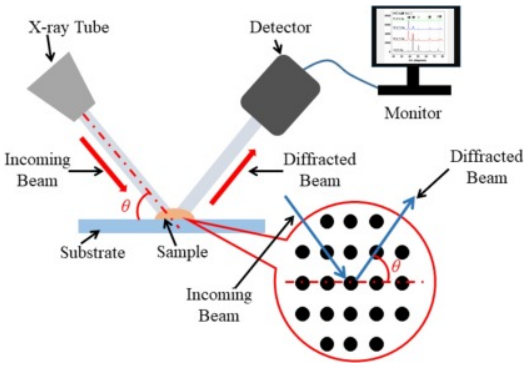

Figure 3.7: Schematic representation of a X-ray Diffractometer [25].

X-ray Diffraction (XRD) was used to characterize the polymeric protective coating on the NMC particles and to study the crystallographic lattice parameters of the NMC particles pre-, and post-cycling. XRD is a method used to identify the compositions, microstructures, and molecular structure of coatings. The typical experimental setup is shown in figure 3.7 [25]. This method is a valuable addition to other techniques used in the degradation analysis of the cathode-electrolyte interface. Fitting XRD patterns can also allow the detection of secondary phases in the sample, and the calculation of lattice parameters can reveal information about experienced stresses during cycling [90].

XRD relies on the constructive interference of X-rays and the crystalline battery components. X-rays, which are short-wavelength electromagnetic radiation, are produced when sufficiently energetic charged particles are slowed down in the X-ray Tube [91]. These X-rays are focused and aimed at the sample as the incoming beam. The interaction between the incident X-rays and the sample generates a diffracted beam, which is intercepted by a detector. The incoming beam, and thus the diffracted beam, are produced at various angles, resulting in a diffraction pattern revealing information about the sample.

In this study, Cu radiation was used, with the absolute scan function and the XCelerator detector. Diffraction patterns were collected in a 2θ angular range from 10° to 90°, with a step size of 0.008°. Post-cycled samples, as well as coated NMC particle powders, were characterized by XRD.

4

Results

The upcoming chapter describes the results of experiments conducted on various assembled sulfide-based solid-state batteries (SSBs). These experiments aimed to investigate the electrochemical cycling performance and degradation mechanisms - caused by electrochemical instability or mechanical deformation - during the electrochemical cycling of SSBs with conductive additives or polymeric protective coatings. Firstly, the impact of the addition of Carbon Nanofibers (CNF) to the cathode composite on the cycling performance and the electrochemical and mechanical stability of the SSBs is explored. The cycling performance of single-crystal and polycrystalline Ni-rich cathode active materials is also tested. This is followed by examining the effects of polymerized ionic liquids (PIL), PDDA-TFSI, as polymeric protective coatings for polycrystalline NMC811 particles. Finally, the influence of PDDA-TFSI and lithiated PDDA-TFSI as a protective coating on single-crystal NMC Ni82 is investigated. Each of the three subsections on CNFs, PIL on polycrystalline, and PIL on single-crystal NMC, the presentation of results includes cycling performance, Electrochemical Impedance Spectroscopy (EIS), X-ray Photoelectron Spectroscopy (XPS), X-ray Diffraction (XRD), and Scanning Electron Microscopy (SEM) images.

4.1. Cathode Composite Optimization: Effect of Carbon Nanofibers and Cathode Particle Size

This subsection describes the effect of CNF on the cycling performance and the degradation of SSBs with argyrodite, as well as the differences between the performance of a polycrystalline, and a single-crystal, crystal structure for the NMC particles. The cathode composites were prepared as described in section 3.1, and cell assembly was performed as described in section 3.3. In the following sub-sections, the prepared samples are referred to as **PC-NMC**, **SC-NMC** and **PC-NMC w/ 3-CNF**. The PC-NMC samples were prepared with a cathode composite consisting of 70wt% of polycrystalline NMC811 particles and 30wt% argyrodite (Li_6PS_5Cl). SC-NMC was prepared with 70wt% of single-crystal NMC Ni82, and 30wt% argyrodite. The samples named PC-NMC 3-CNF were prepared with a cathode composite consisting of 70wt% polycrystalline NMC811, 27wt% LPSC, and 3wt% CNF.

All samples were assembled twice. Replication of results is of utmost importance; this ensures that the results are consistent and not due to chance or specific conditions presented in the initial experiment. The assembly of two of the same SSBs also helped identify outlying performances of specific cell configurations and ultimately helped with a consistent cell assembly protocol.

4.1.1. Cathode Powder Analysis using Secondary Electron Microscopy

SEM images of polycrystalline NMC811 and the single-crystal nickel-rich NMC were taken, shown in figure 4.1. These images were taken with the Secondary Electron Detector setting at different magnifications, at a similar acceleration voltage of 1kV. The images were taken to assess their differences in crystal

structure and surface morphology; the following sections, where polymer interlayers are introduced, also compare these pristine NMC particles with the coated cathode active material.

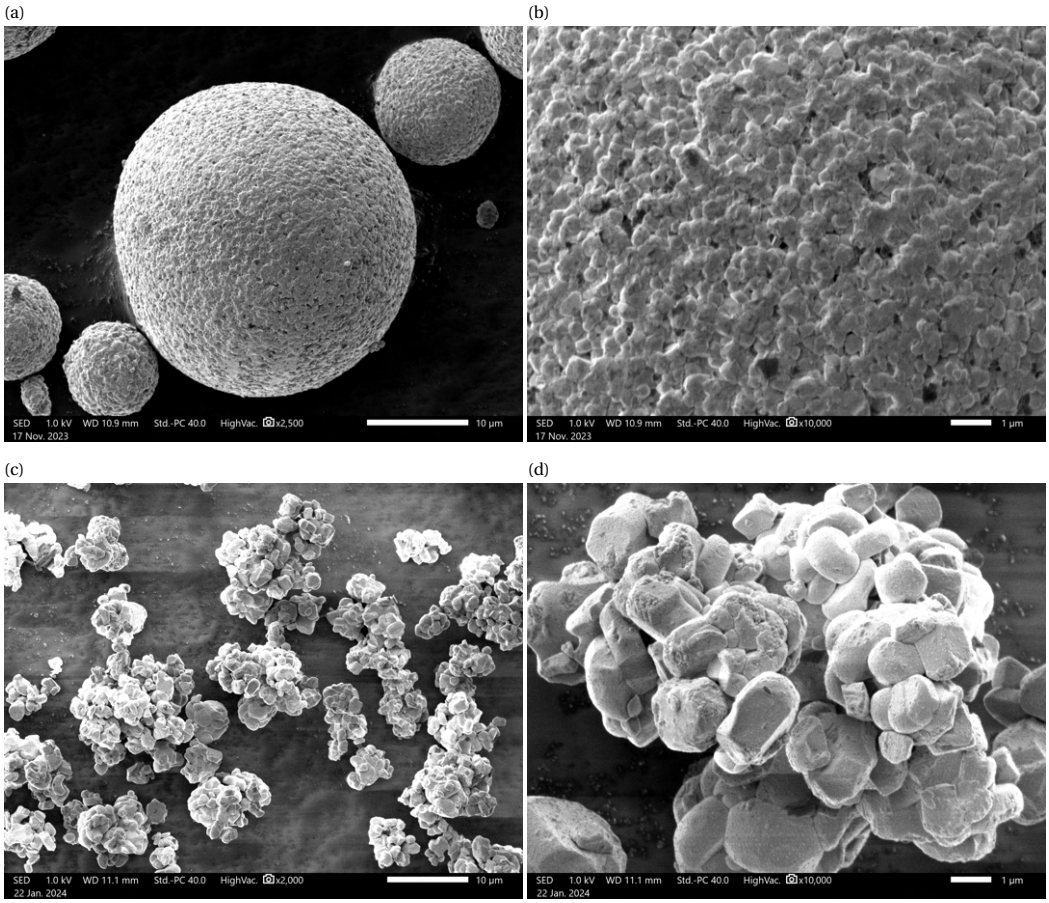

Figure 4.1: SEM images of a) polycrystalline NMC811 particles taken at a 2,500x magnification, b) the surface of a polycrystalline NMC811 particle at 10,000x, c) single-crystal NMC Ni82 at 2,000x, and d) single-crystal NMC at 10,000x. All images were taken with SED, and a 1kV acceleration Voltage.

The polycrystalline NMC811, depicted in figure 4.1a), and b), shows a spherical shape from aggregations of primary particles. These spherical aggregations have an average particle size (D50) of 10 to 13 μm. This specific image displays particles slightly larger and smaller than the provided D50 range, which is to be expected. The NMC particles in the subfigures 4.1c), and d), have a single-crystal structure, solely consisting of primary crystal particles. These crystals are smaller and have an average grain size (D50) of 3 to 5 μm. These images can later be referred back to for comparison with polymer-coated versions of the identical nickel-rich NMC particles or post-cycled cathode electrodes using these active cathode materials.

4.1.2. Electrochemical Cycling Performance

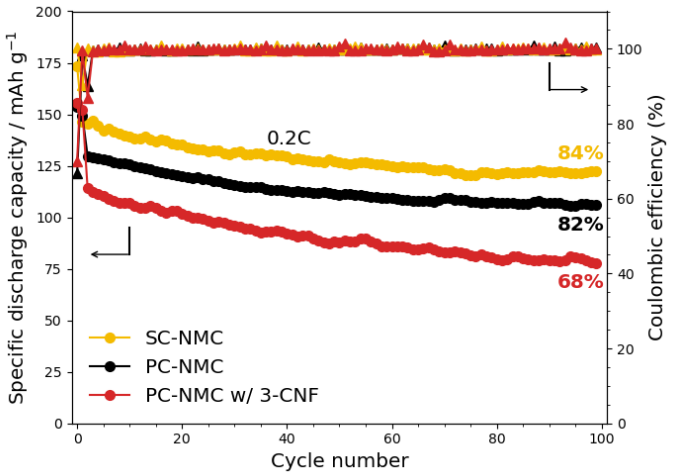

Figure 4.2: Long-term cycling discharge capacity of lithium-indium alloy anode, LPSCl, and SC-NMC, PC-NMC and PC-NMC w/ 3-CNF, at 0.05C for the first two cycles, 0.2C for following cycles, and at room temperature. Cathode active materials ≈ 10 mg cm^{-2}.

To examine the impact of the carbon nanofibers on battery performance, galvanostatic cycling is conducted on **PC-NMC**, and **PC-NMC w/ 3-CNF** at 0.05C for the first two cycles and 0.2C for the remainder of the cycles, totaling 100 charge-discharge cycles. To study the difference between a single-crystal and a polycrystalline crystal structure, similar galvanostatic cycling is performed on sample **SC-NMC** (Figure 4.2). The graph shows the specific discharge capacity in mAh/g versus cycle number and the coulombic efficiency, expressed as the ratio (%) of the charge extracted during discharge to the charge applied during charging.

PC-NMC showed an initial capacity of 129.7 mAh/g at the 3^{rd} cycle, versus the much worse 114.1 mAh/g of PC-NMC w/ 3-CNF. Additionally, the capacity retention after 100 cycles of the PC-NMC was significantly better than that of the 3-CNF. Capacity retention shows the long-term battery stability [16], and is determined as the discharge capacity at cycle x, relative to the initial discharge capacity. In this case, the first two cycles are at a 0.05C rate, and the initial capacity is determined to be at the 3^{rd} cycle, where the C-rate is 0.2C. Therefore, the capacity retention in this study is the capacity of cycle 100 relative to cycle 3. The capacity retention for Pristine NMC is significantly higher than that of 3-CNF, with 82% compared to 68%, respectively. Notably, a considerably higher voltage decay was seen during long-term cycling for the sample with carbon nanofibers, shown in figure 4.3. Specifically, the voltage decay after the 50th cycle is higher for the sample with carbon nanofibers, whereas this is less rapid for PC-NMC.

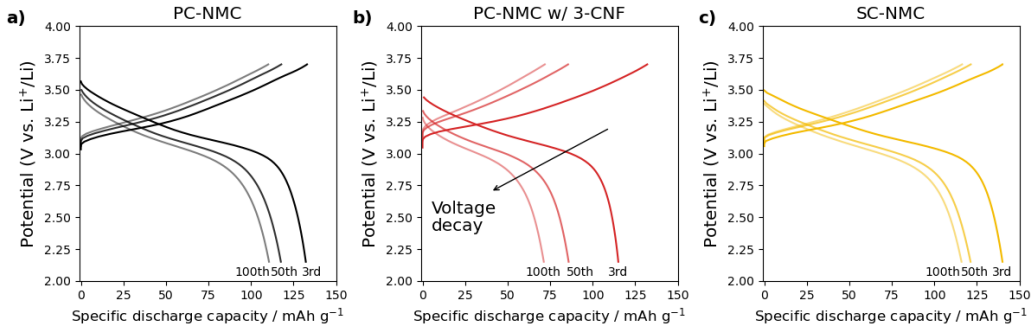

Figure 4.3: Charge-discharge voltage profile for a) PC-NMC, b) PC-NMC with 3wt% Carbon Nanofibers, and c) SC-NMC, at 0.2C for the 3^{rd}, 50^{th}, and the 100^{th} cycle. Cathode active materials ≈ 10 mg cm^{-2}.

The 3rd cycle discharge capacity of the **SC-NMC** was 144.0 mAh/g, roughly 11% better than the discharge capacity at the same cycle number for PC-NMC. The discharge capacity after 100 cycles for SC-NMC was 121.1 mAh/g, resulting in a capacity retention for SC-NMC of 84%, slightly better than the 82% of the sample with polycrystalline NMC. For SC-NMC and PC-NMC, we see that the voltage decay between the 3rd and 50th cycles is much greater than that of the following 50 cycles, indicating a decreasing deterioration rate. Although the initial capacities vary among PC-NMC and SC-NMC, the capacity retention rates are approximately equal.

4.1.3. Resistance Evolution Monitoring with Electrochemical Impedance Spectroscopy

Several reasons can cause the difference in initial capacity and the deterioration of discharge capacity with the introduction of carbon nanofibers; similar or other reasons can explain the improved initial capacity for the sample with single-crystal NMC. Electrical impedance spectroscopy (EIS) was used pre- and post-cycling to study the evolution of impedance, referring to the changes in the interface resistances during cycling. Increasing impedance can lead to reduced performance and efficiency over time [84].

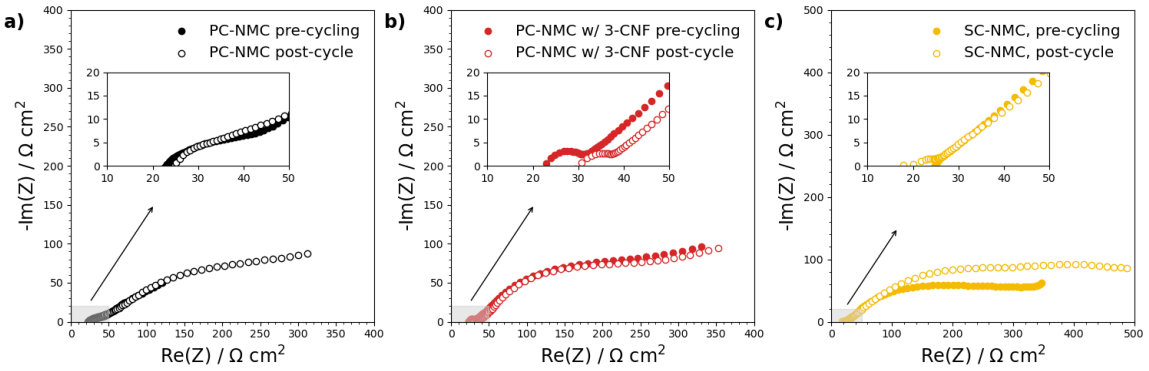

Figure 4.4: Nyquist plot for a) PC-NMC, b) PC-NMC with 3wt% CNF, and c) SC-NMC, pre- and post-cycling. Frequency ranges between 10MHz and 1Hz. The frequency range for the SC-NMC is 10MHz to 0.1Hz.

Figure 4.4 shows the Nyquist plots of the SSBs pre-, and post-cycling. Initially, the pre-cycling EIS measurements were taken at the open-circuit potential of the full-cell right after assembly; for that reason, the pre-cycling EIS measurements of PC-NMC and PC-NMC w/ 3-CNF were taken at an Open Circuit Potential (OCP) at 1.391V and 1.324V, respectively. The pre-cycling EIS measurements of SC-NMC were taken after being charged to a potential of 2.987V. Post-cycling EIS measurements were taken at an OCP of 2.989V, 2.983V, and 3.006V, for PC-NMC, PC-NMC with 3-CNF, and SC-NMC, respectively. This makes a direct comparison of all samples difficult, as differences might result from slight variations in the cathode state of charge, which can influence the charge transfer resistance. Moreover, the frequency range for the SC-NMC has been slightly broader with a lower frequency of 0.1Hz. However, an impedance comparison between PC-NMC with and without CNF, pre- and post-cycling can still be performed.

Another difficulty with the approach of EIS measurements is fitting an electrical equivalent circuit to represent the system. Each circuit element should correspond to a specific physical characteristic - such as the bulk resistance of the solid-electrolyte. However, a prior understanding of the impedance associated with each component is necessary to select the appropriate circuit elements. Therefore, a Distribution of Relaxation Times (DRT) analysis is performed, which can be considered a method to help fit an equivalent circuit to the impedance data, and give accurate approximation of the interface resistances [85].

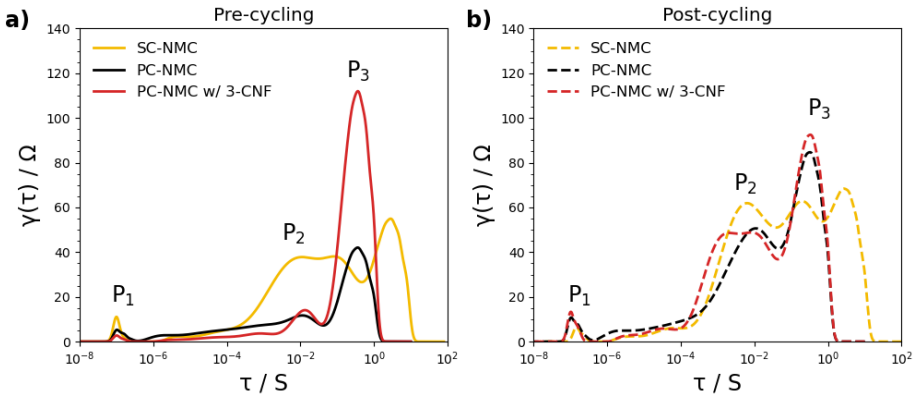

Figure 4.5: DRT plots a) pre-cycling, and b) post-cycling, for PC-NMC, PC-NMC with 3wt% CNF, and SC-NMC.

The performed DRT analysis (figure 4.5) revealed a system with three distinct peaks, denoted as $\mathbf{P}_1$, $\mathbf{P}_2$, and $\mathbf{P}_3$. Where figure 4.5a) shows the DRT plots pre-cycling, and figure 4.5b) post-cycling. Here, the different frequency range of the SC-NMC sample is evident and therefore not comparable to the polycrystalline NMC samples. The peaks can be assigned to components of an equivalent circuit element with their resistances. The DRT analysis, just like the Nyquist plot, consists of a high-frequency region, a midfrequency region, and a low-frequency region, corresponding to $\mathbf{P}_1$, $\mathbf{P}_2$, and $\mathbf{P}_3$, respectively. The peaks around 10^{-7} s can be assigned to the bulk resistance of solid-electrolyte ($\mathbf{P}_1$), sensitive to high frequencies. The peaks around 10^{-2} s can be speculated to be the interfacial resistance at the SE-separator/ electrode interface ($\mathbf{P}_2$); this is the midfrequency region. The low-frequency region around 1 s can be assigned to the charge transfer resistance of the NMC and the argyrodite ($\mathbf{P}_3$) [47]. The DRT analysis served as a technique to find an equivalent circuit that could be fitted to the original EIS measurement. Given the three peaks, the inductance of the electrical wires, and the Warburg impedance, the following equivalent circuit is constructed (figure 4.6). A description of the physical meaning of each DRT peak is given in table 4.1.

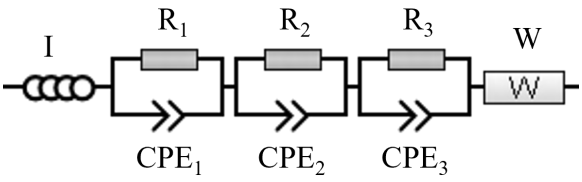

Figure 4.6: Schematic representation of the proposed equivalent circuit.

Table 4.1: overview of resistance annotations and their assigned element in the proposed equivalent circuit.

Peak	Description	Description in Eq. Circuit
-	Inductance	I
P_1	Bulk resistance of solid-electrolyte	R_1/CPE_1
P_2	Solid-Electrolyte Separator/Electrode interface resistance	R_2/CPE_2
P_3	Charge-transfer resistance of NMC/LPSC interface	R_3/CPE_3
-	Warburg Impedance, diffusion limitations	W

The quantification of the interface resistances $\mathbf{R}_1$, $\mathbf{R}_2$, and $\mathbf{R}_3$, pre- and post-cycling, can be constructed by fitting the proposed equivalent circuit to the original EIS measurements. The impedance data is fitted in the Nyquist plot, shown in figure 4.7. The interface resistances were quantified using the RelaxIS software, the EIS data, and the equivalent circuit as input. The values for $\mathbf{R}_1$, $\mathbf{R}_2$, and $\mathbf{R}_3$ can be found

in table 4.2. Pre-cycling the bulk resistance ($\mathbf{R}_1$, and the SE-pellet/electrode interface ($\mathbf{R}_2$) are of the same order of magnitude for both PC-NMC, as for PC-NMC with 3wt% CNF. However, the sample with carbon nanofibers as a conductive additive has the highest resistance values. Moreover, the pre-cycling charge transfer resistance between NMC and the LPSC particles ($\mathbf{R}_3$) is much greater for the sample with conductive additives. One reason for this can be that the carbon nanofibers form an obstruction between the NMC and the LPSC, therefore reducing the Li^+ conduction.

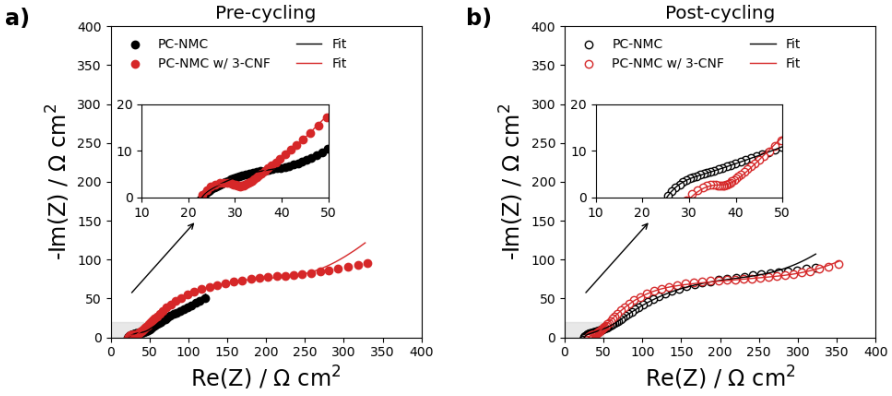

Figure 4.7: Nyquist plot fitted to the proposed equivalent circuit, pre- and post-cycling, for PC-NMC, PC-NMC with 3wt% Carbon Nanofibers.

Table 4.2: Interface resistances pre-, and post-cycling, of R_1, R_2, and R_3, for the samples PC-NMC, and PC-NMC with 3wt% CNF.

Sample	Pre-cycling			Post-cycling		
	$R_1(\Omega)$	$R_2(\Omega)$	$R_3(\Omega)$	$R_1(\Omega)$	$R_2(\Omega)$	$R_3(\Omega)$
PC-NMC	23.29	21.858	37.316	31.076	30.183	198.79
PC-NMC w/ 3-CNF	29.56	32.197	196.28	36.995	38.366	268.01

Post cycling, the interface resistance between the NMC particles and the argyrodite ($\mathbf{R}_3$), is greater for the sample with 3wt% carbon nanofibers compared to the cell with polycrystalline NMC without the addition of Carbon Nanofibers. The increased $\mathbf{R}_3$, caused by the addition of the conductive additive, can be speculated to be the reason for higher overpotentials and a worsened discharge capacity after 100 cycles. The bulk resistance ($\mathbf{R}_1$) and the SE-separator/electrode interface resistance ($\mathbf{R}_{2)}$) also display elevated levels of resistance for the cell with 3wt% CNF. Summarized, EIS measurements indicate that the sample with 3wt% carbon nanofibers has increased interface resistance pre-cycling, as well as post-cycling, which is in line with the cycling performance shown in figure 4.2.

4.1.4. Chemical Stability Analysis with X-ray Photoelectron Spectroscopy

To investigate the decomposition products of the samples, PC-NMC (fig.4.8a - c), PC-NMC with 3wt% CNF (fig.4.8 d - f), and SC-NMC (fig.4.8 g - h), post-cycling XPS is conducted. The S2p spectra has closely spaced spin-orbitals (j=3/2 and j=1/2) [92], and four distinct doublets are observed. These doublets are PS_4^{3-} at a binding energy of ≈160.5 eV (red doublet), P-S-P at ≈162 eV (green doublet), S_x at ≈164eV (blue doublet), and SO_x at a binding energy of roughly 170eV (purple doublet) [93]. Here, "S_x" is a simplification for various compounds, besides elemental sulfur, that can be originating from that binding energy [94]. The S2p peak consists of doublets with a peak split constrained to 1.16eV and a peak intensity ratio of 0.511. The P2p spectra look slightly different for the various samples, and up to five doublets can be identified; PS_4^{3-} at ≈132.5eV (red doublet), P-S-P at ≈134eV (green doublet), oxidized phosphorous, phosphates, at ≈135.5eV (cyan doublet), reduced P^0 and Li_xP at ≈129.5eV and ≈128.5eV (blue doublet).

[95][94] The P2p peaks consist of doublets which are constrained at 0.87eV. The C1s environment can mostly be attributed to the carbon tape used, and the evaporation of the glue for sticking the samples to the XPS-sample holder [96]. However, some differences do arise post-cycling, such as the formation of the reduced species of lithium carbide.

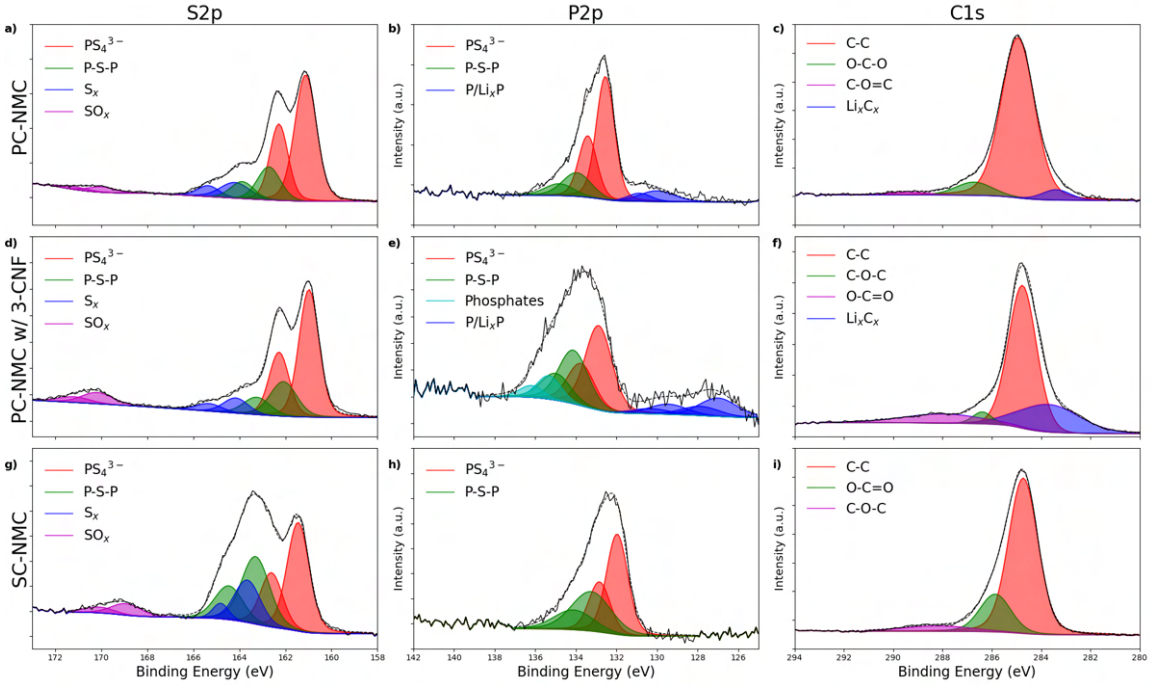

Figure 4.8: Post-cycling - S2p, P2p, and C1s spectra, of a) - c) the polycrystalline NMC811, d) - f) the polycrystalline NMC811 with 3wt% carbon nanofibers, and g) - i) single-crystal NMC, Ni82, samples.

Looking at the S2p spectra of all three samples, the PS_4^{3-} doublets can be assigned to the Li_6PS_5Cl phase [8]. For the PC-NMC cell with CNFs, and the SC-NMC cell, a slight increase in the intensity of oxidized species P-S-P (P_2S_x), and S_x, can be observed [12]. The SO_x peak appears with a slightly higher intensity; this may be an oxidation decomposition product and can be caused by oxygen contamination during transportation of the samples for XPS measurements [97]. However, the oxygen-rich nature of the active material of the cathode can be a source for the formation of SO_x as well [4]. The observation of the S2p spectra can be confirmed by comparing them with the P2p spectra. The increased intensity of the P-S-P species is confirmed for the cells with CNFs. Another environment that can be observed is that of oxidized phosphates. Next, reduced species, such as P/Li_xP, are detected in the same spectra as the observed phosphorous. The presence of species caused by reduction and oxidation might suggest oxygen contamination is a possibility. [94] In the C1s spectra, an increased amount of Lithium Carbide can be observed, suggesting the consumption of Li-ions at the cathode. This is not observed in the sample with single-crystal NMC.

With the use of XPS measurements on the sample with CNFs as conductive additive; it appears that the capacity fade strongly correlates to the increased formation of sulfates/sulfites (SOx), polysulfides (P2Sx), phosphates (POx), and lithium phosphate phases (P/Li_xP) is apparent.

4.1.5. Morphology Evolution Analysis with Scanning Electron Microscopy

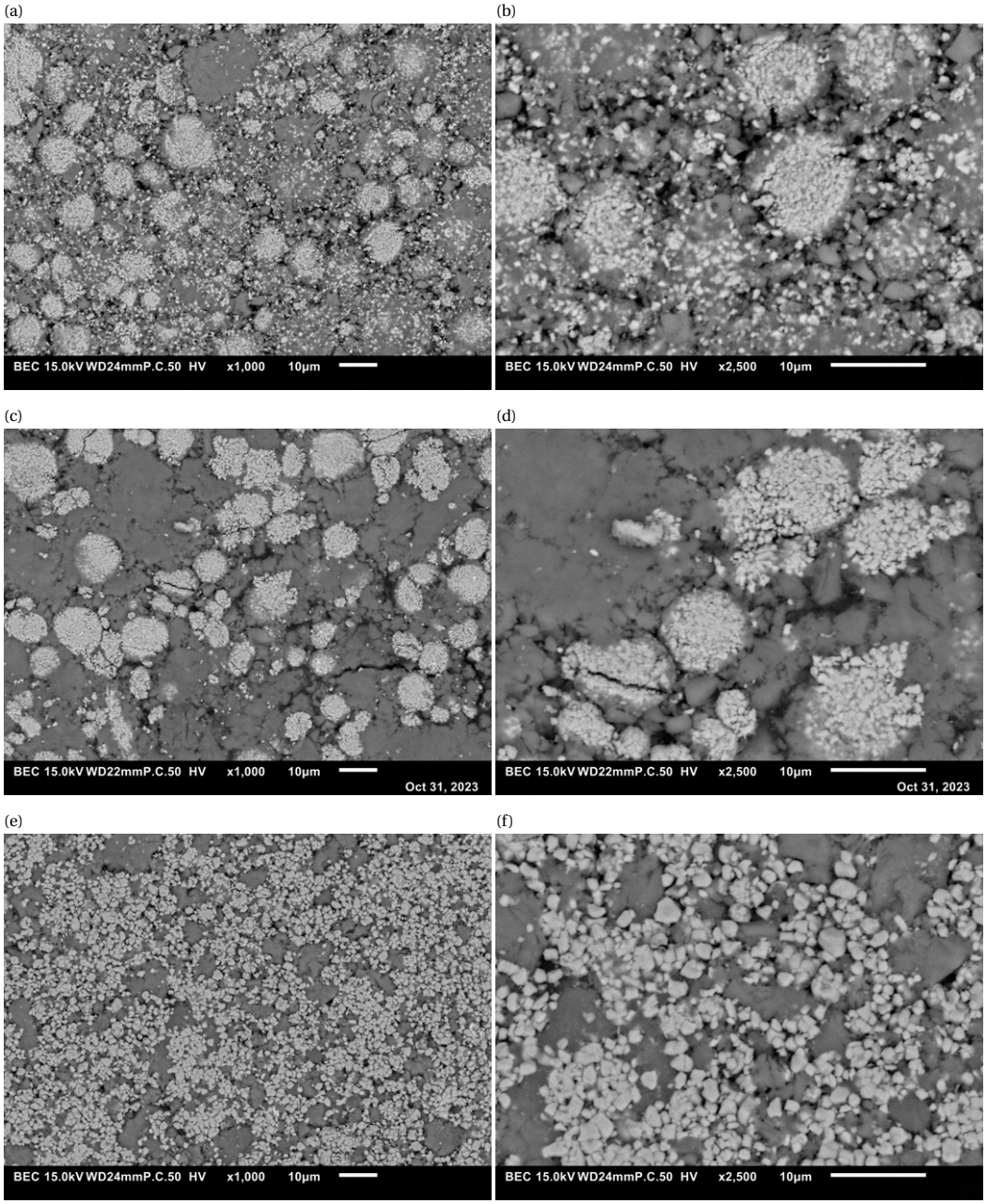

Figure 4.9: Post-cycling SEM images of a) - b) PC-NMC, c) - d) PC-NMC with 3wt% Carbon Nanofibers, and e) - f) SC-NMC; magnifications are 1,000x and 2,500x. All images were taken with BED and a 15kV acceleration voltage.

SEM is used to investigate the mechanical deformation of the cathode composite after 100 cycles at 0.2C, as shown in figure 4.9. All images are of detected backscatter electrons, therefore looking slightly deeper into the surface morphology of the cathode composites than using the secondary electron detector [24]. Here, the NMC particles appear lighter, due to their consistency of heavier elements, resulting in a bigger nuclei and deflecting more electrons. Following the same logic, the lighter elements of the LPSC particles deflect fewer electrons, thus appearing darker in the shown SEM images.

The PC-NMC cell, fig. 4.9a) and b) show some fracture lines along the edges of the NMC particles; it also seems that there is some contact loss between the NMC and the LPSC. Another notable feature of the PC-NMC cell is the presence of many more minor, bright particles, which could be caused by the breakup of primary NMC particles during pelletization. The SEM images of the PC-NMC with 3-CNF, fig. 4.9c) and d) show more particle cracking and some contact loss between the NMC and the LPSC. The cracked NMC particles lose contact with the solid-electrolyte, which may be one of the reasons for the poor discharge capacity after 100 cycles of cell with CNF. Looking at the SC-NMC cell, fig. 4.9e) and f), no particle cracking and some slight contact loss can be detected.

The distribution difference between the material of the SC-NMC cell versus that of the PC-NMC cell is more striking. Significantly more contact between the NMC particles is visible in the SC-NMC sample. Returning to the study of Minnmann et al. [6], the material distribution where more NMC particles make contact could positively influence the percolation pathways, specifically for electronic conduction. This may be one of the reasons for the greater initial capacity of the SC-NMC cell compared to the initial capacity of the PC-NMC.

* * *

4.2. Polymeric Interlayers for Polycrystalline NMC811

This subsection describes the effect of polymeric interlayers on the surface of polycrystalline NMC811, on the cycling performance and the degradation of SSBs with argyrodite. The polymeric interlayers were applied to the polycrystalline NMC811 as described in section 3.2. The preparation of the cathode composite and the cell assembly are explained in section 3.1 and 3.3, respectively. In the following sub-sections, the prepared samples are referred to as **PC-NMC**, **PC-NMC w/ 1-PDDA-TFSI**, **PC-NMC w/ 3-PDDA-TFSI**, and **PC-NMC w/ 3-PDDA-TFSI Spray-Dried**. The PC-NMC samples were prepared with a cathode composite consisting of 70wt% of polycrystalline NMC811 particles and 30wt% argyrodite (Li_6PS_5Cl). The cells PC-NMC with 1-PDDA-TFSI, and PC-NMC with 3-PDDA-TFSI have the same 70:30 wt% ratio as the PC-NMC sample, but the NMC particles used have been coated with 1wt%, and 3wt%, PDDA- TFSI, respectively, using the microencapsulation method. The sample specified with spray-dried refers to the sample where the NMC particles have been coated using the spray-drying process. This chapter starts with the analysis of the applied polymeric protective coatings, followed by the study of the cycling performance of the cells, and the investigation of the degradation mechanisms.

4.2.1. Surface Analysis of Polycrystalline NMC with Scanning Electron Microscopy

SEM images of coated polycrystalline NMC811 particles were taken, shown in figure 4.10. These images were taken using the Secondary Electron Detector setting at a 1kV acceleration voltage. The purpose of these pictures was to make a first assessment of the application of the PDDA-TFSI coatings. Here, 4.10a) to c) are the images of the polycrystalline NMC811, with 1wt% of PDDA-TFSI, and d) to f) of PC-NMC with 3wt% PDDA-TFSI. These coatings were applied using the microencapsulation application method. The SEM images displayed in figure 4.10g) to i), were taken of the spray-dried coated polycrystalline NMC particles. Magnifications range from 1,000x to 15,000x, to ensure the ability to assess the homogeneity of the coating and the coating morphology on the particle's surface.

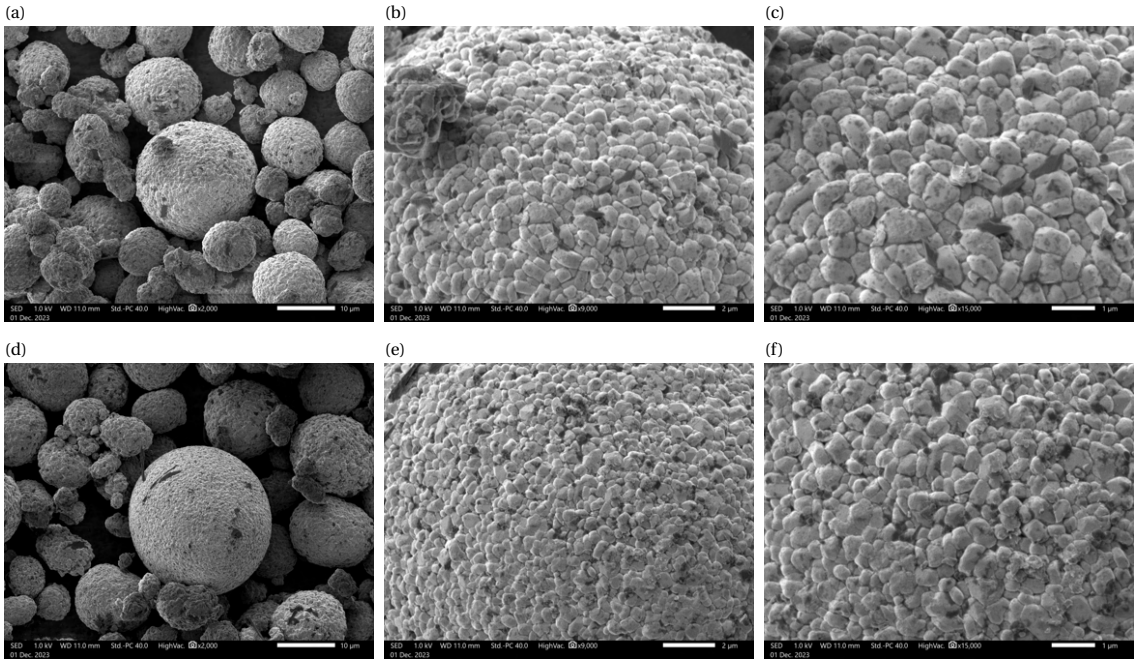

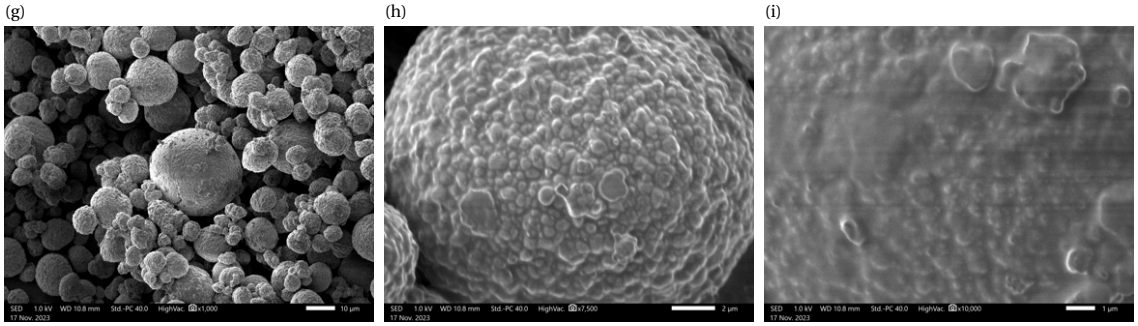

Figure 4.10: SEM images of poly crystalline NMC811 with; a) - c), 1wt% PDDA-TFSI microencapsulated coating; d) - f), 3wt% PDDA-TFSI microencapsulated coating, magnifications are 2,000x, 9,000x, and 15,000x; g) - i), 3wt% PDDA-TFSI spray-dried coating, magnifications are 1,000x, 7,000x and 10,000x. All images were taken with SED, and a 1kV acceleration Voltage.

The particles coated with the microencapsulation method display the formation of PDDA-TFSI particles on the surface of the NMC particles. The images can be compared to the uncoated polycrystalline NMC particles displayed in figure 4.1. The PDDA-TFSI particles appear darker, relative to the lighter-colored NMC particles. At the smallest magnification of 2.000x, figures 4.10a) and 4.10c), a broad range of size differences of the precipitated PDDA-TFSI particles can be observed. At greater magnifications, figures 4.10d) and 4.10f), the PDDA-TFSI are seen on the surface of grainy morphology of the polycrystalline NMC. However, besides the dark more obvious PDDA-TFSI particles, smaller dark spots can be spotted on the surface of individual crystals of the polycrystalline structure. This might indicate that besides the larger precipitated PDDA-TFSI particles, there is also the presence of a thinly coated PDDA-TFSI film.

For the images taken of the spray-dried NMC particles, PDDA-TFSI particles were not observed. At the smallest magnification, figure 4.10g), the applied PDDA-TFSI coating looks more uniform as the darker spots observed in the other pictures can not be detected. Despite the coating looking more uniform, observing the SSEM images with greater magnifications, figures 4.10h) and i), the coating completely changed the morphology of the polycrystalline NMC particle. Where the granular morphology of the polycrystalline structure could still be observed in the microencapsulated particles, the surface morphology is smoother for the NMC particles that were spray-dried.

4.2.2. Electrochemical Cycling Performance

To study the performance of sulfide-based solid-state batteries with polymeric protective coatings, electrochemical cycling is performed on polycrystalline NMC samples; **PC-NMC**, **PC-NMC w/ 1-PDDA-TFSI**, **PC-NMC w/ 3-PDDA-TFSI**, and **PC-NMC w/ 3-PDDA-TFSI Spray-Dried**. The cycling protocol has been left unchanged, with a C-rate of 0.05C for the first two cycles, after which the cells are cycled at 0.2C for the remainder of the 100 cycles. The cycling performance is shown in figure 4.11, where the specific discharge capacity (mAh/g) is represented on the left y-axis, the coulombic efficiency (%) on the right y-axis, and the cycle numbers are displayed on the x-axis. The cell with a spray-dried polymeric protective coating showed an initial capacity far below the uncoated cells, and it was decided to stop the 100 cycles prematurely. For this reason, the cycling performance of this cell is not displayed in figure 4.11, but can be found in the appendix B, figure B.1. The lower initial capacity was later assigned to silicon contamination during the coating process; XPS measurements of the Si2p spectra of the spray-dried coated NMC powder are shown in figure B.2.

The cycling performance of PC-NMC has been discussed in the previous section but will be briefly repeated for comparison with the polycrystalline NMC811 samples with 1wt% and 3wt% PDDA-TFSI. The PC-NMC cell showed an initial discharge capacity of 129.7 mAh/g at the 3^{rd} discharge cycle, slightly better than the discharge capacity of 123.5 mAh/g for the sample with 3wt% PDDA-TFSI, or the 118.9 mAh/g for the cell with 1wt% PDDA-TFSI. The polymeric protective coating at the surface of the NMC811 particles decreases the initial discharge capacity of the cell. It was expected that the sample with the higher

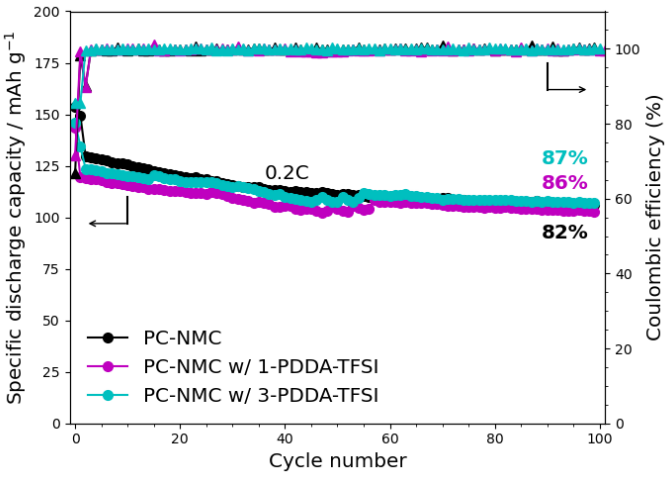

Figure 4.11: Long-term cycling discharge capacity of lithium-indium alloy anode, LPSCl, and Pristine NMC, NMC with a 1wt% or 3wt% PDDA-TFSI protective coating, at 0.05C for the first two cycles and 0.2C for following cycles. NMC active materials = 10 mg cm^{-2}. The 87% capacity retention refers to the first cycle at 0.2C.

weight percentage of the polymer during the coating process would have a thicker coating, therefore encountering a more substantial increase in interface resistance and the lowest initial discharge capacity. However, the cycling performance data presented in figure 4.11 shows that the sample with only 1wt% of PDDA-TFSI has a lower discharge capacity. Other analysis techniques, like electrochemical impedance spectroscopy, might provide arguments for the unexpectedly better initial discharge capacity of the sample with 3wt% PDDA-TFSI compared to the one with 1wt% PDDA-TFSI.

Long-term cycling stability is an insight that can be drawn from capacity retention calculations. As previously explained, the capacity retention was calculated by dividing the discharge capacity at cycle 100 by the discharge capacity at cycle 3. For the sample PC-NMC, the capacity retention at cycle 100 relative to cycle number 3 is 82%; for the sample with 1wt% PDDA-TFSI, the capacity retention is 86%; and for the sample with 3wt% PDDA-TFSI, this is 87%. A slight improvement in capacity retention is observed for the sample with polymeric interlayers.

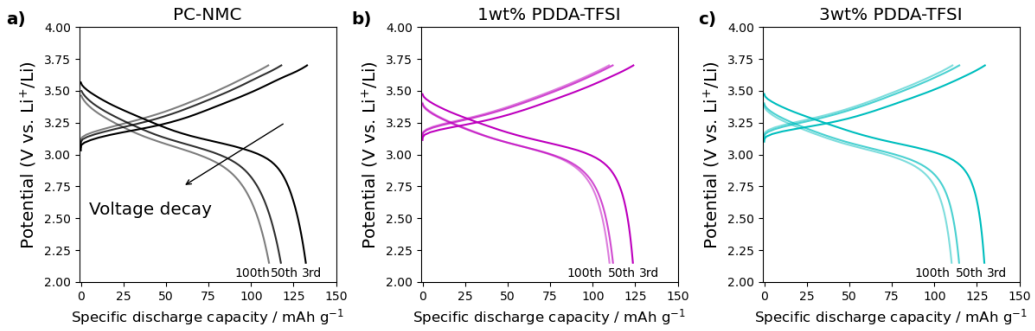

Figure 4.12: a) Charge-discharge voltage profile for pristine NMC NMC with a 1wt% or 3wt% PDDA-TFSI protective coating, at 0.2C for the 3^{rd}, 50^{th}, and the 100^{th} cycle. NMC active materials = 10 mg cm^{-2}.

Figure 4.12 shows the charge and discharge curves for the 3^{rd}, 50^{th}, and 100^{th} cycle of all three of the investigated samples. The charge and discharge curves show that, for all of the samples, the capacity fade of the batteries mainly occurs during the first 50 charge and discharge cycles. The PC-NMC sample displays come with additional capacity deterioration for the 50 cycles that follow. The discharge seems to

approach a stable system with negligible capacity fade for the other two samples, with a 1wt% and a 3wt% PDDA-TFSI polymeric protective coating.

4.2.3. Resistance Evolution Monitoring with Electrochemical Impedance Spectroscopy

The cycling performance of the polycrystalline NMC811 cells with and without a PDDA-TFSI coating showed slight differences in their initial capacity and minorly improved capacity retentions for the cells with a polymeric protective layer. Using electrochemical impedance spectroscopy, pre- and post-cycling, the aim is to understand the performance degradation with the impedance evolution.

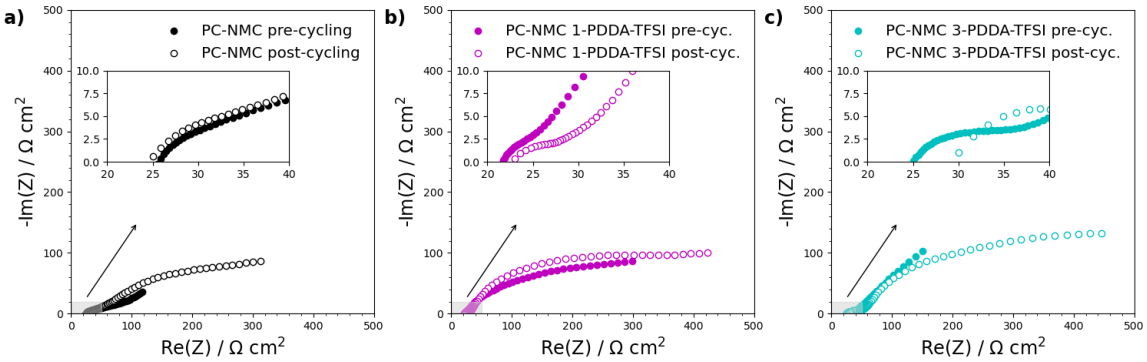

Figure 4.13: a) Nyquist plot for Pristine NMC, b) NMC coated with 1wt% PDDA-TFSI, and c) NMC coated with 3wt% PDDA-TFSI, both pre-cycling and post-100th cycle. Frequency range between 10MHz and 1Hz.

Figure 4.13 shows the Nyquist plots of the samples: PC-NMC, PC-NMC with 1wt% PDDA-TFSI, and 3wt% PDDA-TFSI - pre-cycling, and post-cycling. Again, the EIS measurement protocol was sub-optimal as the pre-cycling EIS measurements of the cell PC-NMC and PC-NMC w/ 3-PDDA-TFSI were taken at the open circuit potential after assembly - roughly 1.3V. All post-cycling measurements were taken at a 3V potential. For this, a direct comparison can be made complex and unreliable; a direct comparison of the samples post-cycling is, however, still possible.

Similar to the EIS measurements in the previous subsection, the difficulty with EIS measurements and extracting relevant data lies with the selection and fitting on an equivalent circuit. DRT analysis is carried out to confirm that the equivalent circuit resembles assembled cells.

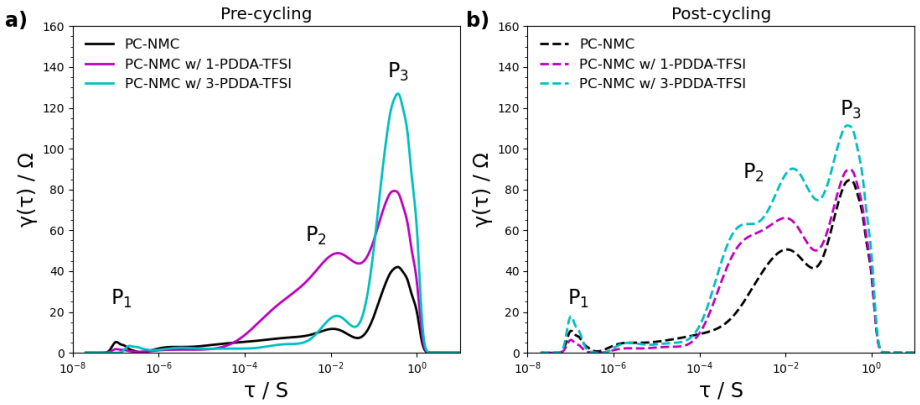

Figure 4.14: DRT plots a) pre-cycling, and b) post-cycling, for PC-NMC, PC-NMC with a 1wt%, and a 3wt% PDDA-TFSI polymeric protective coating.

A distribution of relaxation times is performed and shown in figure 4.14. Pre-cycling (4.14a) a system with three distinct peaks is observed, denoted with $\mathbf{P}_1$, $\mathbf{P}_2$, and $\mathbf{P}_3$. The three peaks are located at different positions on the x-axis, corresponding to different frequency regions. One distinct difference between the $\mathbf{P}_2$ peaks is the slowing angle observed in the sample with 1wt% PDDA-TFSI, which happens to be the only EIS measurement taken at an OCP of 3V pre-cycling. This suggests a direct correlation between the potential at which the EIS measurement was taken and the result DRT fit. Similar peaks can be identified for the DRT curves of the impedance measurements post-cycling. Therefore, the exact equivalent circuit is proposed in figure 4.6, with the corresponding description from table 4.1.

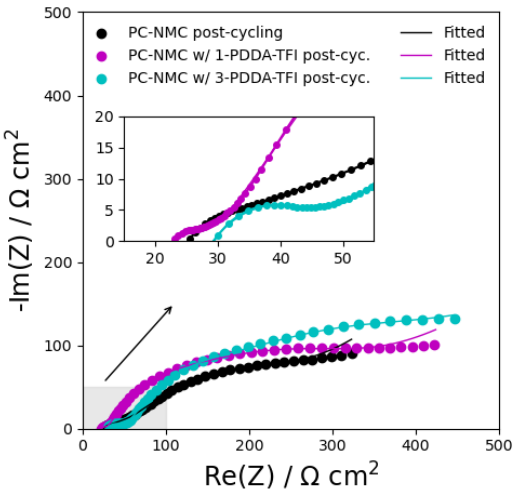

Figure 4.15: Nyquist plot fitted to the proposed equivalent circuit, post-cycling, for PC-NMC, PC-NMC with a 1wt%, and a 3wt% PDDA-TFSI polymeric protective coating.

Table 4.3: Interface resistances R_1, R_2, and R_3, post-cycling, for PC-NMC, PC-NMC with a 1wt%, and a 3wt% PDDA-TFSI polymeric protective coating.

Sample	$R_1(\Omega)$	$R_2(\Omega)$	$R_3(\Omega)$
PC-NMC	31.076	30.183	198.79
PC-NMC w/ 1-PDDA-TFSI	28.012	67.175	186.84
PC-NMC w/ 3-PDDA-TFSI	44.382	75.308	184.48

The interface resistances $\mathbf{R}_1$, $\mathbf{R}_2$, and $\mathbf{R}_3$ can be quantified by fitting the equivalent circuit to the impedance measurements. In figure 4.15, the original data points of the EIS measurements are shown, with the fitted curve as a line. This fit correlates the impedance data with the equivalent circuit, making it possible to quantify the different interface resistances. The interface resistances $\mathbf{R}_1$, $\mathbf{R}_2$, and $\mathbf{R}_3$ can be found in table 4.3. $\mathbf{R}_1$, the resistance related to the bulk resistance of the argyrodite, is approximately the same for the polycrystalline NMC sample without any polymeric interlayers, as for the sample with a 1wt% PDDA-TFSI coating. The sample with the 3wt% PDDA-TFSI coating has an estimated bulk resistance greater than the other samples, indicating a potential issue with the SE pellet. The SE-separator/electrode interface ($\mathbf{R}_2$), is for the coated samples slightly more than double the resistance of the uncoated PC-NMC. As these are the interface resistances post-cycling, the reason that the SE-separator/electrode interface might be elevated can be caused by chemical instability of the interface, contact loss, or potentially the insulating behavior of the polymeric coating. Looking at the interface where the influence of the polymeric coating might be biggest - the particle interface of the polycrystalline NMC and the argyrodite - the interface resistance of the sample without a PDDA-TFSI coating is highest with $\mathbf{R}_3$ equal to roughly 199Ω. The $\mathbf{R}_3$ of the samples with protective coatings is lower than that of the sample without a protective coat-

ing, suggesting that the degradation mechanisms at a particle level - cathode-electrolyte interface (CEI) formation and mechanical deformation - are passivated by the introduction of the PDDA-TFSI coating.

4.2.4. Chemical Stability Analysis with X-ray Photoelectron Spectroscopy

X-ray photoemission spectroscopy (XPS) has been carried out to examine the formation of a cathode-electrolyte interface. The S2p, and P2p spectra of the XPS measurements for samples; PC-NMC, PC-NMC with 1wt% PDDA-TFSI, and 3wt% PDDA-TFSI, are shown in figure 4.16. Here figure 4.16a and b represent sample PC-NMC, figure 4.16c and d, the sample with 1wt% PDDA-TFSI, and figure 4.16e and f, the sample with 3wt% PDDA-TFSI. In the S2p spectra, four distinct doubles are observed for PC-NMC, whereas five doublets are observed for the cells with a protective coating. The red doublets representing the PS_4^{3-}, at a binding energy of ≈160.5 eV. The green doublets corresponding to polysulfides, P_2S_X or P-S-P, at ≈162 eV. Multiple compounds other than elemental sulfur are located in the binding energies of triphosphates. Therefore, the simplified term "S_x" (blue doublets) is used at an intensity of ≈164 [94]. The purple doublets at a binding energy of ≈170eV, can be the oxidation product SO_x [93]. For the cells with a PDDA-TFSI polymeric protective coating, the doubles at a marginally lower binding energy of ≈169.5eV originate from the $TFSI^-$ [92]. The doublets at a binder energy of ≈167.5eV might correspond to reduced TFSI [98]. Notably, a significantly higher fraction originating from the TFSI compound is observed in the sample with 3wt% PDDA-TFSI, relative to sample 1-PDDA-TFSI. The doublets in the P2p spectra originate mainly from similar compounds, PS_4^{3-} at ≈131.5eV, and P-S-P at ≈133.5eV. Some reduced products can be observed at around 130eV originating from P^0, or Li_xP [95][94].

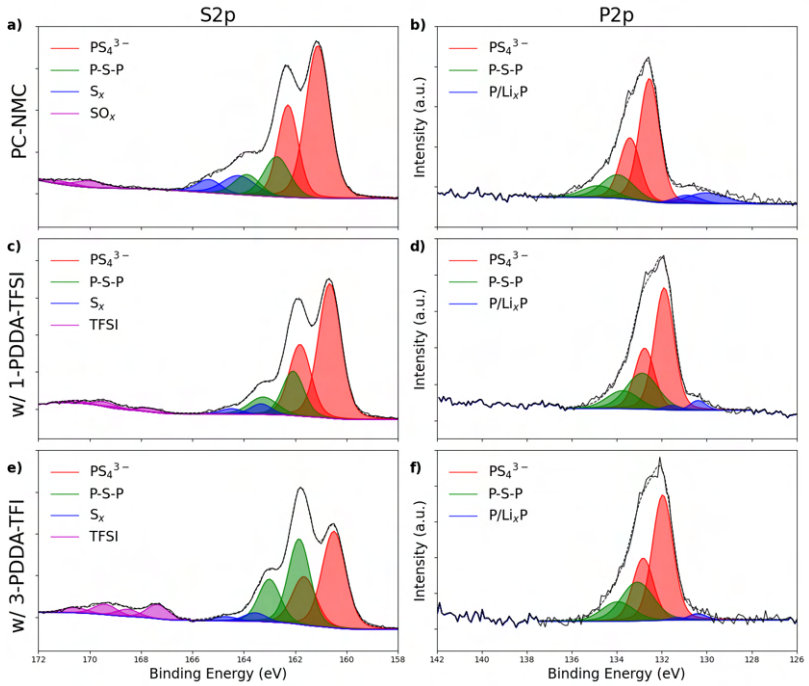

Figure 4.16: Post-cycling XPS measurements - S2p and P2p spectra, of a) - b) the polycrystalline NMC811, c) - d) the polycrystalline NMC811 with a 1wt% PDDA-TFSI polymeric protective coating, and e) - f) with 3wt% PDDA-TFSI.

Logically, the peaks originating from the $TFSI^-$ group in the cells with a greater fraction of PDDA-TFSI, should have a greater peak intensity as well. Figure 4.16c), the polycrystalline NMC with 1wt% PDDA-TFSI some intensity can be observed at the corresponding binding energy of ≈170eV [92]. For the sample with 3-PDDA-TFSI, the intensity at the same binding energy is much greater, indicating a higher content of $TFSI^-$ and a successfully thicker applied PDDA-TFSI coating.

For the solid-electrolyte, Argyrodite (Li_6PS_5CL), the phase PS_4^{3-} is an expected compound. The intensities originating from the polysulfides (green doublets) display a slightly increased intensity for the sample with 1-PDDA-TFSI and a significantly increased intensity for the sample with 3-PDDA-TFSI. The P-S-P compounds, such as $P_2S_7^{4-}$, are compounds that can be formed during the mixing NMC particles with the mortar and pestle [12]. However, the polysulfides are also a compound that increases in intensity during charging of the cell; upon discharging of the cell, the P-S-P intensity is expected to decrease and a signal S^{2-}, and reduced Li_2S is expected [8][94]. Subsequently, with discharging the cell, increased intensity of the reduced species P/Li_xP signal in the P2p spectra is an observation in the study of Wang et al. [94] - this is a compound similarly observed in the figure 4.16b, d, and f. For the uncoated polycrystalline NMC811, a lower intensity of polysulfides is observed, and an increased intensity of the P/Li_xP compound. The sample with a 1wt% PDDA-TFSI coating, a slightly increased polysulfide content, and a slightly decreased P/Li_xP environment is measured. This effect is even more visible for the sample with 3wt% PDDA-TFSI, where the P/Li_xP phases are negligible, and the polysulfides have a significant contribution to the S2p spectra. The ratio of Polysulfide content to P/Li_xP is in line with the observation of the study of Wang et al. [94] and can be related to the state of charge of the battery. As the battery discharges, LPS-like phases decompose into P/Li_xP compounds. Subsequently, during charging cycles, the reduction products are oxidized to LPS-like phases, such as polysulfides and S_x-like species.

4.2.5. Morphology Evolution Analysis with Scanning Electron Microscopy

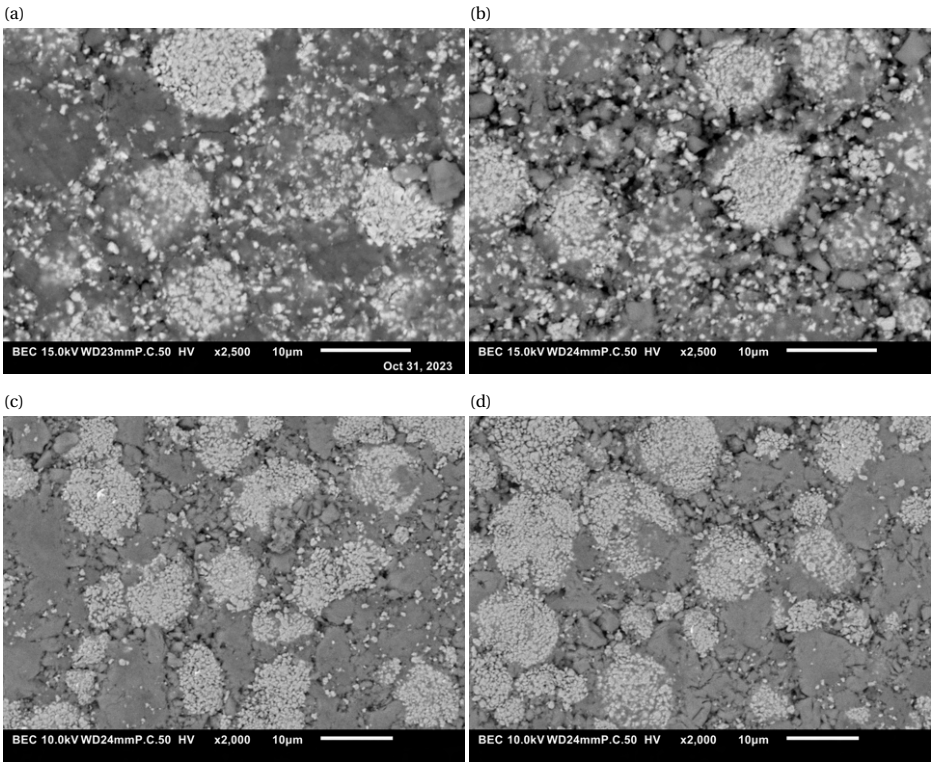

Figure 4.17: SEM images of the cathode electrodes with; a) polycrystalline NMC811 before cycling b) PC-NMC after cycling c) PC-NMC with 1wt% PDDA-TFSI after cycling, and d) PC-NMC with 3wt% PDDA-TFSI after cycling. All images were taken with BED, and a 15kV or 10kV acceleration Voltage, with a magnifications of 2,000x, and 2,500x

SEM is used to study the evolution of the cathode morphology after 100 cycles at 0.2C, shown in figure 4.17. The uncoated, pristine, polycrystalline NMC cell (fig. 4.17a) is before cycling, and 4.17b) after cycling. Figure 4.17c) and d) show the PC-NMC coated with 1-PDDA-TFSI and 3-PDDA-TFSI - both post-cycling. The pristine PC-NMC cathode shows a significant contact loss between the NMC particles

and the argyrodite solid-electrolyte, likely caused by the volume changes of the NMC during lithiation and delitiation [6]. The cells with the 1-PDDA-TFSI and the 3-PDDA-TFSI coating display more retained contact between the CAM and the SE. Additionally, the pristine NMC sample shows some fracture lines, whereas this is limited in the 1-PDDA-TFSI and the 3-PDDA-TFSI samples. This suggests that the improved capacity retention of the cells with a polymeric protective coating can be associated with improved NMC/L_6PS_5Cl contact retention. This implies that the polymer protective coating has acted as a buffer for volume changes due to its elastomeric properties [16].

4.2.6. Microstrain Analysis with X-ray Diffraction

As discussed in the previous section, the polymer protective coating might have acted as a buffer layer for volume expansion, to reduce the contact loss between the NMC particles and the solid-electrolyte. However, there is still the issue of particle cracking which also leads to contact loss in the cathode electrode [6]. XRD measurements were performed on the polycrystalline NMC powder, pristine, and with 1wt% and 3wt% PDDA-TFSI coatings. Post-cycling XRD measurements of the cathode electrode were taken after 100 cycles. Particle cracking can change the lattice parameters of the NMC crystals, which causes peak shift and peak broadening in the XRD patterns [99]. All following XRD patterns have been refined using the Pawley refinement method. The observed, calculated, and the difference between the two is shown in figure B.4 of the supplementary material.

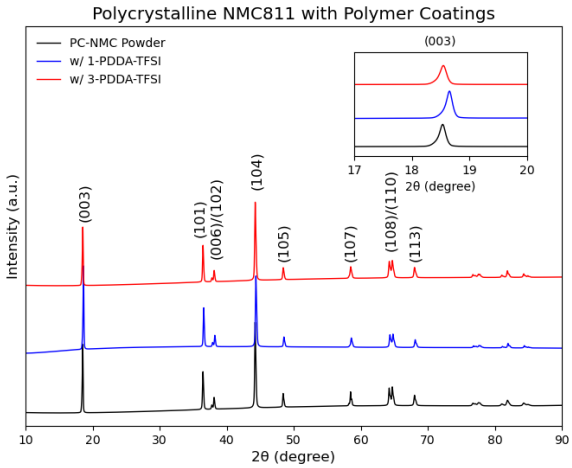

Figure 4.18: XRD patterns of polycrystalline NMC powder, uncoated, and with 1wt% and 3 wt% PDDA-TFSI coatings. Inset axis of (003) peak intensity.

Figure 4.18 shows the XRD pattern of the NMC811 powders, uncoated and coated with PDDA-TFSI. The pattern displays a series of peaks in conformity with the 003, 101, 006, 102, 104, 105, 107, 108, 110, and 113 peaks, which are part of the indexed hexagonal structure of the R-3m spacegroup. Here, the 003 plane can be studied to investigate the evolution of the c parameter, and the 101 and 110 planes to study the lattice parameters a and b [100]. After the application of a polymeric coating, a slight peak shift to the right (higher 2θ) can be observed for the PC-NMC powder with a 1wt% PDDA-TFSI, indicative of a contraction along the c direction. No peak shift is observed for the powder with a 3wt% PDDA-TFSI coating.

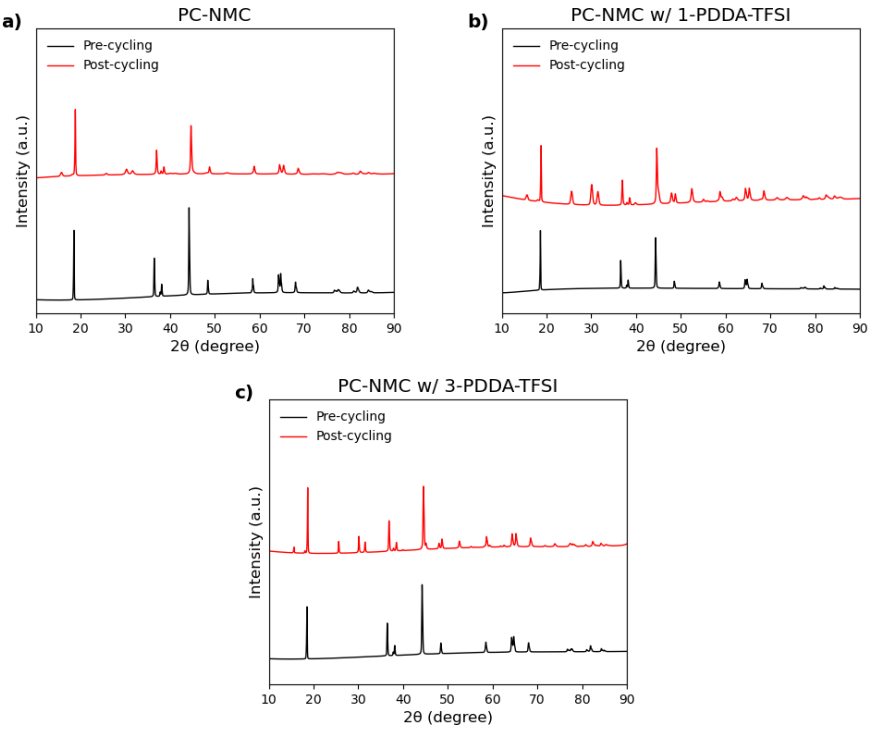

Figure 4.19: Pre-cycling, and post-cycling XRD patterns of a) polycrystalline NMC811, b) polycrystalline NMC with 1wt% PDDA-TFSI, and c) polycrystalline NMC with 3wt% PDDA-TFSI.

The XRD patterns of the polycrystalline NMC powders pre-cycling, and the cathode samples after 100 cycles are shown in figure 4.19. Additional peaks can be observed in the post-cycling cathode samples; these can be assigned to the F-43m spacegroup of the argyrodite solid-electrolyte. Using Pawley refinement, the lattice parameters were convoluted from the XRD patterns, and an estimation of the expansion of the lattice parameters could be made by comparing polycrystalline NMC crystal structures before and after cycling. The lattice parameters are listed in table 4.4; one can rapidly observe that all samples display an expansion along the *c* direction and a contraction of the lattice parameters *a* and *b* - after 100 cycles. All samples showed a similar expansion and contraction of the NMC lattice parameters, suggesting the PDDA-TFSI coating had a negligible effect on the microstrain experienced by the SSBs.

Table 4.4: Pre-, and post-cycling lattice parameters of polycrystalline NMC, pristine, and coated with 1wt% and 3wt% PDDA-TFSI.

Sample	*a, b* (Å)	*c* (Å)
PC-NMC pre-cycling	2.8725	14.2089
PC-NMC post-cycling	2.8609	14.2736
Difference	*-0.0116*	*+0.0647*
PC-NMC w/ 1-PDDA-TFSI pre-cycling	2.8722	14.2049
PC-NMC w/ 1-PDDA-TFSI post-cycling	2.8607	14.2643
Difference	*-0.0115*	*+0.0594*
PC-NMC w/ 3-PDDA-TFSI pre-cycling	2.8727	14.2080
PC-NMC w/ 3-PDDA-TFSI post-cycling	2.8609	14.2732
Difference	*-0.0118*	*+0.0652*

* * *

4.3. Polymeric Interlayers for Single-crystal NMC

This subsection investigates the effect of polymeric interlayers on the surface of single-crystal NMC, Ni82, on the cycling performance, the effect on the chemical and mechanical stability of the SSBs. The polymer used is a polymerized ionic liquid, namely PDDA-TFSI, and as applied as described in section 3.2. In the following subsection, the prepared samples are referred to as **SC-NMC**, **SC-NMC w/ 1-PDDA-TFSI**, and **SC-NMC w/ 2-PDDA-(Li)TFSI**. The SC-NMC cell, which has also been discussed in section 4.1, has been prepared with a cathodecomposite consisting of 70wt% single-crystal NMC, and 30wt% argyrodite. The cells sc-NMC with 1-PDDA-TFSI, and SC-NMC with 2-PDDA-(Li)TFSI have the same 70:30 wt% ratio as the pristine SC-NMC sample, but the NMC particles used have both been coated with 1wt% PDDA-TFSI. However, the one denoted with 2-PDDA-(Li)TFSI has an additional 1wt% of Lithium bis(trifluoromethanesulfonyl)imide (LiTFSI) in its polymeric coating. Again, two cells were made of each variation to reduce the chance of results with significant outlying data. This subsection starts with the analysis of the applied coatings, followed by a section on the electrochemical cycling performance of the cells. After the performance is examined, the evolution of interfacial resistances is tested with EIS measurements, followed by a study on chemical stability using XPS measurements. This subsection ends with the examination of the mechanical stability, a comparison of SEM images of the cathode composites, and an analysis of the microstrain using XRD measurements.

4.3.1. Surface Analysis of Single-crystal NMC with Polymeric Coatings

To examine the polymeric coating on the surface of the single-crystal NMC, SEM, XPS, and TEM, measurements were taken, shown in figures 4.20, 4.21, and 4.22, respectively. SEM images were taken at an acceleration voltage of 1kV. Figure 4.20a) and b) show the images of pristine single-crystal NMC at a 2,000x and 10,000x magnification, figure 4.20c) and d) display single-crystal NMC coated with 1-PDDA-TFSI at magnifications 4,000x and 15,000x, and figure 4.20e) and f) show the images taken of single-crystal NMC coated with 2-PDDA-(Li)TFSI at 2,500x and 10,000x.

(a) (b)

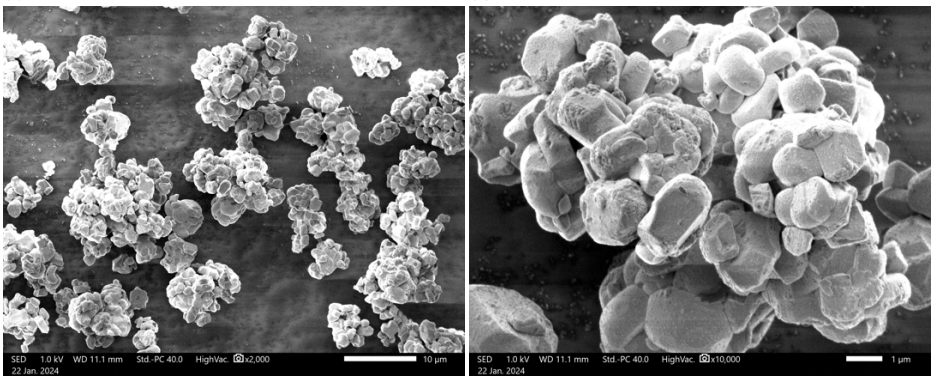

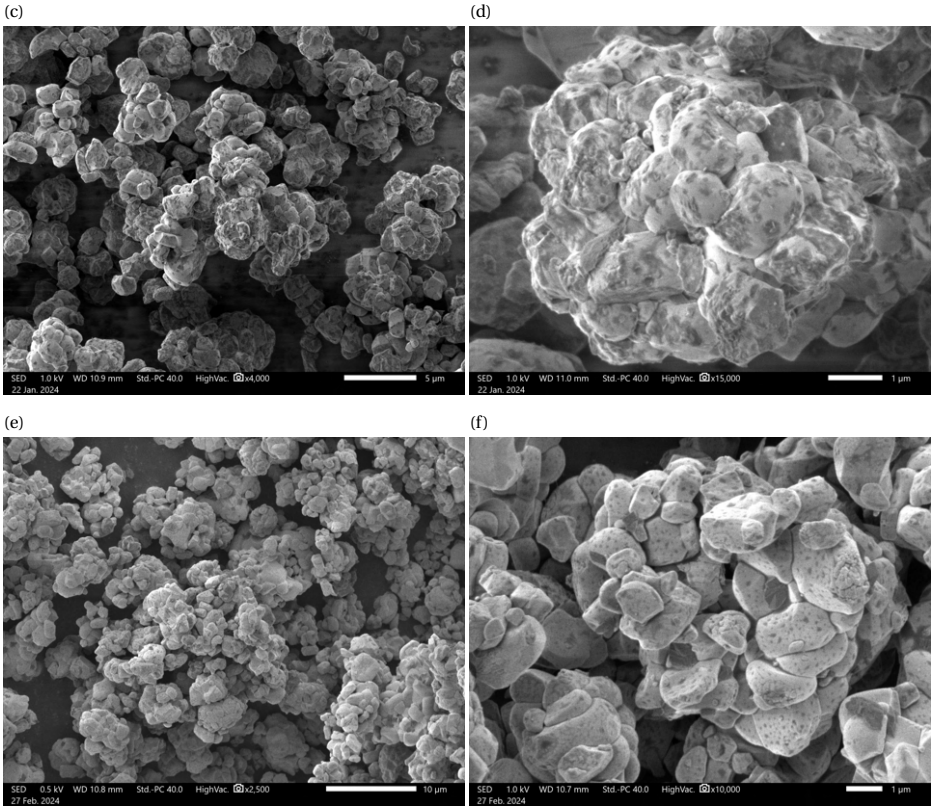

Figure 4.20: SEM images of a) - b) single-crystal NMC Ni82 at 2,000x, and 10,000x, c) - d) single crystal NMC with 1-PDDA-TFSI at 4,000x and 15,000x, and e) - f) single crystal NMC with 2-PDDA-(Li)TFSI. All images were taken with SED, and a 1kV acceleration Voltage.

The pristine, uncoated, single-crystal NMC particles show a smooth surface with limited impurities. The single-crystal NMC particles coated with wt% PDDA-TFSI display darker spots at the surface of the particle, indicating the polymer has collapsed on the NMC surface. Figure 4.20c) shows that not all particles have equally as many dark spots; however, this might be due to the height differences of the particles. Figure 4.20d) displays a single conglomerate of particles, and it can be observed that the polymer might not have precipitated homogeneously. Regardless, the polymer could still cover the complete surface of the particles, as the dark spots are observed throughout. For the images taken with 2-PDDA—(Li)TFSI, similar dark spots can be observed as in the sample with 1-PDDA-TFSI. However, the spots seem to be smaller and spread more evenly over the surface of the particles. This might suggest a more homogenous coverage of the polymeric coating. To ensure that the observed coating actually consists of the elements of the polymerized ionic liquid (PDDA-TFSI), XPS measurements were taken of the pristine single-crystal NMC powder, and the powders with microencapsulation with the PDDA-TFSI, shown in figure 4.21.

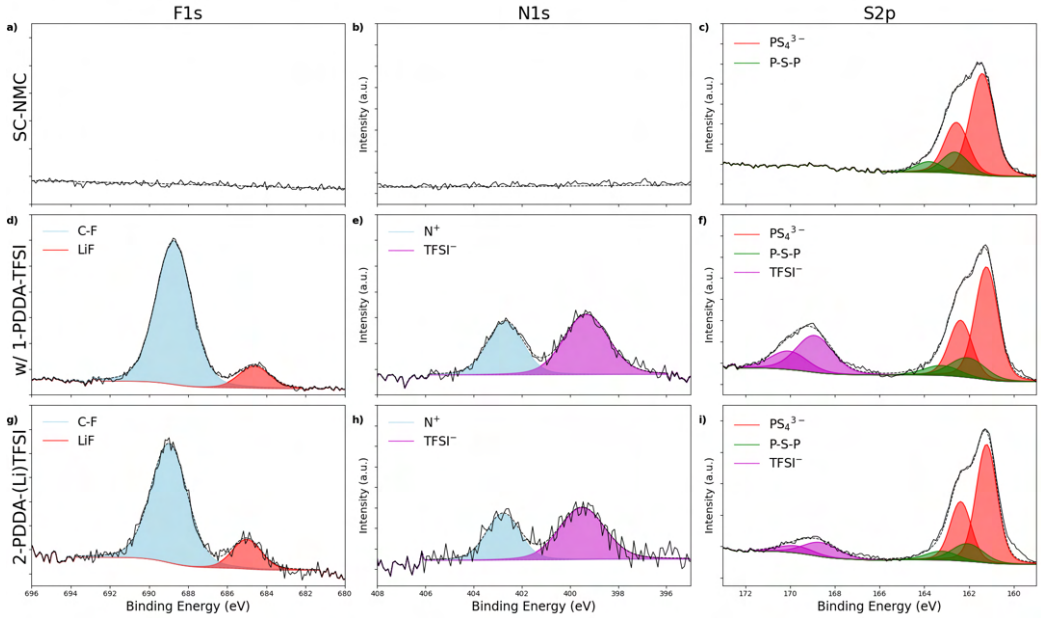

Figure 4.21: XPS measurements of F1s, N1s, and S2p spectra of the cathode composites; a) - c) SC-NMC, d) - f) SC-NMC with 1-PDDA-TFSI, and g) - i) SC-NMC with 2-PDDA-(Li)TFSI.

Figure 4.21 shows the XPS measurements of the F1s, N1s, and S2p spectra of the cathode composites of the samples; SC-NMC (fig. 4.21a - c), SC-NMC w/ 1-PDDA-TFSI (fig. 4.21d -f), and SC-NMC w/ 2-PDDA-(Li)TFSI (fig. 4.21g - i). In the F1s spectra, two distinct peaks can be identified at ≈689eV and ≈685eV. For the N1s spectra, two peaks arise at roughly 402.5eV and 399eV. The identified peaks in the F1s spectra, and the N1s spectra were not observed for the pristine cathode composite. In the S2p spectra, again, the red doublets at ≈161eV are observed - which is the PS_4^{3-} originating from the argyrodite. As well as the green doublets at around 162eV, associated with P-S-P - a compound which is formed during the mixing of NMC with LPSC [12]. Furthermore, at a binding energy of ≈169eV, magenta doublets are identified originating from $TFSI^-$ [92].

For the samples 1-PDDA-TFSI and the 2-PDDA-(Li)TFSI samples, the peak at ≈402.5eV is the C-F (CF_3) component, originating from the $TFSI^-$. The CF_3 component of $TFSI^-$ can be seen in the chemical structure representation in figure 2.21 by Del Olmo et al. [18]. The other peak observed in the F1s spectra most likely originates from a LiF compound (≈399eV) which can be present due to ionic liquid degradation [92] [101]. In the N1s spectra, the peak at ≈689eV corresponds to the N^+ element, originating from the cationic PDDA. Moreover, a peak at ≈685eV might also be caused by ionic liquid degradation and can be assigned to the compound nitrogen in the $TFSI^-$ [102]. Lastly, as seen similarly in the S2p spectra of polycrystalline NMC samples of the precious section, the purple doublets at ≈169eV in figures 4.21f) and g), also originate from $TFSI^-$. The absence of these intensities in the pristine single-crystal composite, and the presence of the mentioned compounds in the coated NMC composites, suggests that the coating process was successful. The fraction of $TFSI^-$ in the S2p spectra might indicate that more polymeric ionic liquid has precipitated on the 1-PDDA-TFSI sample.

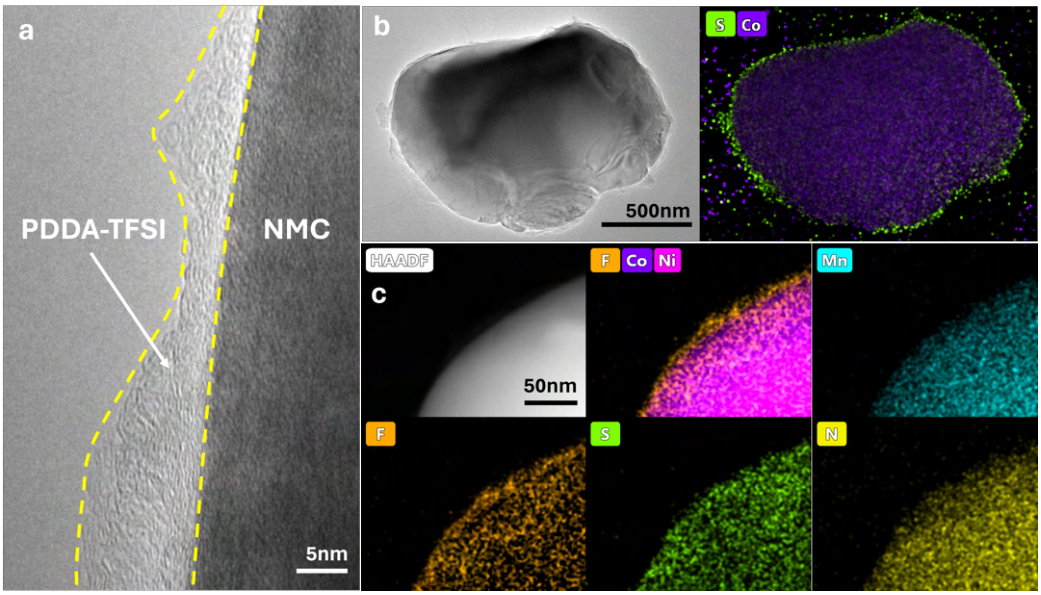

Figure 4.22: Structural characterization and elemental distribution of PDDA-TFSI on Single-crystal NMC, Ni82. a) TEM, b) STEM elemental mapping of S, and Co, and c) HAADF, and STEM elemental mapping of Ni, Mn, Co, F, S, and N.

For the Titan TEM results, we acknowledge support from the Kavli Institute of Nanoscience, Delft University of Technology, and the Netherlands Electron Microscopy Infrastructure (NEMI), project number 184.034.014, part of the National Roadmap and financed by the Dutch Research Council (NWO).

Transmission Electron Microscopy (TEM) was used to study the thickness, morphology, and elemental distribution of the 1wt% PDDA-TFSI coating - 1wt% PDDA-TFSI is the weight percentage of polymer relative to CAM during the microencapsulation procedure for both of the coated samples. The surface of the single-crystal NMC particle is shown to be encapsulated by a PDDA-TFSI coating, with a thickness ranging from 5 to 20 nanometers (figure 4.22a). Figure 4.22b shows a TEM image of a PDDA-TFSI particle, where the coating appears to be thicker in some areas - such as on the left side of the particle. However, looking at the Secondary Transmission Electron Microscopy (STEM) image on the right, the Sulfur and Cobalt at% map shows a more uniformly distributed image of the PDDA-TFSI coating. Cobalt is mostly seen in the bulk of the particle, and sulfur is only at the surface of the particle. Moreover, the High-Angle Annular Dark-Field (HAADF) image and the corresponding Energy Density X-ray spectroscopy (EDX) reveal a uniform distribution of F, S, and N elements on the particle surface (figure 4.22c).

SEM images of uncoated single-crystal NMC and coated NMC presented the comparison of the smooth, spotless surface of the pristine NMC - whereas the coated NMC particles had darker spots on their surface. This was followed by an XPS analysis, which clearly indicated the presence of the CF_3, and the N^+, components originating from the polymer, which were present at the surface of the 1-PDDA-TFSI and 2-PDDA-(Li)TFSI cathode active material. The SEM images, and the XPS analysis, provided evidence for the presence of a coating, but gave limited information on the homogeneity of the polymeric coating. The structural characterization and elemental distribution provided by the TEM images suggest the particles are mostly covered with the polymer, but the thickness of the coating might deviate slightly.

4.3.2. Electrochemical Cycling Performance

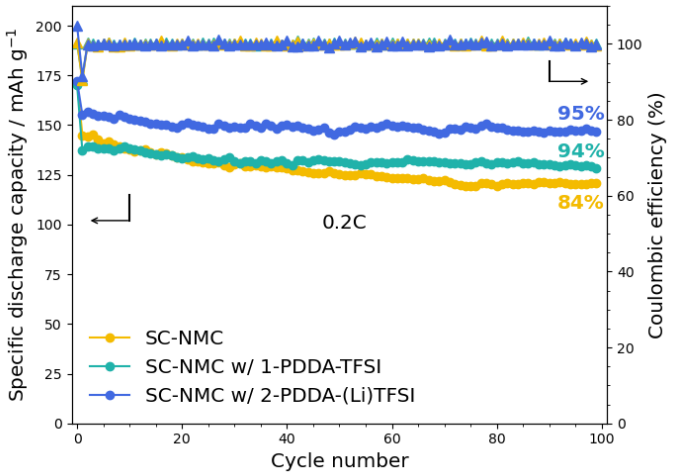

Figure 4.23: Long-term cycling discharge capacity of lithium-indium alloy anode, LPSCl, and single-crystal NMC (Ni82), NMC with a 1wt% PDDA-TFSI, and NMC with 2wt% PDDA-(Li)TFSI, at 0.05C for the first cycle and 0.2C for following cycles. NMC active materials = 10 mg cm^{-2}.

Galvanostatic cycling was performed to investigate the performance of the solid-state batteries with single crystal NMC with polymeric coatings; pristine **SC-NMC**, **SC-NMC w/ 1-PDDA-TFSI**, and **SC-NMC w/ 2-PDDA-(Li)TFSI**. The cycling protocol has been slightly changed; here, only the first cycle is at a C-rate of 0.05C followed by cycles at a C-rate of 0.2C up to 100 cycles. The cycling performance is shown in figure 4.23. The capacity of the first cycle, at 0.05C, is comparable for all samples with an initial capacity of 171.7 mAh/g, 169.9mAh/g, and 172.0mAh/g, for SC-NMC, pristine, with 1-PDDA-TFSI, and 2-PDDA-(Li)TFSI, respectively. Here the initial capacity of the sample with a lithiated coating is highest, followed by the uncoated sample and the sample coated with 1-PDDA-TFSI. For the second cycle, at a C-rate of 0.2C, the discharge capacity starts to deviate per sample variation. The 2^{nd} cycle discharge capacity of 2-PDDA-(Li)TFSI is again the highest with 155.2 mAh/g, and the second highest is the pristine SC-NMC with 144.9 mAh/g. The lowest discharge capacity in the second cycle was 137.3mAh/g for the cell with a 1-PDDA-TFSI coating. The capacity retention is calculated by dividing the discharge capacity of the 100^{th} cycle over that of the 2^{nd} cycle. The capacity retention of the sample with 2-PDDA-(Li)TFSI and 1-PDDA-TFSI are similar at about 94%, and 95%, respectively. However, the difference is that the 2-PDDA-(Li)TFSI coating significantly improves the initial capacity, whereas the 1-PDDA-TFSI coating reduces the initial capacity. The capacity retention of the pristine single-crystal NMC is only ≈84%. The 1-PDDA-TFSI and the 2-PDDA-(Li)TFSI significantly improve the capacity retention of single-crystal NMC. Alongside improved capacity retention, the SSB with 2-PDDA-(Li)TFSI achieved a higher initial capacity of 155.1 mAh/g at a rate of 0.2C. After 100 cycles, another measurement at 0.05C was taken; compared with the first cycle at 0.05C, the sample with 1-PDDA-TFSI showed capacity retention of 96%, and the sample with 2-PDDA-(Li)TFSI an exceptional capacity retention of 99%. The additional cycles are shown in figure C.1, in appendix C.

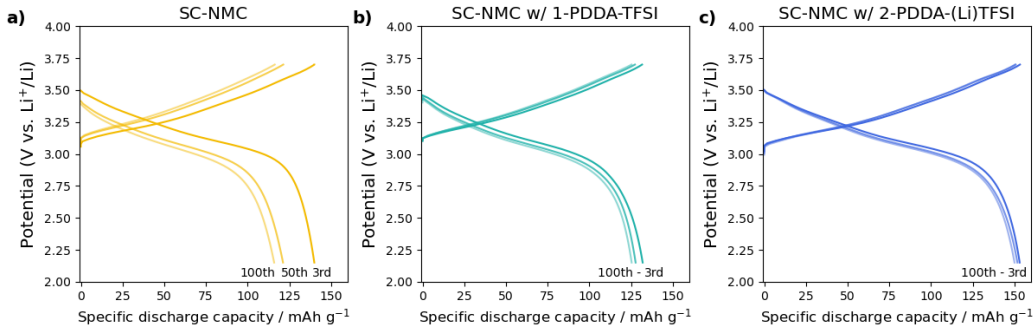

Figure 4.24: Charge-discharge voltage profile for a) SC-NMC, b) SC-NMC with 1wt% PDDA-TFSI, and c) SC-NMC with 2wt% PDDA-(Li)TFSI, at 0.2C for the 3^{rd}, 50^{th}, and the 100^{th} cycle. Cathode active materials ≈ 10 mg cm^{-2}.

Figure 4.24 shows the charge and discharge curves for the 3^{rd}, 50^{th} and 100^{th} cycle of the sample variations. For the sample with pristine SC-NMC, most capacity deterioration occurs in the first 50 cycles. With polymeric protective coatings 1-PDDA-TFSI and 2-PDDA-(Li)TFSI, a slightly higher capacity fade can be detected for the first 50 cycles, slowly heading towards a stable system with negligible capacity fade over the last 50 cycles.

4.3.3. Resistance Evolution Monitoring with Electrochemical Impedance Spectroscopy

The cycling performance of the single-crystal NMC cells displayed clear differences in initial capacity and capacity retention. EIS has been carried out to assess the resistance evolution of interfaces within the solid-state batteries.

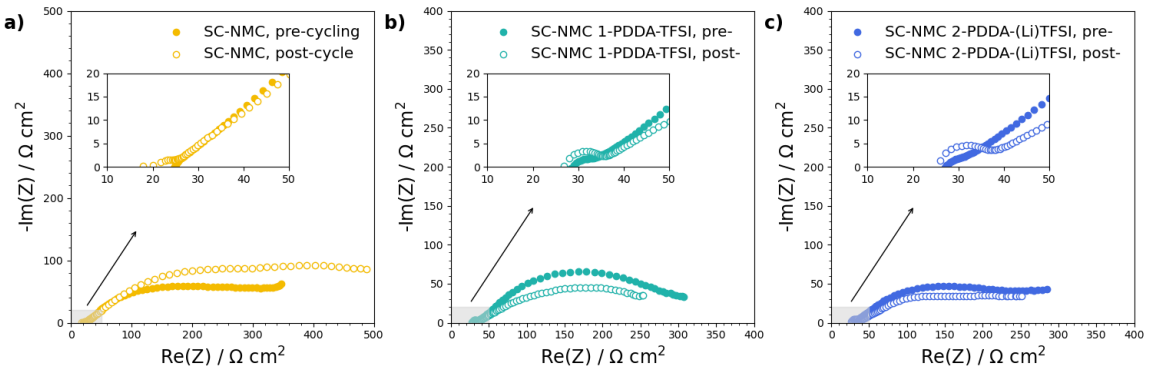

Figure 4.25: a) Nyquist plot for Pristine single-crystal NMC, b) SC-NMC coated with 1wt% PDDA-TFSI, and c) SC-NMC coated with 2wt% PDDA-(Li)TFSI, both pre-cycling and post-100th cycle.

Figure 4.25 shows the Nyquist plots of the samples: SC-NMC, SC-NMC with 1wt% PDDA-TFSI, and 2wt% PDDA-(Li)TFSI, pre- and post-cycling. All EIS measurements were taken at a potential of ≈3.0V, and a frequency range between 10Mhz and 0.1Hz. The exact voltages at the moment impedance measurements at listed in table C.1, in the appendix. Similar to previous sections, a DRT analysis has been carried out to find an equivalent circuit. Figure C.2, in the supplementary materials, shows the DRT curves were constructed using the EIS data as displayed above. The equivalent circuit for fitting the EIS measurements has remained unchanged. The equivalent circuit is shown in figure 4.6, with annotations in table 4.1.

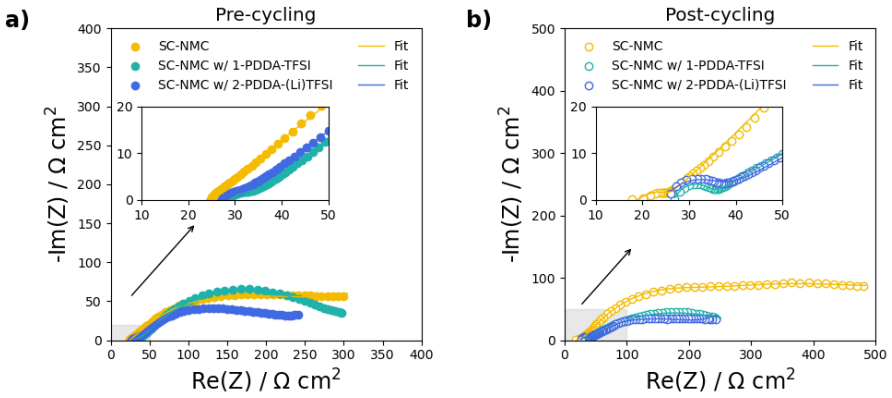

Figure 4.26: Nyquist plots of EIS data fitted to equivalent circuit; a) pre-cycling,a nd b) post-cycling, of samples SC-NMC, SC-NMC with 1wt% PDDA-TFSI, and 2wt% PDDA-(Li)TFSI.

Table 4.5: Interface resistances pre-, and post-cycling, of R_1, R_2, and R_3, for the samples SC-NMC, SC-NMC with 1wt% PDDA-TFSI, and SC-NMC with 2wt% PDDA-(Li)TFSI.

Sample	Pre-cycling			Post-cycling		
	$R_1(\Omega)$	$R_2(\Omega)$	$R_3(\Omega)$	$R_1(\Omega)$	$R_2(\Omega)$	$R_3(\Omega)$
SC-NMC	24.874	27.874	261.71	24.198	95.889	462.66
SC-NMC w/ 1-PDDA-TFSI	28.569	18.234	240.03	29.891	7.497	267.2
SC-NMC w/ 2-PDDA-(Li)TFSI	24.209	10.93	204.63	36.625	6.3702	195.99

The fit of the equivalent to the impedance measurements, pre- and post-cycling, are shown in figure 4.26. Here, the original data points are shown, with the fitted curve as a line. The interface resistances $\mathbf{R}_1$, $\mathbf{R}_2$, and $\mathbf{R}_3$ were determined using the newly fitted impedance data with the use of the RelaxIS 3 software. The interface resistances are listed in table 4.5, where: $\mathbf{R}_1$ corresponds to the bulk resistance, , $\mathbf{R}_2$ refers to the SE-pellet/electrode interface, and $\mathbf{R}_3$ to the NMC/LPSC particle interface resistance [47].

The cell with the lithium salt integrated into the polymeric coatings shows the lowest interface resistances, pre-cycling. The cycling performance of the batteries showed that the sample with 1-PDDA-TFSI had the lowest initial discharge capacity and the cell with 2-PDDA-(Li)TFSI was the highest. The impedance data confirms the findings in the cycling performance results - as the sample with the lowest interface resistances is expected to have the highest discharge capacity. Post-cycling, the interface resistances for the uncoated single-crystal NMC have increased significantly, where the SE-pellet/electrode resistance ($\mathbf{R}_2$) is almost fourfold its value pre-cycling, and the NMC/LPSC interface resistance ($\mathbf{R}_3$) almost doubled. The increase of cell resistances is in line with the capacity fade the cell displayed during electrochemical cycling. The NMC/LPSC interface resistance ($\mathbf{R}_3$) of the sample with 1-PDDA-TFSI is only slightly higher than it was pre-cycling. Again, the cell with the lowest $\mathbf{R}_3$ interface resistances is the cell coated with 2-PDDA-(Li)TFSI.

The impedance spectra for the sample without polymeric coatings show a significant increase in the NMC/LPSC interface resistance, which might be caused by the formation of a CEI, or cathode electrolyte interface. The elevated NMC/LPSC particle interface resistance ($\mathbf{R}_2$) of the sample with a 1-PDDA-TFSI polymeric coating might indicate some form of contact loss of electrodes, but could also indicate decomposition elements at the NMC/LPSC interface. The sample with the 2-PDDA-(Li)TFSI polymeric coatings showed the highest capacity retention (≈95%) and showed negligible differences in pre-cycling and post-cycling interface resistances.

4.3.4. Chemical Stability Analysis with X-ray Photoelectron Spectroscopy

To investigate the effect of the polymer coating on the chemical stability, XPS measurements of the composite cathodes were taken after cycling. In figure 4.27 the S2p and P2p spectra are shown for the samples; SC-NMC, SC-NMC with 1-PDDA-TFSI, and SC-NMC with 2-PDDA-(Li)TFSI. XPS measurements were taken after cycling at roughly 3.0V, corresponding to about 3.6V vs Li^+/Li. A Shirley background was used for line fitting, and the spectra were normalized for their maximum signal intensity to compare the relative contribution of the different compounds. The S2p spectra have closely spaced out spin-orbitals (Δ=1.16eV) [92], and for all cells, four doublets were observed. The main component is detected at a binding energy of ≈161.3eV, corresponding to the $PS_4{}^{3-}$ formation of the Li_6PS_5Cl. Oxygized species were detected at roughly 162.5eV and 163.5eV corresponding to the P-S-P (P_2S_x) and S_x, respectively. S_x is a simplified term used for multiple compounds, including elemental sulfur, that can be responsible for the intensity at that specific binding energy of ≈163.5eV [94]. Additionally, oxidized sulfates were detected in the uncoated sample at ≈169.0eV. The intensity at the same binding energy for coated samples corresponds to the units of TFSI [92]. Similarly to the S2p spectra, the P2p spectra also display spaced out spin orbitals, Δ=0.87eV. Here, the same compounds were detected, namely; $PS_4{}^{3-}$ at round 131eV, and polysulfides at approximately 132.5eV.

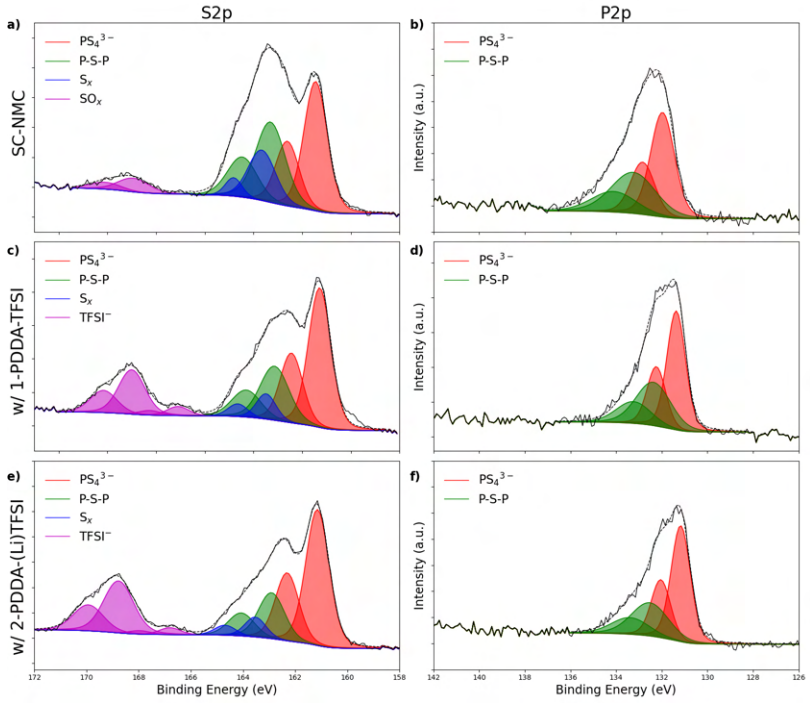

Figure 4.27: Post-cycling XPS measurements- S2p and P2p spectra, of a) - b) single-crystal NMC, c) - d) single-crystal NMC with a 1wt% PDDA-TFSI polymeric protective coating, and e) - f) with 2wt% PDDA-(Li)TFSI.

For all composite cathodes, electrochemical cycling has increased the intensities of oxidized species in the S2p spectra. In the case of uncoated NMC, the intensity of the oxidized species was slightly greater than for the samples coated with PDDA-TFSI. In addition, sulfates were detected in the uncoated sample, which is another compound related to the degradation in sulfide-based SSBs. Reduced TFSI species, $TFSI^-$, were detected for the SSB cells with a PDDA-TFSI coating. In the P2p spectra, a similar ratio of $PS_4{}^{3-}$ to P-S-P was detected as in the S2p spectra for all cells. The average signal position for the polysulfides shows slight deviations per cell, which is a result of the average chain length of the number of sulfite atoms, P-[S_n]-P, in the polysulfides [12]. Assumed is a signal shift towards higher binding energies with increasing n, which is observed in the uncoated SC-NMC composite cathode. Overall, it was observed that

the fraction of oxidized decomposition products, relative to the PS_4^{3-} species assigned to the argyrodite phase, was greater for the uncoated cells than for the PDDA-TFSI coated SSB cells. Therefore, the polymeric coating on single-crystal NMC prevented increased decomposition of the Li_6PS_5Cl solid-electrolyte at the interfaces of the composite cathodes.

4.3.5. Morphology Evolution Analysis with Scanning Electron Microscopy

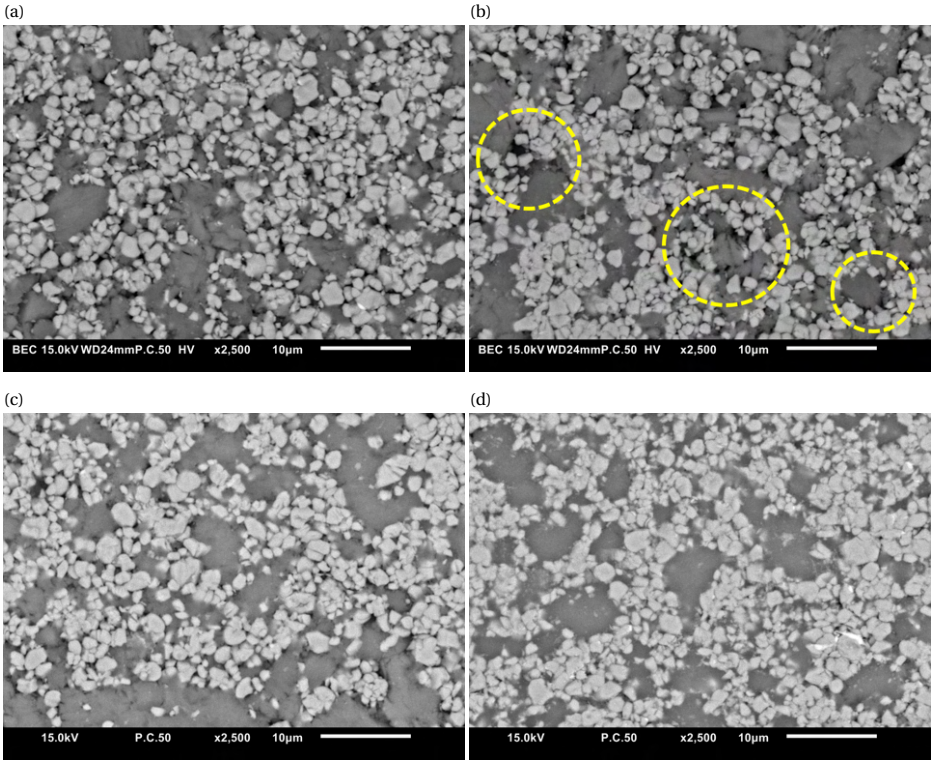

Figure 4.28: SEM images of the cathode electrodes with; a) SC-NMC before cycling b) SC-NMC after cycling c) SC-NMC with 1-PDDA-TFSI after cycling, and d) SC-NMC with 2-PDDA-(Li)TFSI after cycling. All images were taken with BED, and a 15kV acceleration voltage, with a magnification of 2,500x. Yellow circles indicate the contact loss after cycling for uncoated SC-NMC.

The morphology evolution was studied using SEM images of the SC-NMC cathode before cycling, figure 4.28a, and after cycling of SC-NMC with 1-PDDA-TFSI and 2-PDDA-(Li)TFSI, figures 4.28b, c, and d, respectively. For all images, an acceleration voltage of 15kV, and a magnification of 2,500x, was applied. Before cycling, some voids between the NMC particles and the LPSC of the uncoated SC-NMC cathode were observed. Alongside the observed smaller voids, more severe contact loss inside the cathode was seen after cycling. The yellow circles indicate the areas with significant contact loss. After cycling the SSBs with a 1-PDDA-TFSI and 2-PDDA-(Li)TFSI, the contact between the particles was observed to be maintained. The limited number of visible voids of the post-cycled samples compared to the pre-cycled SC-NMC sample, indicated that initial particle contact might have been improved by the polymeric coating as well. To summarize, the investigated SEM images showed two distinct paths of improved contact between the NMC and the SE with the introduction of a polymeric protective coating. These paths suggest i) improved particle contact before cycling and ii) increased contact retention due to the polymeric coating's volume buffering capacity during the lithiation and delithiation of the NMC particles.

4.3.6. Microstrain Analysis with X-ray Diffraction

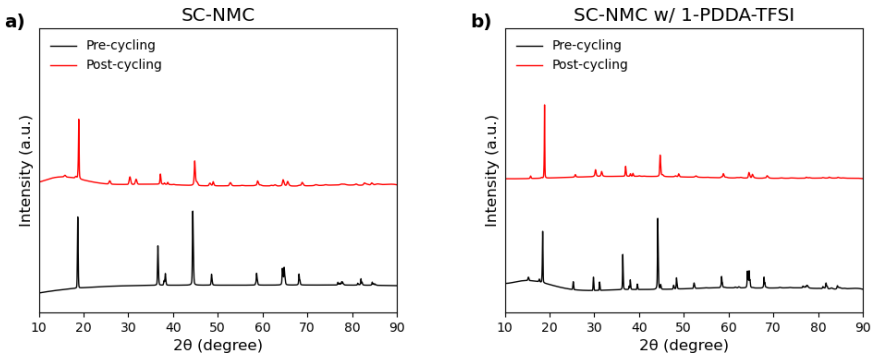

Figure 4.29: Pre-cycling, and post-cycling XRD patterns of a) single-crystal NMC, b) single-crystal NMC with 1wt% PDDA-TFSI.

The XRD patterns pre- and post-cycling, of single-crystal NMC, and single-crystal NMC with a PDDA-TFSI polymeric coating are displayed in figure 4.29. These samples were selected to investigate the evolution of the microstructure of the NMC particles, and the effect of the polymeric coating. Similarly to previously shown XRD patterns of NMC cathode active material, the characteristic peaks 003, 101, and 110 at roughly 18.8°, 36.6°, and 64.8° [100], correlating to the R-3m spacegroup. These peaks were used to study the evolution of the lattice parameters *a*, *b*, and *c*. The raw data was refined using Pawley refinement, which is a method often used as a precursor to Rietveld refinement and can give an indicative 'best fit possible', as well as a direct method to extract intensities and lattice parameters [103]. The observed, calculated, and the difference between the two is shown in figure C.4 of the supplementary materials. The calculated lattice parameters of the pristine single-crystal NMC, and the PDDA-TFSI coated sample are given in table 4.6.

Table 4.6: Pre-, and post-cycling lattice parameters of pristine single-crystal NMC, coated with 1 wt% PDDA-TFSI.

Sample	*a, b* (Å)	*c* (Å)
SC-NMC pre-cycling	2.8726	14.1909
SC-NMC post-cycling	2.8558	14.2867
Difference	*-0.168*	*+0.0958*
SC-NMC w/ 1-PDDA-TFSI pre-cycling	2.8725	14.2089
SC-NMC w/ 1-PDDA-TFSI post-cycling	2.8627	14.2540
Difference	*-0.0098*	*+0.0451*

With the calculated lattice parameters, using Pawley refinement, the pre- and post-cycling lattice spacing was determined. Pre-cycling, the lattice parameters *a*, and *b*, for the NMC with and without a polymeric coating, were roughly the same at ≈2.873 Å. The lattice parameter *c*, displayed higher values for the sample with the polymeric coating of around 14.209 Å, compared to ≈14.191 Å for the sample without the the coating. During cycling, the lattice parameters are expected to display some form of expansion or contraction due to the constant lithiation and delithiation of the NMC particle [6], resulting in a deformation of the microstructure of the particle. The refined results showed a slightly greater (003) peak shift for the uncoated SC-NMC, as well as slightly increased peak broadening (figure C.5), associated with the presence of microstrain on the uncoated NMC [99]. Looking at the differences in the lattice parameters before cycling versus after cycling, we can see the lattice parameters of the uncoated single-crystal NMC have changed more relative to the PDDA-TFSI coated sample, by a factor 2. This suggests that the polymeric interlayers at the surface of the NMC acted as a buffer for the micro-stresses experienced by the cathode active material and reduced the microstrain of the NMC particles.

5

Discussion

The introduction of carbon nanofibers into the cathode composition with polycrystalline NMC had a detrimental impact on the performance of the SSBs with LPSC, shown in figure 4.2. For one, the initial discharge capacity of the cell was significantly worse for the cell with CNF, compared to the cell without any CNF. Here, the results do not align with a study performed by Walther et al. [12], where the initial capacity was improved by introducing vapor-grown carbon fibers. It has to be pointed out that carbon nanofibers and vapor-grown carbon fibers are not the same. Improper storage of the carbon nanofibers can increase the moisture contact of the material and sabotage the premise of improved electronic conduction pathways for improved active materials utilization. For another, the capacity retention of this cell was lowest with only ≈68% after 100 cycles. This is in accordance with the findings in the study by Walther et al. [12]. With the use of XPS measurements, the capacity fade can be associated with the increased formation of sulfates/sulfites (SO_x), polysulfides (P_2S_x), phosphates (PO_x), and lithium phosphate phases (P/Li_xP).

In the same results section, polycrystalline NMC and single-crystal NMC were compared. Regarding initial discharge capacity and capacity retention, the electrochemical performance of single-crystal NMC outperformed that of polycrystalline NMC (figure 4.2). To analyze this outperformance, EIS measurements were taken to study the evolution of interfacial resistances. However, as measurement procedures had not yet been optimized, pre-cycling voltages for EIS measurements varied too much for a fair comparison. This is an issue returning for the polycrystalline NMC samples with polymeric interlayers. Moreover, the frequency ranges were different, making a comparison after cycling difficult.

Two methods were applied for the polymeric coating on polycrystalline NMC: spray-drying and microencapsulation. The cell created with a spray-dried coated NMC had a deficient discharge capacity, shown in figure B.1. In the study by Shi et al. [20], a uniform polymeric coating was obtained via a spray-drying process, which was shown to stabilize the interface between NMC and LPSC. Here, single-crystal NMC with a particle size of ≈3-5μm was coated. This study used polycrystalline NMC with a particle size of ≈10-13μm, which might have blocked the nozzle of the spray-drying installation, hindering the formation of a uniform polymeric coating. Moreover, the installation had a standard inlet tube incompatible with the solvent (acetone) used. XPS measurements of coated NMC powder showed a significant intensity in the Si2p spectra (figure B.2), concluding that cross-contamination had occurred. The presence of silicon on the surface of the NMC particles was the reason for believing that the interface resistance had increased, such that the initial discharge capacity was exceptionally low.

The study by Shi et al. [20] showed that the initial capacity of the cell with a polymeric coating was lower than that of the cells with pristine NMC. It showed that the cell with the highest polymer content had the lowest initial capacity, followed by the sample with a smaller polymer fraction. Similarly, in this study, the batteries with pristine polycrystalline NMC had a higher initial capacity than the coated cells (figure 4.11), which is in line with the study from Shi et al. [20]. However, the 3wt% PDDA-TFSI coated

NMC had a slightly higher initial capacity compared to the cells with 1wt% PDDA-TFSI coated NMC. Post-cycling XPS measurements (figure 4.16) showed a greater fraction of $TFSI^-$ is present in the sample with 3wt% PDDA-TFSI, meaning that indeed more polymer was coated on the 3wt% coated NMC, relative to the 1wt% coated NMC. However, this does not give any conclusive evidence of the uniformity of the coating. The unexpected initial capacity differences can be caused by a non-uniform coating application during the microencapsulation coating process.

Diffraction patterns suggested that the polymeric interlayer in single-crystal NMC acted as a micro-stress buffer, reducing the microstrain on the NMC particles. A study by Wu et al. [104] shows that the value of the lattice parameters is a function of the lithiation state of the NMC particles. Here, lattice *a* experiences contraction, and lattice *c* expansion during charging, or delithiation of the cathode. Moreover, during discharging, or lithiation of the cathode, lattice *a* experiences expansion, and lattice **c** contraction. However, the samples that had undergone XRD measurements had a similar OCP of around 3V (exact values can be found in table C.1). Therefore, it can be ruled out that the lattice parameters' values result from the state-of-charge of the cathode, and the evolution of the lattice parameters most likely causes the microstrain of the single-crystal NMC particles.

6

Conclusions and Recommendations

6.1. Conclusions

This study investigated the effects of polymeric interlayers, in sulfide-based solid-state batteries, on the cathode/solid-electrolyte interface to mitigate contact loss and chemical decomposition, and elevate the cycle stability. The electrochemical performance and the degradation pathways of the NMC/SE interface were studied using galvanostatic cycling, electrochemical impedance spectroscopy, secondary electron microscopy, x-ray photoemission spectroscopy, and x-ray diffraction measurements. Additionally, this study investigated the effects of carbon nanofibers as a conductive additive in the cathode composite mix with polycrystalline NMC and argyrodite. The research questions formulated in the introduction are addressed below.

The influence of the conductive additive carbon nanofibers on the cycling performance and the cycle stability in polycrystalline $LiNi_{0.8}Mn_{0.1}Co_{0.1}O_2$ was investigated. Galvanostatic cycling revealed that CNF reduced the initial capacity, and significantly decreased the capacity retention of the SSB cells. EIS measurements before cycling showed that the charge transfer resistance between NMC and LPSC particles was increased considerably with the introduction of CNF in the composite cathodes, underlining the reduced initial capacity. This outcome provides reasoning to think that the CNFs obstructed lithium ion conduction, which is detrimental to the SSB capacity. XPS measurements showed that chemical degradation played a significant role in the capacity fade of the cells. The observed capacity fade was associated with the formation of decomposition elements sulfates/sulfites (SO_x), polysulfides (P_2S_x), phosphates (PO_x), and lithium phosphate phases (P/Li_xP), which were detected on the cathode using XPS. To summarize, the results showed that CNFs increased capacity deterioration without improving the initial capacity of the cathode for the first cycles.

The effect of a poly(diallyldimethylammonium)-bis(trifluoro- methanesulfonyl)imide coating on polycrystalline NMC811 was tested and showed slightly improved capacity retention. The polymer coating was applied with two methods: i) spray drying, and ii) microencapsulation. Microencapsulation proved to be a lab-scale method that produced a polymer coating with improved long-term cycling performance compared to uncoated NMC. Impedance data showed that the NMC/LPSC particle interface resistance was lower for the samples with a PDDA-TFSI coating than the uncoated NMC. In addition, the PDDA-TFSI coating effectively suppressed the formation of sulfates and significantly reduced the extent of contact loss between particles.

The PDDA-TFSI polymer coating on single-crystal NMC showed greater capacity retention, and with the addition of LiTFSI in the polymer, active mass utilization improved compared to SSBs with uncoated NMC. SEM, XPS, and TEM measurements showed that by adding 1wt% of PDDA-TFSI, the microencapsulation method created a coating of 5 nm to 20 nm thickness around most of the NMC. EIS measurements showed minimal resistance evolution across grain boundaries in the cathode for the polymer-coated samples, compared to a severe resistance increase for uncoated NMC. XPS, after cycling, showed the polymer

coating effectively suppressed the formation of oxidized species and confirmed the chemical passivation of the NMC/SE interface. Furthermore, the polymer coating exhibited improved particle contact after electrochemical cycling, established by SEM. In addition, XRD measurement showed that the PDDA-TFSI coating reduced the degree of particle deformation, which confirmed the volume buffering characteristics of the polymer. This study showed a lab-scale approach for the coating of NMC with a commercially available polymer to mitigate chemical and mechanical degradation in Li_6PS_5Cl-based solid-state batteries.

6.2. Recommendations

This study revealed insights into the effect of polymeric interlayers on the cycle stability in sulfide-based SSBs. Based on these findings, the following recommendations are suggested to further increase the understanding of the role of the coating in Li-ion diffusion across the cathode/solid-electrolyte interface. Additionally, recommendations are made for further optimization of the polymer application, the usage of mixed ionic electronic conducting (MIEC) polymers, and exploring different operating conditions of SSBs.

In this work, a polymeric coating with lithium salts was shown to improve SSB capacity; one reason for this can be improved Li-ion conduction over the cathode grain boundaries. Exchange-NMR, nuclear magnetic resonance, is a technique that can be used to quantify Li-ion equilibrium exchange across the solid-electrolyte/electrode interface [105]. To investigate the contribution of the polymeric coating on the Li^+ diffusion between the NMC electrode, the PDDA-(Li)TFSI, and the Li_6PS_5Cl solid-electrolyte, solid-state Li^6 NMR measurements are recommended for future studies.

The preparation of the PDDA-TFSI coating on cathode active material was performed with two methods: microencapsulation via dissolution and precipitation and spray drying. In this work, spray drying was abandoned after the first attempt due to the incompatibility of the feed tube with the acetone solution resulting in a cross-contamination of silicon, and the clogging of the nozzle with the usage of polycrystalline particles with a D_{50} of 10 to 13 μm. Alongside, the preparation of the coating via dissolution and precipitation displayed a coating with a thickness varying from 5nm to 20nm. For future work, coating preparation with the Buchi Mini Spray Dryer is a technique that could be explored for a thin polymer coating with a more uniform thickness. Recommended is the use of a feed tube compatible with acetone, and cathode active materials of a smaller particle size, such as the single-crystal NMC with a D_{50} of 3 to 5 μm.

Besides these recommendations, further research can be done into the effects of different types of polymer coatings. A recommended candidate for future work would be the preparation of a mixed ionic electronic conductive (MIEC) polymer. As stated in chapter 2, MIEC polymers are unique for their ability to conduct ions as well as electrons [15], improving SSB kinetics alongside the premise of the promise of improved cycle stability.

To further optimize SSB performance, it is recommended to explore the dependency of operating temperature, C-rate, and cell closing pressure. In this study, all experiments were conducted at room temperature; it is important to acknowledge that practical operating conditions, such as those in electric vehicles, often involve higher temperatures. Therefore, further research can be conducted into cycling performance at higher operating temperatures. Another practical demand for rechargeable batteries is fast charging and greater power output during discharge; additional experiments can be done to explore SSB performance at higher C-rates and support the demand for faster charge and discharge rates. Another impracticality of solid-state batteries is the high closing pressures to ensure electrode/solid-electrolyte contact. Polymer interlayers have been shown to improve particle contact retention, potentially enabling operation at lower closing pressures. Addressing and optimizing for higher operating temperatures, higher C-rates, and lower closing pressures will improve SSB performance and stability in practical, real-world scenarios.

Bibliography

[1] Jürgen Janek and Wolfgang G. Zeier. A solid future for battery development. *Nature Energy*, 1:16141, 2016.

[2] Darren H. S. Tan, Abhik Banerjee, Zheng Chen, and Ying Shirley Meng. From nanoscale interface characterization to sustainable energy storage using all-solid-state batteries. *Nature Nanotechnology*, 15:170–180, 2020.

[3] Jijeesh Ravi Nair, Laura Imholt, Gunther Brunklaus, and Martin Winter. Lithium metal polymer electrolyte batteries: Opportunities and challenges. *The Electrochemical Society*, 28, 2019.

[4] Darren H. S. Tan, Erik A. Wu, Han Nguyen, Zheng Chen, Maxwell A. T. Marple, Jean-Marie Doux, Xuefeng Wang, Hedi Yang, Abhik Banerjee, and Ying Shirley Meng. Elucidating reversible electrochemical redox of li6ps5cl solid electrolyte. *ACS Energy Letter*, 4:2418–2427, 2019.

[5] A. L. Santhosha, Lukas Medenbach, Johannes R. Buchheum, and Philipp Adelhelm. The indium-lithium electrode in solid-state lithium-ion batteries: Phase formation, redox potentials, and interface stability. *Batteries Supercaps*, 2:524–529, 2019.

[6] Philip Minnmann, Florian Strauss, Anja Bielefeld, Raffael Ruess, Philipp Adelhelm, Simon Burkhardt, Sören L. Dryer, Enrico Trevisanello, Helmut Ehrenberg, TOrtsen Breesinski, Felix G. Richter, and Jürgen Janek. Designing cathodes and cathode active materials for solid-state batteries. *Advanced Energy Materials*, 12, 2022.

[7] Jürgen Janek and Wolfgan G. Zeier. Challenges in speeding up solid-state battery development. *Nature Energy*, 18:230–240, 2023.

[8] Saneyuki Ohno, Carolin Rosenbach, Geroge F. Dewald, Jürgen Janek, and Wolfgang G. Zeier. Linking solid electrolyte degradation to charge carrier transport in the thiophosphate-based composite cathode toward solid-state lithium-sulfur batteries. *Advanced Functional Materials*, 31(18): 2010620, 2021.

[9] Philip Minnmann, Lars Quillman, Simon Burkhardt, Felix H. Richter, and Jürgen Janek. Quantifying the impact of charge transport bottlenecks in composite cathodes of all-solid-state-batteries. *The Electrochemical Society*, 168:040537, 2021.

[10] Tan Shi, Qingsong Tu, Yaosen Tian, Yihan Xiao, Lincoln J. Miara, Olga Kononova, and Gerbrand Ceder. High active material loading in all-solid-state battery electrode via particle size optimization. *Advanved Energy Materials*, 10:190281, 2020.

[11] Kausthubh G. Naik, Bairav S. Vishnugopi, and Partha P. Mukherjee. Kinetics or transport: Whither goes the solid-state battery cathode? *Applied Materials and Interfaces*, 13:29754–29765, 2022.

[12] Felix Walther, Simon Randau, Yannick Schneider, Joachim San Marcus Rohnke, Felix H. Richter, Wolfgang G. Zeier, and Jürgen Janek. Influence of carbon additives on the decomposition pathways in cathodes of lithium thiophosphate-based all-solid-state batteries. *Chemistery of Materials*, 32: 6123–6136, 2020.

[13] Yihan Xiao, Lincoln J. Miara, Yan Wang, and Gerbrand Ceder. Computational screening of cathode coatings for solid-state batteries. *Joule*, 3:1252–1275, 2019.

[14] Sixu Deng, Yipeng Sun, Xia Li, Zhouhong Ren, Jianwen Liang, Kieran Doyle-Davis, Jianneng Liang, Weihan Li, Mohammad Norouzi Banis, Ruying Li Qian Sun, Yongfeng Hu, Huan Huang, Li Zhang, Shigang Lu, Jun Luo, and Xueliang Sun. Eliminating the detrimental effects of conductive agents in sulfide-based solidstate batteries. *ACS Energy Letters*, 5:1243–1251, 2020.

[15] Elina Nazmutdinova, Carolin Rosenbache, Christina Schmidt, Sangchai Sarawutanukulf, Kerstin Neuhausa, André Gröschel, and Nella M. Vargas-Barbosaa. Water-mediated synthesis of halide solid electrolyte and conducting polymer hybrid materials for all solid-state batteries. *Energy*, 1, 2023.

[16] Georgina L. Gregory, Hui Gao, Boyang Liu, Xiangwen Gao, Gregory J. Rees, Mauro Pasta, Peter R. Bruce, and Charlotte K. Williams. Buffering volume change in solid-state battery composite cathodes with co2-derived block polycarbonate ethers. *Journal of The American Chemical Society*, 144: 17477–17486, 2022.

[17] Tae Young Kwona, Kyu Tae Kima, Dae Yang Oha, Yong Bae Songa, Seunggoo Juna, and Yoon Seok Junga. Three-dimensional networking binders prepared in situ during wet-slurry process for all-solid-state batteries operating under low external pressure. *Energy Storage Materials*, 49:219–226, 2022.

[18] Rafael Del Olmo, Gregorio Guzmán-González, Ilda O. Santos-Mendoza, David Mecerreyes, Maria Forsyth, and Nerea Casado. Unravelingthe influence of li+-cation and tfsi-anion in poly(ionic liquid) binders for lithium-metal batteries. *Batteries and Supercaps*, 6:e20220051, 2023.

[19] S. Vauthier, M. Alvarez-Tirado, G. Guzman-Gonz, L.C. Tome, S. Cotte, L. Castro, A. Gueguen, D. Mecerreyes, and N. Casado. High-performance pyrrolidinium-based poly(ionic liquid) binders for li-ion and li-air batteries. *Materials Today Chemistery*, 27:101293, 2023.

[20] Bing-Xuan Shi, Yuriy Yusim, Sudeshna Sen, Thomas Demuth, Raffael Ruess, Kerstin Volz, Anja Henss, and Felix H. Richter. Mitigating contact loss in li6ps5cl-based solid-state batteries using a thin cationic polymer coating on ncm. *Advanced Energy Materials*, 13:2300310, 2023.

[21] Alexandros Ch. Lazanas and Mamas I. Prodromidis. Electrochemical impedance spectroscopya tutorial. *ACS Measurement Science*, 3:162–193, 2023.

[22] Jiangong Zhu, Michael Knapp, Xinyang Liu, Peng Yan, Haifeng Dai, Xuezhe Wei, and Helmut Ehrenberg. Low-temperature separating lithium-ion battery interfacial polarization based on distribution of relaxation times (drt) of impedance. *IEEE TRANSACTIONS ON TRANSPORTATION ELECTRIFICATION*, 7, 2021.

[23] Teighmouth Science and Technology Centre. *A beginners Guide to XPS*. 2017. URL `http://www.tscienceandtech.org.uk/CourseNotesTSTC2017.pdf`.

[24] NanoScience Instruments. What is scanning electron microscopy?, 2023. URL `https://www.nanoscience.com/techniques/scanning-electron-microscopy/`.

[25] Chenmin Zhao, Bing Wang, Shuncong Zhong, Md. Akhtaruzzaman, Wei Liang, and Hui Chen. Polymer-based nanoscale materials for surface coatings. 2023. URL `https://www.sciencedirect.com/book/9780323907781/polymer-based-nanoscale-materials-for-surface-coatings`.

[26] Richard Schmuch, Ralf Wagner, Gerhard Hörpel, Tobias Placke, and Martin Winter. Performance and cost of materials for lithium-based rechargeable automotive batteries. *Nature Energy*, 3:267–278, 2018.

[27] Kun Joong Kim, Moran Balaish, Masaki Wadaguchi, Lingping Kong, and Jennifer L. M. Rupp. Solid-state li–metal batteries: Challenges and horizons of oxide and sulfide solid electrolytes and their interfaces. *Advanced Energy Materials*, 11, 2021.

[28] Ting Chen, Long Zhang, Zhaoxing Zhang, Peng Li, Hongqjang Wang, Chuang Yu, Xinlin Yan, Limin Wang, and Bo Xu. Argyrodite solid electrolyte with a stable interface and superior dendrite suppression capability realized by zno co-doping. *Applied Materials and Interfaces*, 11(43):40808–40816, 2019.

[29] Jeremie Auvergniott, Alice Cassel, Jean-Bernard Ledeuil, Virginie Viallet, Vincent Seznec, and Remi Dedryvere. Interface stability of argyrodite li6ps5cl toward licoo2, lini1/3co1/3mn1/3o2, and limn2o4 in bulk all-solid-state batteries. *Chemistery of Materials*, 29(9):3883–3890, 2017.

[30] Arumugam Manthiram. A reflection on lithium-ion battery cathode chemistery. *Nature Communications*, 11:1550, 2020.

[31] Katharina Märker, Philip J. Reeves, Choa Xu, Kent J. Griffith, and Clare P. Grey. Evolution of structure and lithium dynamics in lini0.8mn0.1co0.1)2 (nmc811) cathodes during electrochemical cycling. *Chemistery of Materials*, 31(7):2545–2554, 2019.

[32] George E. Blomgren. The development and future of lithium ion batteries. *Journal of The Electrochemical Society*, 164(1):5019–5025, 2017.

[33] Jayse Langdon and Arumugam Manthiram. A perspective on single-crystal layered oxide cathodes for lithium-ion batteries. *Energy Storage Materials*, 37:143–160, 2021.

[34] Dae Yang Oh, Young Eun Choi, Dong Hyeon Kim, Young-Gi Lee, Byeong-Su Kim, Jongnam Park, Hiesang Sohn, and Yoon Seok Jung. All-solid-state lithium-ion batteries with tis2 nanosheets and sulphide solid electrolytes. *Journal of Materials Chemistery*, 4:10329–10335, 2016.

[35] Zachary Ruff, Chloe S. Coates, Katharina Märker, Amoghavarsha Mahadevegowda, Chao Xu, Megan E. Penrod, Caterina Ducati, and Clare P. Grey. O3 to o1 phase transitions in highly delithiated nmc811 at elevated temperatures. *Chemistry of Materials*, 35:4979–4987, 2023.

[36] Allan J. Jacobson and Linda F. Nazar. Intercalation chemistry. *Encyclopedia of Inorganic Chemistry*, 2006.

[37] Young-Ok Kim and Su-Moon Park. Intercalation mechanism of lithium ions into graphite layers studied by nuclear magnetic resonance and impedance experiments. *Journal of the Electrochemical Society*, 148:A194, 2001.

[38] Raimund Koerver, Wenbo Zhang, Lea de Biasi, Simon Schweidler, Aleksandr O. Kondrakov, Stefan Kolling, Torsten Brezesinki, Pascal Hartmann, Wolfgan G. Zeier, and Jürgen Janek. Chemomechanical expansion of lithium electrode materials - on the route to mechanically optimized all-solid-state-batteries. *Energy Environmental Science*, 11:2142, 2018.

[39] Raimund Koerver, Isabel Aygün, Thomas Leichtweiß, Christian Dietrich, Wenbo Zhang, Jan O. Binder, Pascal Hartmann, Wolfgang G. Zeier, and Jürgen Janek. Capacity fade in solid-state batteries: Interphase formation and chemomechanical processes in nickel-rich layered oxide cathodes and lithium thiophosphate solid electrolytes. *Chemistry of Materials*, 29:5574–5582, 2017.

[40] Svenja-K. Otto, Luise M. Rieger, Till Fuchs, Sven Kayser, Pasal Schweitzer, Simon Burkhardt, Anja Henss, and Jürgen Jannek. In situ investigation of lithium metal-solid electrolyte anode interfaces with tof-sims. *Advanced Materials Interfaces*, 9:2102387, 2022.

[41] Ziyang Ning, Dominic Spencer Jolly, Guachen Li, Robin De Meyere, Shengda D. Pu, Yang Chen, Jitti Kasemchianan, Johannes Ihli, Chen Gong, Boyang Liu, Dominic L. R. Melvin, Anne Bonnin, Oxana Magdyskyuk, Paul Adamson, Gareth O. Hartley, CHares W. Monroe, T. James Marrow, and Peter G. Bruce. Visualizing plating-induced cracking in lithium anode solid-electrolyte cells. *Nature Materials*, 20:1121–1129, 2021.

[42] Thorben Krauskopf, Rabea Dipper, Hannah Hartmann, Klaus Peppler, Boris Mogwitz, Felix H. Richter, Wolfgang G. Zeier, and Jürgen Jannek. Lithium-metal growth kinetics on llzo garnet-type solid electrolytes. *Joule*, 3:2165–2178, 2019.

[43] Kian Kerman, Alan Luntz, Venkatasubramanian Viswanathan, Yet-Ming Chiang, and Zhebo Chen. Review—practical challenges hindering the development of solid state li ion batteries. *Journal of The Electrochemical Society*, 164:1731, 2017.

[44] Mauro Pasta, David Armstrong, Zachary L. Brown, Junfu Bu, Martin R. Castell, Peiyu Chen, Alan Cocks, Serena A. Corr, Edmund J. Cussen, Ed Darnbrough, Vikram Deshpande, Christopher Doerrer, Matthew S. Dyer, Hany El-Shinawi, Norman Fleck, Patrick Grant, Georgina L. Gregory, Chris Grovenor, Laurence J. Hardwick, John T.S. Irvine, Hyeon Jeong Lee, Guanchen Li, Emanuela Liberti, Innes McClelland, Charles Monroe, Peter D. Nellist, Paul R. Shearing, Elvis Shoko, Weixin Song, Dominic Spencer Jolly, Stephen J. Turrell Christomer I. Thomas, Mihkel Vestli, Charlotte K. Williams, Yundong Zhou, and Peter G. Bruce. 2020 roadmap on solid-state batteries. *Journal of Physics: Energy*, 2:032008, 2020.

[45] Jinlong Fu, Hywel R. Thomas, and Chenfeng Li. Toruosity of porous media: Image analysis and physical simulation. *Earth-Science Reviews*, 212:103439, 2021.

[46] Young Jin Nam, Dae Yang Oh, Sung Hoo Jung, and Yoon Seok Jung. Toward practical all-solid-state lithium-ion batteries with high energy density and safety: Comparative study for electrodes fabricated by dry- and slurry-mixing processes. *Journal of Power Sources*, 375:93–101, 2018.

[47] Wenbo Zhang, Domink A. Weber, Harald Weigand, Tobias Arlt, Ingo Manke, Daniel Schröder, Raimund Koerver, Thomas Leichtweiss, Pascal Hartmann, Wolfgang G. Zeier, and Jüregen Janek. Interfacial processes and influence of composite cathode microstructure controlling the performance of all-solid-state lithium batteries. *Applied Material Interfaces*, 9:17835–17845, 2017.

[48] Anja Bielefeld, Dominik a. Weber, and Jürgen Janek. Microstructural modeling of composite cathodes for all-solid-state batteries. *Journal of Physical CHemistry C*, 123:1626–1634, 2019.

[49] Michael E. Spahr, Dietrich Goers, Antonio Leone, Salvatore Stallone, and Eusebiu Grivei. Development of carbon conductive additives for advanced lithium ion batteries. *Journal of Power Sources*, 196:3404–3413, 2011.

[50] Wembo Zhang, Thomas Leightweiss, Sean P. Culver, Raimund Koerver, Dyuman Das, Dominik A. Weber, Wolfgang G. Zeier, and Jürgen Janek. The detrimental effects of carbon additives in li10gep2s12-basedsolid-state batteries. *ACS Applied Materials Interfaces*, 9:35888–35896, 2017.

[51] Sean P. Culver, Raimund Koerver, Wolfgang G. Zeier, and Jürgen janek. On the functionality of coatings for cathode active materials in thiophosphate-based all-solid-state batteries. *Advanced Energy Materials*, 9:1900626, 2019.

[52] Simon Hein, Timo Danner, Daniel Westhoff, Benedikt Prifling, Rares Scurtu, Lea Kremer, Alice Hoffmann, Andre Hilger, Markus Osenberg, Ingo Manke, Margret Wohlfarht-Mahrens, Volker Schmidt, and Arnulf Latz. Influence of conductive additives and binder on the impedance of lithium-ion battery electrodes: Effect of morphology. *Journal of The Electrochemical Society*, 167: 013546, 2020.

[53] Xia Li, Zhouhong Ren, Hohammad Norouzi Banis, Sixu Deng, Yang Zhao, Qian Sun, Changhong Wang, Xiaofei Yang, Weihan Li, Jianwen Liang, Xiaona Li, Yipeng Sun, Keegan Adair, Ruying Li, Yongfeng Hu, Tsun-Kong Sham, Huan Huang, Li Zhang, Shigang Lu, Jun Luo, and Xueliang Sun. Unravelling the chemistry and microstructure evolution of a cathodic interface in sulfide-based all-solid-state li-ion batteries. *ACS Energy Letters*, 4:2480–2488, 2019.

[54] Conrad L. Bender, Pascal Hartmann, Milos Vracar, Philipp Adelhelm, and Jürgen Janek. On the thermodynamics, the role of the carbon cathode, and the cycle life of the sodium superoxide (nao 2) battery. *Advanced Energy Materials*, 4:1301863, 2014.

[55] Fudong Han, Yizhou Zhu, Xingfeng He, Yifei Mo, and Chunsheng Wang. Electrochemical stability of li10gep2s12 and li7la3zr2o12 solid electrolytes. *Advanced Energy Materials*, page 1501590, 2016.

[56] Florain Strauss, Dominik Stepien, Julia Maibach, Lukas Pfaffman, Sylvio Idris, Pascal Hartmann, and Torten Brezesinski. Influence of electronically conductive additives on the cycling performance of argyrodite-based all-solid-state batteries. *Royal Society of Chemistry*, 10:1114–1119, 2020.

[57] J.Y. Song, Y.Y. Wang, and C.C. Wan. Review of gel-type polymer electrolytes for lithium-ion batteries. *Journal of Power Sources*, 77:182–197, 1999.

[58] Sang Wook Park, Gwangseok Oh, Jun-Woo Park, Yoon-Cheol Ha, Sang-Min Lee, Seog Young Yoon, and Byung Gon Kim. Graphitic hollow nanocarbon as a promising conducting agent for solid-state lithium batteries. *Small*, 15:1900235, 2019.

[59] Pratik R. Das, Lidiya Komsiyska, Oliver Osters, and Gunther Wittstock. Pedot: Pss as a functional binder for cathodes in lithium ion batteries. *Journal of The Electrochemical Society*, 162:A674, 2015.

[60] Wenwu Zeng, Lei Wang, Xiang Peng, Tiefeng Liu, Youyu Jiang, Fei Qin, Lin Hu, Paul K. Chu, Kaifu Huo, and Yinhua Zhou. Enhanced ion conductivity in conducting polymer binder for high-performance silicon anodes in advanced lithium-ion batteries. *Advanced Energy Materials*, 8: 1702314, 2018.

[61] Gui-Liang Xu, Qiang Liu, Kenneth K. S. Lau, Yuzi Liu, Xiang Liu, Han Gao, Xinwei Zhou, Minghao Zhuang, Yang Ren, Jiadong Li, Minhua Shao, Minggao Ouyang, Feng Pan, Zonghai Chen, Khalil Amine, and Guohua Chen. Building ultraconformal protective layers on both secondary and primary particles of layered lithium transition metal oxide cathodes. *Nature Energy*, 4:484–494, 2019.

[62] Leire Meabe, Tan Vu Huynh, Nerea Lago, Haritz Sardon, Chunmei Li, Luke A. O'Dell, Michel Armand, Maria Forsyth, and David Mecerreyes. Poly(ethylene oxide carbonates) solid polymer electrolytes for lithium batteries. *Electrachimica Acta*, 264:367–375, 2018.

[63] Kuirong Deng, Shuanjin Wang, Shan Ren, Dongmei Han, Min Xiao, and Yuezhong Meng. A novel single-ion-conducting polymer electrolyte derived from co2-based multifunctional polycarbonate. *Applied Materials and Interfaces*, 8:33642–33648, 2016.

[64] C. Resetco, B. Hendriks, N. Badi, and F. Du Prez. Thiol–ene chemistry for polymer coatings and surface modification – building in sustainability and performance. *Materials Horizons*, 4:1041, 2017.

[65] Kyulin Lee, Sangryun Kim, Jesik Park, Sung Hyeon Park, Ali Coskun, Dae Soo Jung, Woosuk Cho, and Jang Wook Choi. Selection of binder and solvent for solution-processed all-solid-state battery. *Journal of the Electrochemical Society*, 146:A2075, 2017.

[66] Dae Yang Oh, Young Jin Nam, Kern Ho Park, Sung Hoo Jung, Kyu Tae Kim, A. Reum Ha, and Yoon Seok Jung. Slurry-fabricable li+-conductive polymeric binders for practical all-solid-state lithium-ion batteries enabled by solvate ionic liquids. *Advanced Energy Materials*, 9:1802927, 2019.

[67] Darryl A. Boyd. Sulfur and its role in modern materials science. *Angewandte Chemie International Edition*, 55:15486–15502, 2016.

[68] Xiaoen Wang, Gaetan M. A. Girard, Haijin Zhu, Ruhamah Yunis, Douglas R. MacFarlane, David Mecerreyes, Aninda J. Bhattacharyya, Patrick C. Howlett, and Maria Forsyth. Poly(ionic liquid)s/electrospun nanofiber composite polymer electrolytes for high energy density and safe li metal batteries. *Applied Energy Materials*, 6:6237–6245, 2019.

[69] Ioannis Spanos, Sebastian Neugebauer, Ryan Guterman, Jiayin Yuan, Robert Schlöglb, and Markus Antonietti. Poly(ionic liquid) binders as ionic conductors and polymer electrolyte interfaces for enhanced electrochemical performance of water splitting electrodes. *Sustainable Energy and Fuels*, 2:1446–1451, 2018.

[70] Liliana C. Tomé, David Mecerreyes, Carmen S.R. Freire, Luís Paulo N. Rebelo, and Isabel M. Marrucho. Pyrrolidinium-based polymeric ionic liquid materials: New perspectives for co2 separation membranes. *Journal of Membrane Science*, 428:260–266, 2013.

[71] Xiaoen Wang, Haijin Zhu, Gaetan M. A. Girard, Ruhamah Yunis, Douglas R. MacFarlane, David Mecerreyes, Aninda J. Bhattacharyya, Patrick C. Howlett ORCID logo, and Maria Forsyth. Preparation and characterization of gel polymer electrolytes using poly(ionic liquids) and high lithium salt concentration ionic liquids. *Journal of Materials Chemistery A*, 5:23844–23852, 2017.

[72] Zhenguang Gao, Shaojian Zhang, Zhigen Huang, Yanqiu Lu, Weiwei Wang, Kai Wang, Juntao Li, Yao Zhou, Ling Huang, and Shigang Sun. Protection of li metal anode by surface-coating of pvdf thin film to enhance the cycling performance of li batteries. *Chinese Chemical Letters*, 30:525–528, 2019.

[73] Bhavesh B. Patel, Jayvadan K. Patel, and Subhashis Chakraborty. Review of patents and application of spray drying in pharmaceutical, food and flavor industry. *Recent Pat. Drug Deliv. Formul.*, 8: 63–78, 2014.

[74] La Hu Feng Fu. Advanced high strength natural fibre composites in construction, 2017. URL `https://www.sciencedirect.com/book/9780081004111/advanced-high-strength-natural-fibre-composites-in-construction`.

[75] N.G. Hoogeveen, C.W. Hoogendam, R. Tuinier, and M.A. Cohen Stuart. Adsorption of weak polyelectrolytes on amphoteric oxide surfaces. *International Journal of Polymer Analysis and Characterization*, 1:315–328, 1995.

[76] Geraldine Guyard Stephen Greenberg Nava Dayan Scott Hawkins, Mike Wolf. *Delivery System Handbook for Personal Care and Cosmetic Products*. 2005. URL `https://www.sciencedirect.com/book/9780815515043/delivery-system-handbook-for-personal-care-and-cosmetic-products#book-info`.

[77] P. Yu, J. A. Ritter, R. E. White, and B. N. Popov. Ni-composite microencapsulated graphite as the negative electrode in lithium-ion batteries. *Journal of the Electrochemical Society*, 147:1280–1285, 2000.

[78] Chi-An Chen and Chia-Chen Li. Microencapsulating inorganic and organic flame retardants for the safety improvement of lithium-ion batteries. *Solid State Ionics*, 323:56–63, 2018.

[79] Buchi. Buchi mini spray dryer s-300. URL `https://www.buchi.com/en/products/instruments/spray-dryer-s300`.

[80] Xiaoen Wang, Fangfang Chen, Gaetan M.A. Girard, Haijin Zhu, Douglas R. MacFarlane, David Mecerreyes, Michel Armand, Patrick C. Howlett, and Maria Forsyth. Poly(ionic liquid)s-in-salt electrolytes with co-coordination-assisted lithium-ion transport for safe batteries. *Joule, Cell Press*, 3: 2687–2702, 2019.

[81] Solvionic. The metallic salts, lithium(i) bis(trifluoromethanesulfonyl)imide 99.9 URL `https://en.solvionic.com/products/lithiumi-bistrifluoromethanesulfonylimide-99.9`.

[82] Wesley M. Dos, Chao Xu, Claire P. Grey, and Michael F.L. De Volder. Effect of anode slippage on cathode cutoff potential and degradation mechanisms in ni-rich li-ion batteries. *Cell Reports Physical Science*, 1:100253, 2020.

[83] Seong Jin An, Jianlin Li, Zhijia Du, Claus Daniel, and David L. Wood III. Fast formation cycling for lithium ion batteries. *Journal of Power Sources*, 342:846–852, 2017.

[84] Wenxuan Hu, Yufan Peng, Yimin Wei, and Yong Yang. Application of electrochemical impedance spectroscopy to degradation and aging research of lithium-ion batteries. *The Journal of Physical Chemistry*, 127:4465–4495, 2023.

[85] Science Intstruments Bio-Logic. Distribution of relaxation times (drt): An introduction, 2017. URL `https://www.biologic.net/wp-content/uploads/2019/08/battery-eis-distribution-of-relaxation-times-drt_electrochemistry-an60.pdf`.

[86] Michael A. Danzer. Generalized distribution of relaxation times analysis for the characterization of impedance spectra. *Batteries*, 5:53, 2019.

[87] Jan Philipp Schmidt, Thorsten Chrobak, Moses Ender, Jörg Illig, Dino Klotz, and Ellen Ivers-Tiffée. Studies on lifepo4 as cathode material using impedance spectroscopy. *Journal of Power Sources*, 196:5342–5348, 2011.

[88] Mark E. Orazem, Pavan Shukla, and Michael A. Membrino. Extension of the measurement model approach for deconvolution of underlying distributions for impedance measurements. *Electrochimica Acta*, 47:2027–2034, 2002.

[89] Matthew Ginder-Vogel and Donald L. Sparks. *The Impact of X-Ray Absorption Spectroscopy on Understanding Soil Process and Reaction Mechanisms*. 2010. URL `https://www.sciencedirect.com/science/article/pii/S0166248110340013`.

[90] N. Fleck, H. Amli, V. Dhanak, and Waqar Ahmed. Emerging nanotechnologies for renewable energy. 2021. URL `https://www.sciencedirect.com/book/9780128213469/emerging-nanotechnologies-for-renewable-energy`.

[91] Pandian Bothi Raja, Kabilashen Readdyi Munusamy, Veeradasan Perumal, and Mohamad Nasir Mohamad Ibrahim. *Nano-Bioremediation: Fundamentals and Applications*. 2022. URL `https://www.sciencedirect.com/science/article/abs/pii/B9780128239629000374`.

[92] Mario El Kazzi. Li-ion solvation in tfsi and fsi -based ionic liquid electrolytes probed by x-ray photoelectron spectroscopy. *EPJ Web of Conferences*, 273:01001, 2022.

[93] Matthew Lacey, Anurag Yalamanchili, Julia Maibach, and Carl Tengstedt. The li-s battery: An investigation of redox shuttle and self-discharge behaviour with lino3-containing electrolytes. *RCS Advances*, 6:5, 2015.

[94] Shuo Wang, Mingxue Tang, Qinghua Zhang, Baohua Li, Saneyuki Ohno, Felix Walther, Ruijun Pan, Xiaofu Xu, Chengzhou Xin, Wenbo Zhang, Liangliang Li, Yang Shen, Felix H. Richter, Jürgen Janek, and Ce-Wen Nan. Lithium argyrodite as solid electrolyte and cathode precursor for solid-state batteries with long cycle life. *Advanced Energy Materials*, 11:2101370, 2021.

[95] Kerstin Wissela, Luise M. Rieggerb, Christian Schneiderd, Aamir I. Waidhaa, Theodosios Famprikise, Yuji Ikedaf, Blazej Grabowskif, Robert E. Dinnebierd, Bettina V. Lotsch, Jürgen Janek, Wolfgang Ensingera, and Oliver Clemensh. Dissolution and recrystallization behavior of li3ps4 in different organic solvents. *ResearchGate*, 2022.

[96] Yusuke Morino, Hikaru Sano, Koji Kawamoto, Ken ichi Fukui, Masato Takeuchi, Atsushi Sakuda, and Akitoshi Hayashi. Degradation of an argyrodite-type sulfide solid electrolyte by a trace of water: A spectroscopic analysis. *Solid State Ionics*, 392:116162, 2023.

[97] M Descostes, F Mercier, N Thromat, C Beaucaire, and M Gautier-Soyer. Use of xps in the determination of chemical environment and oxidation state of iron and sulfur samples: constitution of a data basis in binding energies for fe and s reference compounds and applications to the evidence of surface species of an oxidized pyrite in a carbonate medium. *Applied Surface Science*, 165:288–302, 2000.

[98] M. Tułodziecki, J.-M. Tarascon, P.-L. Taberna, and C. Guéry. Catalytic reduction of tfsi-containing ionic liquid in the presence of lithium cations. *Electrochemistry Communications*, 77:128–132, 2017.

[99] Hyeseung Chung, Yixuan Li, Minghao Zhang, Antonin Grenier, Carlos Mejia, Diyi Cheng, Baharak Sayahpour, Chengyu Song, Meghan Hannah Shen, Ricky Huang, Erik A. Wu, Karena W. Chapman, Suk Jun Kim, and Y. Shirley Meng. Mitigating anisotropic changes in classical layered oxide materials by controlled twin boundary defects for long cycle life li-ion batteries. *Chemistery of Materials*, 34:7302–7312, 2022.

[100] Yong-Ning Zhou, Jun Ma, Enyuan Hu, Xiqian Yu, Lin Gu, Kyung-Wan Nam, Liquan Chen, Zhaoxiang Wang, and Xiao-Qing Yang. Tuning charge–discharge induced unit cell breathing in layer-structured cathode materials for lithium-ion batteries. *Nature Communications*, 5:5381, 2014.

[101] Jingyi Wu, Zhixiang Rao, Xueting Liu, Yue Shen, Chun Fang, Lixia Yuan, Zhen Li, Wuxing Zhang, Xiaolin Xie, and Yunhui Huang. Polycationic polymer layer for air-stable and dendrite-free li metal anodes in carbonate electrolytes. *Advanced Materials*, 33:2007428, 2021.

[102] Isabella Weber, Dr. Jihyun Kim, Dr. Florian Buchner, Dr. Johannes Schnaidt, and Prof. Dr. R. Jürgen Behm. Surface science and electrochemical model studies on the interaction of graphite and li-containing ionic liquids. *ChemSusChem*, 13:2589–2601, 2020.

[103] Matteo Leoni, Rosa Di Maggio, Stefano Polizzi, and Paolo Scardi. X-ray diffraction methodology for the microstructural analysis of nanocrystalline powders: Application to cerium oxide. *Journal of the American Ceramic Society*, 10:1111, 2008.

[104] Xianyang Wu, Bohang Song, Po-Hsiu Chien, S. Michelle Everett, Kejie Zhao, Jue Liu, and Zhijia Du. Structural evolution and transition dynamics in lithium ion battery under fast charging: An operando neutron diffraction investigation. *Advanced Science*, 2:2102318, 2021.

[105] Ming Liu, Chao Wang, Chenglong Zhao, Eveline van der Maas, Kui Lin, Violetta A. Arszelewska, Baohua Li, Swapna Ganapathy, and Marnix Wagemaker. Quantification of the li-ion diffusion over an interface coating in all-solid-state batteries via nmr measurements. *Nature Communications*, 12:5943, 2021.

Appendices

A

Appendix A

A.1. Specification Sheet LPSCl, Lithium Phosphorus Sulfur Chloride

A.1.1. Product Identifiers:

Product Name / Ddescription	Lithium Phosphorus Sulfur Chloride (LPSCl) powder
CAS Number:	The CAS number is unknown or ahs not been assigned to this material

A.1.2. Relevant Identified Uses of the Substance or Mixture and USes Advised Against:

Identified Uses:	Solid electrolyte material; laboratory chemicals; synthesis of substances

A.1.3. Composition / Information of Ingredients

Component:	Lithium Phosphorus Sulfur Chloride
Formula:	Li_6PS_5Cl
Synonyms:	LPSCl, Argyrodite
CAS#	n/a
Concentration:	≥ 100%
Average Particle Size (D_{50}):	5 μm
Hazard Classification:	Flammable solid (Cat. 1, H228); In contact with water releases flammable gasses (Cat. 2, H261); Toxic is swallowed (Cat. 3, H301); Causes severe skin burns and eye damage (Cat. 1B, H314); Harmful if inhaled (Cat. 4, H332); Very toxic to aquatic life (Cat. 1, H400)
Physical State:	Solid (powder)
Color:	Light brown, beige
Odor:	Rotten eggs (sulfur) smell, stench
Water Solubility:	Insoluble

Specification sheet is publicly available at: https://www.neicorporation.com/products/batteries/solid-state-electrolyte/

A.2. Specification Sheet NANOMYTE®BE-56E (NMC811)

A.2.1. Active Material Characteristics

Product Description:	Lithium Nickel Manganese Cobalt Oxide (NMC811) electrode sheets
Formula:	$LiNi_{0.8}Mn_{0.1}Co_{0.1}O_2$
Average Particle Size (D_{50}):	10 - 13 μm
Specific Surface Area:	0.2 - 0.5 m^2/g

A.2.2. Electrical Characteristics

Nominal voltage vs. Li/Li^+:	3.75V
Minimum capacity:	190mAh/g
Experimental capacity:	≥ 200mAh/g (3 - 4.3V @ 0.1C)

A.2.3. Recommended Operating Conditions

Maximum Charge Voltage:	4.5V vs. Li/Li^+
Maximum Charge Current:	1C
Cutoff Voltage for Discharge:	2.7V vs. Li/Li^+
Maximum Discharge Current:	5C

A.2.4. Available Quantities

NEI's standard electrode sheets are available in packages of 2, 5, & 10 sheets. Bulk quantities are also available.

A.2.5. Precaution for Safe Storage & Handling

Personal protective equipment should be used at all times. Avoid contact with eyes and skin. Ensure adequate ventilation and avoid inhalation of dusts. Wash hands thoroughly after handling. Store in a dry and sealed pouch or under inert atmosphere, away from heat. Avoid moisture.

Specification sheet is publicly available at: https://www.neicorporation.com/products/batteries/cathode-anode-tapes/

A.3. Specification sheet MSE PRO Single Crystal High Nickel NMC Ni82

A.3.1. Properties

Appearance	Grey Black Powder
D10 (μm)	≥ 1.0
D50 (μm)	3.0 - 5.0
D90 (μm)	≤ 10.0
Dmax (μm)	≤ 25.0
H_2O (ppm)	≤ 600
pH	≤ 11.9
BET Specific Surface Area (m^2/g)	0.30 - 0.9
Tap Density (g/cm^3	≥ 0.8

A.3.2. Chemial Properties

Ni+Co+Mn (wt%)	58.5 - 60.5
Li (wt%)	7.0 - 7.6
Ni (mol%)	83.0
Co (mol%)	11.0
Mn (mol%)	6.0
Ca (mol%)	≤ 0.0100
Cu (mol%)	≤ 0.0020
Fe (mol%)	≤ 0.0050
Na (mol%)	≤ 0.0300

A.3.3. Half Coin cell performance

0.1C (mAh/g)	≥ 200
0.5C (mAh/g)	≥ 190
1C (mAh/g)	≥ 185
First cycle efficiency (%)	88.68

Specification sheet is publicly available at: https://www.sigmaaldrich.com/NL/en/product/aldrich/719781

A.4. Specification sheet Carbon Nanofibers

A.4.1. Properties

Quality Level	200
Form	powder
D x L	100 cm x 20-200μm
Impurities	iron-free, <100 ppm Iron content
Average diamter	130 nm
Pore size	0.075 cm^3/g average pore volume, 124Åaverage pore diameter
Surface area	average specific surface area 24 m^3/g
mp	3652-3697°C
density	1.9g/mL at 25°C

A.4.2. Product Specification

Product name	Carbon nanofibers - graphitized (iron-free), composed of conical platelets, D x L 100 nm x 20-200 μm
Product number	719781
Formula:	C
Formula Weight:	12.01 g/mol
Appearance (Color)	Black
Appearance (Form)	Powder
X-Ray diffraction	Conforms to structure
Iron (Fe)	100 ppm

Specification sheet is publicly available at: https://www.sigmaaldrich.com/NL/en/product/aldrich/719781

B

Appendix B

B.1. Cycling Performance of Polycrystalline NMC811 with a Spray-Dried Polymeric Coating

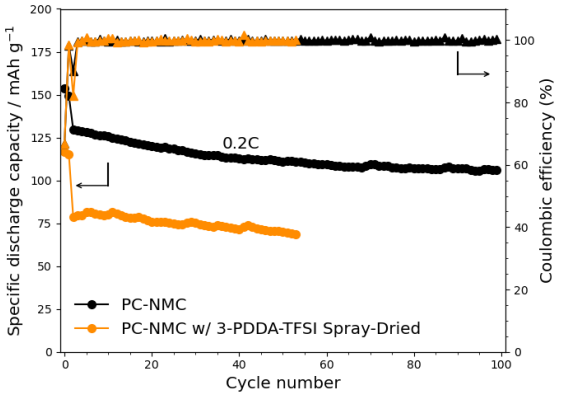

Figure B.1: Long-term cycling discharge capacity of lithium-indium alloy anode, LPSCl, and Pristine polycrystalline NMC811, and NMC811 with a 3wt% PDDA-TFSI spray dried protective coating, at 0.05C for the first two cycles and 0.2C for following cycles. NMC active materials = 10 mg cm^{-1}.

B.2. XPS - S2p Spectra of Spray-Dried Polymeric Coating

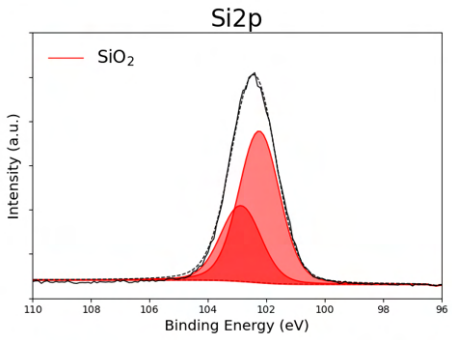

Figure B.2: Si2p spectra of XPS measurements of polycrystalline NMC with spray-dried PDDA-TFSI. Indication of Silicon contamination during polymeric coating application process.

B.3. DRT analysis of Polycrystalline NMC

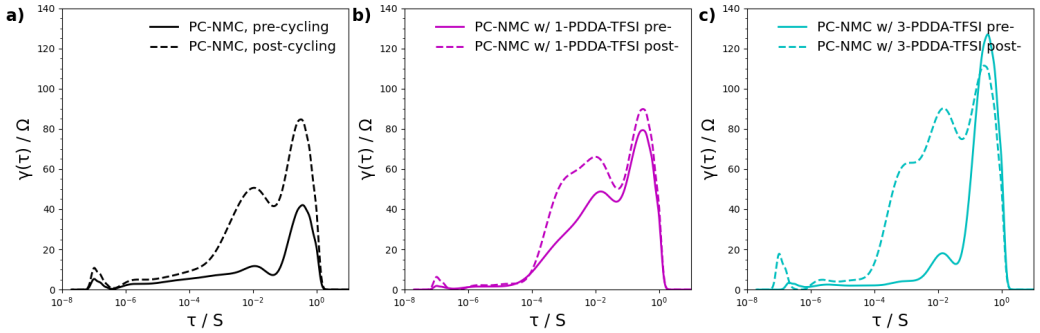

Figure B.3: DRT plots of pre-, and post-cycling for a) PC-NMC, b) PC-NMC with a 1wt%, and c) 3wt% PDDA-TFSI polymeric protective coating.

B.4. Pawley Refinement of XRD Patterns of Polycrystalline NMC

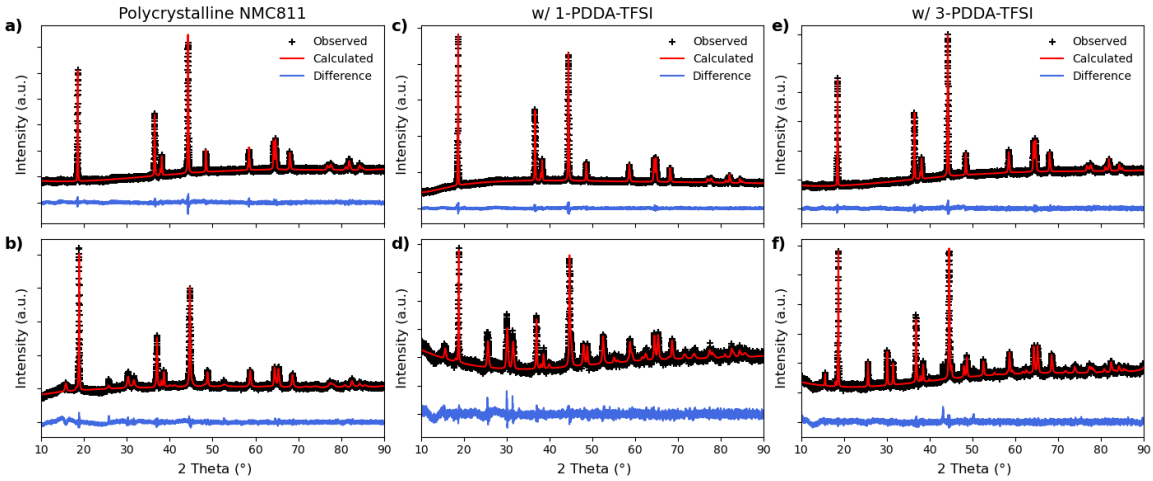

Figure B.4: Pawley refinement fits of XRD patterns of a) PC-NMC powder, b) post-cycling PC-NMC, c) PC-NMC with 1wt% PDDA-TFSI powder, d) PC-NMC with 1wt% PDDA-TFSI post-cycling, e) PC-NMC with 3wt% PDDA-TFSI powder, and f) PC-NMC3 with wt% PDDA-TFSI post-cycling.

C

Appendix C

C.1. Cycling performance including capacity retention at 0.05C

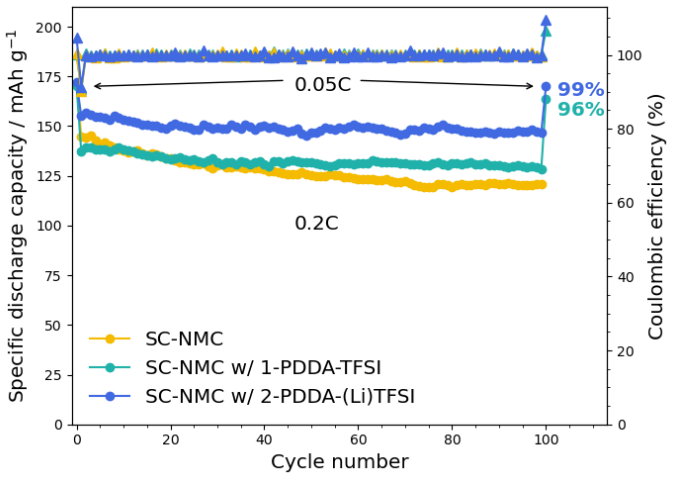

Figure C.1: Long-term cycling discharge capacity of lithium-indium alloy anode, LPSCl, and single-crystal NMC (Ni82), NMC with a 1wt% PDDA-TFSI, and NMC with 2wt% PDDA-(Li)TFSI, at 0.05C for the first cycle and 0.2C for following cycles, and 0.05C for cycle 101. Capacity retention at a rate of 0.05C is specified for the coated samples. NMC active materials = 10 mg cm^{-2}.

C.2. EIS Measurement Voltages

Table C.1: Cell Voltages during EIS measurements, pre- and post-cycling, of SC-NMC, SC-NMC with 1-PDDA-TFSI, and SC-NMC with 2-PDDA-(Li)TFSI.

Sample	Pre-cycling	Post-cycling
SC-NMC	2.987V	3.01V
SC-NMC w/ 1-PDDA-TFSI	3.005V	2.994V
SC-NMC w/ 2-PDDA-(Li)TFSI	2.995V	2.999V

C.3. DRT Analysis of Single-crystal NMC

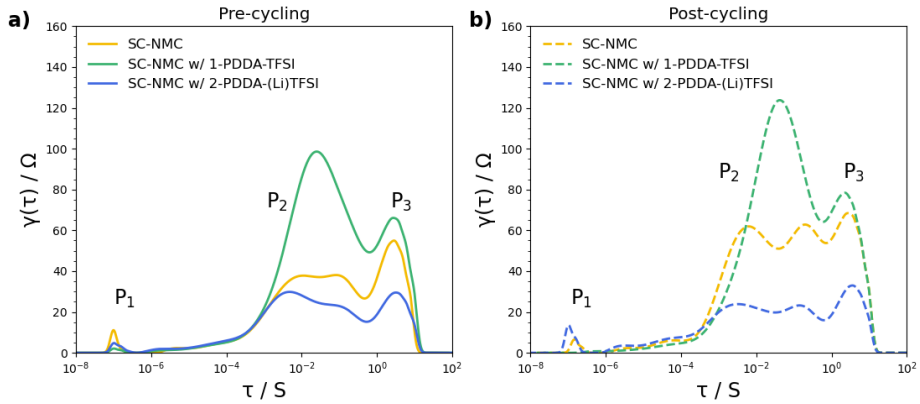

Figure C.2: DRT plots of PC-NMC, PC-NMC with a 1wt%, and 3wt% PDDA-TFSI polymeric protective coating, a) pre-cycling, and b) post-cycling.

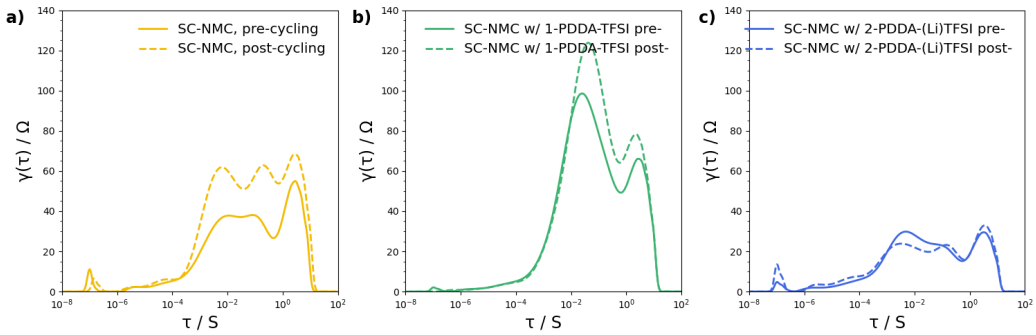

Figure C.3: DRT plots of pre-, and post-cycling for a) SC-NMC, b) SC-NMC with a 1wt%, and c) 2wt% PDDA-(Li)TFSI polymeric protective coating.

C.4. Pawley Refinement of XRD Patterns of Single-Crystal NMC

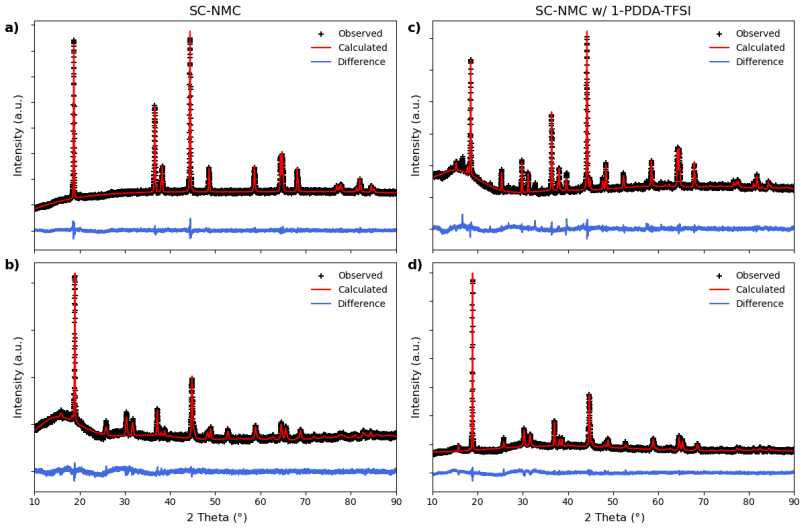

Figure C.4: Pawley refinement fits of XRD patterns of a) SC-NMC powder, b) post-cycling SC-NMC, c) SC-NMC with 1wt% PDDA-TFSI powder, d) SC-NMC with 1wt% PDDA-TFSI post-cycling.

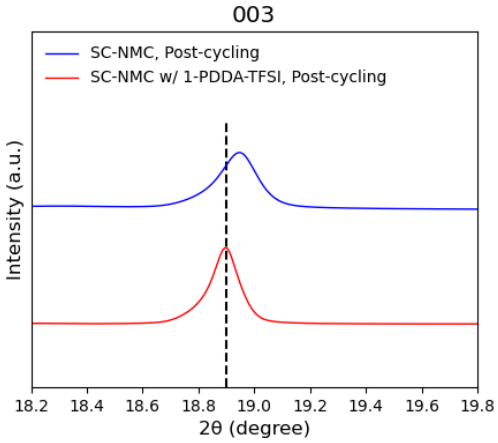

Figure C.5: Pawley refinement fit of 003 peaks in the XRD pattern after cycling a) uncoated SC-NMC, and b) SC-NMC with 1wt% PDDA-TFSI.